Optical Fiber Coupled Low Power Micro-PIV Measurement of Flow in Microchambers: Modeling, Fabrication, Testing and Validation

Qing Fang

A Thesis

in

The Department

of

Mechanical and Industrial Engineering

Presented in partial fulfillment of requirements for the

Degree of Master of Applied Science (Mechanical Engineering) at

Concordia University

Montreal, Quebec, Canada

November, 2009

Your file Votre référence
ISBN: 978-0-494-67297-6
Our file Notre référence
ISBN: 978-0-494-67297-6

ABSTRACT

Microfluidic chip is one of the important tools for modern analytical sciences. It is an important and fast developing component for applications in life science, environment science, medicine and chemistry.

While its development is spread over tens of years, the basic research on flow mechanism in microfluidics is far behind its application research. This study applies flow visualization techniques to measure the parameters of flow in microchambers for comparing their performance. Geometrical influence of microchambers on flow behavior is found through experimental and theoretical investigations. In order to quantify the effect of geometry, many microfluidic chips were designed with microchambers of different shapes and experimentally tested for various flow rates. As a result, it was identified that symmetrical and asymmetrical shapes have varying effects on the performance of microfluidic chips.

In the experiment, the microfluidic chips based on glass platform were fabricated by CMC. This study discusses the main differences and other key factors among many visual observation techniques. This thesis applies micro-particle image velocimetry (μPIV) technique to measure the flow fields in microchambers using de-ionized water. Low power and optical fiber coupled micro PIV experimental system was developed and implemented in-house. This system utilizes an epi-fluorescent microscope, seed particles, high speed CCD camera, green pulsed laser and optical fiber components to record the particle-image fields. The implemented platform is able to capture the fluid behavior in microchambers.

Oblique illumination method was developed for illuminating the flow in microchambers. The oblique illumination method provides a low-cost platform enabling low power studies. Different packaging and interconnection techniques were developed for leak proof sealing of microfluidic ports. Both numerical and experimental investigations have been carried out for different geometries of microchambers under varying Reynolds numbers. Commercial Finite Element Analysis software COMSOL was used to solve the required differential equations. The comparison of simulation results shows a close agreement with experimental results.

Acknowledgment

First of all, I would like to thank Dr. Muthukumaran Packirisamy, my advisor, for his wisdom, patience and knowledge. His timely feedback and ideas injected in the development of this study.

I would like to express my sincere gratitude to my advisor, Dr. Kamran Siddiqui, for his support guidance and contributions in all aspects of the research and for encouragement me to keep engineering mind. I'll always keep that in my mind on my future career.

Appreciation goes to all the colleagues in Dr. Packirisamy's Laboratory and Dr. Siddiqui's laboratory for their friendship and assistance during the past years of my graduate education.

Most of all, the deepest appreciation goes to my family, especially for parents, for their encouragement and support throughout my life. This work would not have been completed without their deepest care and love.

Table of Contents

LIST OF TABLES

LIST OF FIGURES

NOMENCLATURE

c	concentration of fluorescence matter
D	Brownian motion diffusion coefficient (m^2/s)
D_B	Beam diameter
de	effective image diameter for particles with finite size
d_I	diameter of particles' image
d_P	diameter of the seeding particles
D_p	density of the power
d_s	diameter of the diffraction ring
E	energy per each pulse (Joule)
f	Focal length
FN	number of field of view
FOV	field of view
I_o	light source optical power (Watts/ cm2)
K	Flow coefficient
Kn	Knudsen Number

L	characteristic length of the channel
M	magnification
n	density of the particles
NA	numerical aperture
P	pressure
Q	flow rate
Re	Reynolds number
RPM	Revolutions per minute
S	distance of diffusion
S_m	size of the image
u_i	Instantaneous velocity
Var	Variance
Vx	Absolute velocity in the x-direction
Vy	Absolute velocity in the y-direction
w	average velocity
λ	wave length (nm)
μ	dynamic viscosity (kg/m-s)
μPIV	Micro Particle Image Velocimetry

ρ	density (kg/m3)
v	kinematic viscosity
λ	mean free path
ε	molar absorption coefficient
Δp	Pressure drop
Δt	time interval between two frames of images

Chapter 1

Introduction to microfluidics system and applications

1.1 Introduction to microfluidics System

Microfluidics is a new field that allows the development of systems to synthesize and purify chemicals, biological products, and materials with the usage of integrated and miniaturized platforms. Compared to macro fluidic systems, microfluidic systems have low fabrication cost, enhanced analytical performance and minimal consumption of chemicals or bio-products. The main advantage of microfluidics is that it gives better control of processes. This is because the micro flow has high surface to volume ratio and therefore the responses to control actions are better. It also gives better selectivity and induce higher yield. In addition, microfluidic systems require low energy cost, and give very rapid reaction speed, with minimal cost of reagents, which could be used for dangerous substances with safe handling, and allow various flow analyses simultaneously. Furthermore, since the size of the entire system is small, it is much easier for transport comparing to conventional fluidic systems. In biomedical applications, since the microfluidic devices approach cellular size, it can be used for the analysis and characterization of individual cells.

The first application of microfluidic system was the low-cost disposable inkjet print head developed in mid-1980's [1]. Lately, people discovered that microfluidics could be used in biomedical and health care systems as it allows using biological samples within the micro volumetric scale. Most recently, the majority of work on microfluidic devices is conducted in the fields of biomedical, diagnostics, pharmaceuticals, aerospace, fuel cell and cooling of electronic devices. The miniaturized "micro total analysis system" (μTAS), which was first introduced in 1990's by Manz et al. [2], has been developed for the drug delivery, DNA analysis and sequencing, and biological/chemical-agent detection.

1.1.1 Definitions in microfluidics

Microfluidic system is geometrically constrained to a sub-millimeter (1micron to 1mm) scale, which can be used for manipulating fluids inside chips that were manufactured by silicon, glass, or polymer, etc. These chips may contain micro pumps, mixers, micro chambers, micro channels, reservoirs and some connecting ports. In order to study microfluidics, certain peripheral apparatus including measurement system, driving system, and tubing system have to be used. In the study of microfluidic system, several important parameters determine the characteristics of flow within the system.

The key factor of the microfluidics experimental platform is the design of the microcircuits. The characteristics that influences the behavior of the flow inside a microfluidic device includes hydrophilicity and hydrophobicity of the channel wall, the geometric shape and dimensions of the chamber, fabrication technology and working fluid pressure, and temperature. The design of the experimental platform also has to associate with the requirement of the optical equipments in order to provide better measurement results.

Reynolds Number represents the ratio between the inertia and viscous forces in the flow. The equation for the calculation of Reynolds number is:

$$\mathrm{Re} = \mathrm{wb}/\nu \tag{1.1}$$

Where, w represents the average velocity of the flow; b is the characteristic length of the channel (typically the channel width) and ν is the kinematic viscosity of the fluid. In microfluidic systems, the Reynolds number is typically in the range 0.1 to 5.

The Knudsen Number (Kn) is another very important parameter for the evaluation of the suitability of the flow. The Kn can be calculated as:

$$Kn = \frac{\lambda}{L} \tag{1.2}$$

Where, λ is the mean free path of the particles (molecules). L is the characteristic length of the microchamber or microchannel. Under equilibrium condition, due to the randomness of the particle collision, the distance between two collisions of the same particle is never the same. By taking the average distance between every two collisions, the mean free path can be calculated as:

$$\lambda = \frac{1}{\sqrt{2}\pi d^2 n} \tag{1.3}$$

Where, n is the density of the particles and d is the diameter of the particles. λ is inversely related to density and particle diameter, but insensitive to thermal movement of the molecules. In the present study, the working fluid is deionized water. The average diameter of the water molecule is 3.7Å. The density of water is 1000 kg/m^3, and the characteristic length of the microfluidic channel is 75μm. Thus, in the present study, λ is equal to 3.1nm, and Kn is equal to 4.13×10^{-5}. Therefore, the calculated Kn number falls

within the range, that Kn < 0.003 the continuum assumption holds with no slip at the solid surface and thus, the Navier-Stokes equation is valid [3].

1.1.2 Factors influencing flow velocity distribution

The flow velocity distribution within certain flow field is highly dependent on the characteristic of the fluid, and the surrounding environment. There are two commonly used methods for driving flow through microchannels: pressure driven flow and electrokinetic driven flow. In pressure driven flow, fluid is pumped through microchannels by pumps. This produces a parabolic velocity profile within the channel. Once the fluid enters the chamber from the channel, it undergoes the developing phase, and the velocity profile is no longer constant and changes with the distance.

The electrokinetic driven flow refers to the combination of electro-osmosis and electrophoresis. Electro-osmosis utilizes charged double-layer at the solid-liquid interface that move the fluid in bulk within the channel under electrical field applied to either side of the channel. This method involves charging of layer near wall and pulling the fluid to move. Depending on the orientation of the electrical field, the flow may move in different directions [4]. Electrophoresis causes charging of a surface submerged within the fluid to move towards the electrode. Fundamentally, electro-osmosis and electrophoresis are different. Electro-osmosis causes the net mass of the fluid to transfer whereas, electrophoresis causes movement of charged particles or molecules.

1.1.3 Features of microfluidics system

A microfluidic system includes micro-flow delivery, mixing and measurement apparatus. In microfluidic systems, the surface tension of the flow which could be significant is quite different due to surface effects. Because of the smaller dimensions of the system, the techniques used in classical flows cannot be applied to microfluidic

systems. The measurement, analysis and research methods for microfluidic systems are different from that of the conventional macro-scale fluidic systems.

For instance, the electrokinetic driver is the most commonly used driving system in miniaturization system research, whereas pump is the driving system in conventional fluidic studies.

1.2 Fabrication of microfluidic elements

Although there are many commercial technologies for fabricating silicon-based devices, silica or glass are superior for their optical transparency, low electrical conductance and biocompatibility. Even though some other active researches have chosen polymers as the material for microfluidics chips, silica or glass are still the most common choice due to their low auto-fluorescence, mechanical durability, reusability and smooth surfaces. Therefore, the glass-based chip had been chosen for this research.

Microfluidic structures are usually fabricated with chemigraphy. The basic structures to be fabricated are channels and chambers, which together form the mixer, pump, reservoirs, etc. The choice between the fabrication methods depend on the number and shape of the required features which are based on the functionality of the microfluidic device. Chemical etching processes are normally used for glass [5] whereas silica requires hydrofluoric acid vapor [6] and xenon difluoride for silicon [7] whenever isotropic etch characteristics are allowed. Certain chemicals chosen for etching may have very high selectivity between masking materials and fabricating material with different etch rates, so that the mask will not be consumed at all. The disadvantages of the chemical etching for glass include the isotropic etch behavior (i.e. the etch rate is the

same in every direction within the material to be etched), and its high requirement on the integrity and the precision of the etching mask.

Ion beam etching, also known as ion milling, utilizes noble gas ions [8]. This process is a pure physical sputtering without chemical reactions. It can be used for etching materials that normally cannot be chemically etched easily. Compared to chemical etching, this method has a low etch rate and low etching selectivity towards any masking material.

Plasma jet etching is a widely used commercialized technique for shaping high aspect ratio structures in silicon and glass [9]. It allows exploitation of both chemical and physical processes in order to remove solid material locally. This method requires several gas precursors and the chambers have been designed for versatile etching. By using a suitable mask, the plasma jet can be defocused to etch a larger area and to yield higher aspect ratio.

In powder blasting, which is also known as abrasive jet machining [10; 11], hard particles are blown to the surface with high velocity, causing erosion. Using elastic mask, which is not eroded by the silicon carbide or sapphire particles, moderate aspect ratios in glass and other materials, can be achieved. Other methods used for fabrication of the glass based microchips include drilling and laser ablation [12].

1.2.1 Components

In older microfluidic systems, several components were externally connected to a given microfluidic system. However, in newly designed microfluidic system, these components are integrated within a given microfluidic system.

1.2.1.1 Driving system: In the old microfluidic system, external pumps such as centrifugal pumps were used. In order to precisely provide amount of micro volume, peristaltic pumps are used in this research as the driving system. However, peristaltic pump is also an external pump. In order to integrate the driving system entirely into the microfluidic chip, electrokinetic pump has been developed for such a purpose. The currently used electrokinetic pumps, which was first reported by Bart et al [13], use electroosmosis, electrophoresis, or de-electrophoresis electrokinetic phenomena as the fundamental driving force.

1.2.1.2 Mixer: Since the flow in microfluidic systems is typically laminar, the mixers of the microfluidic system are much more complicated than conventional fluidic system. The diffusion time is proportional to the square of the mixing path and therefore faster mixing is a major goal that needs to be achieved. The mixers are classified into two groups, the passive mixers and active mixers. The passive mixer utilizes the shape of the channels which allow multiple bypasses of two flows, whereas the active mixer uses electric force or magnetic force causing the oscillation of the flow within certain region of the channel.

1.2.1.3 Integrated sensory system: Variety of sensors can be integrated into the chips [14]. For instance, electrical sensors, chemical sensors, thermal sensors [15], and light source or waveguides [16] have been integrated into the chips for different applications. As the fabrication technology improved, more and more components can be integrated into the chip. Integration of apparatus such as camera and battery of micro lens are active research areas in microfluidics.

1.3 Measurement technologies for microfluidic systems

Different measurement technologies are used in the microfluidics systems. Flow field is the fundamental parameter to be measured in microfluidic research. Microscale Particle Image Velocimetry (μPIV) is the most common flow field measuring method. There are several branching methods from PIV, such as infrared micro-PIV, micro particle image thermometry, particle tracking velocimetry and stereoscopic micro particle image velocimetry [17]. Nowadays, the improvement of measurement methods are focused on increasing the sensitivity under high flow velocities, increasing detection limits towards smaller scaled apparatus [18], increasing the precision of the timing and decreasing the size of the particle. Other typical parameters measured in microfluidic systems such as electrical pulse, resistance, electrochemical reactions, or variety of photo spectrum, have also been improved in terms of precision and diversity of specimens [19].

1.3.1 The μPIV Measurements

In recent years, the rapid development of laser technology has led to the improvement of micro particle image velocimetry (μPIV), which works with double-pulsed laser as a light source. The process of PIV measurement is described below:

(1) The tracer particles are mixed into the flow field.

(2) A laser pulse illuminates the measurement plane at a time instant t and the camera captures the images of the tracer particles in the measurement plane. A short time later ($t + \Delta t$), the second laser pulse illuminates the same measurement plane and the camera captures the second image of the tracer particles. This way a sequence of image pairs are obtained.

(3). These images are divided into numbers of interrogation regions, so that the average displacement of particles within each region can be estimated through cross-correlation between the interrogation region in the first image and the corresponding search region in the second image of the image pair.

(4). By dividing the average particle displacement by the time difference between the two image of the image pair (i.e. Δt), the average velocity in each interrogation region can be obtained and thus, the velocity field of the entire measurement plane.

In 1996 Brody et al. [20] published a paper about a μPIV applied with an 11x72 μm cross section of silicon channel. Meinhart et al. [21] used polystyrene-particles coated with fluorescent material, instead of non-coated particles in the Nd: YAG laser pulse excitation. In 2003, Devasenathipathy et al. [22] performed detailed flow investigation of a cross-point in cross channels. The primary interest was to develop and compare the micro particle image velocimetry (μPIV) and particle tracking velocimetry (PTV), which are the new generation of velocimetry measurement techniques.

1.4 Applications of microfluidic system

Recently, the application of microfluidics has been derived into several different fields, including biological, pharmaceutical, medical diagnostics, food inspection, environmental analysis, pollution control, and electric appliances.

In modern biological researches, especially in molecular biology, the microfluidic system has been widely used in the case of cytometry [23], cellular component analysis, and protein and DNA analysis [24]. In cytometry, microfluidic system has been used for cell counting and cell sorting. The cell counting system uses either fluorescent signal or

non-fluorescent diffractions to obtain different information of cells. Depending upon the amount of light transfer though each cell, the cell transparency can be determined and the subcellular component of the cell can be briefly examined. Another detector, which obtains the information on reflected light by the cell, gives information on the cell surface property. Together with both transparent light and reflected light, the number and size of the cells within the solution and the characteristics of the cells can be determined. Compared to the original cell counter which is based on Coulter principle under ordinary fluidic system, the flow cytometry obtains much detailed information on the examined cells. In order to minimize the amount of proteins and DNA samples used in the analyses such as concentration determination, electrophoresis separation, and luminance reaction, several research groups have been working on integrated microfluidics to achieve lab-on-chip capability for DNA analysis [25; 26].

In pharmaceutical applications, microfluidic system can be used in chemical reaction, drug delivery, and packaging of liquid drugs [27; 28]. Microfluidic system with different reaction chambers could be used to control the reaction speed in pharmaceutical drug production and research. Furthermore, the microfluidic system takes the advantage of minimal reagent consumption and accelerated reaction speed, which makes it suitable for drugs scanning. In terms of drug delivery, micro-pumps are used in the slow release of drugs for diabetics or heart diseases [29]. The microfluidic system has been put under discussion for its application in point of care (POC) testing system [30; 31]. POC testing is a diagnostic process near or at the site of the patient, which utilizes transportable, portable, and handheld instruments and testing kits. Currently POC instruments including blood-gas monitor, blood glucose monitor may use microfluidic system to increase the test efficiency and decrease the cost of the

instrument. Since these devices require accurate liquid sample uptake, microfluidic system can provide better sampling accuracy.

Moreover, microfluidic system has also been used in the food inspection. Certain wine and cheese industry uses microfluidic system for rapid quality control and the detection of formaldehyde level in food products [32]. This application, which detects trace of chemicals within certain samples, may also be applied in environmental studies and pollution control. The quality monitoring systems use immunosensors that contain a microfluidic chamber to detect the presence of potential harmful chemicals and bacteria [33]. These sensors use antibodies to bind the target contaminates and therefore change the optical properties of the examined fluid which then be detected by optic sensors. Another application of microfluidic system in food industry is the microfiltration techniques. Compared to traditionally thermal processing, the microfiltration techniques require low energy and avoid thermal damage of tastes and fragrances [34; 35].

The environmental monitoring is another application of microfluidic system [36; 37]. It has been used for the biological decompost of organic matter, nitrates, and phosphates in aerobic environment. Nowadays, the efficiency of biological decomposition is low due to the insufficient oxygen supply, which can be provided by continuous supply of air bubbles using aerators. Currently aerators use porous materials to create bubbles. By introducing the microfluidic system in aerators, smaller micro bubbles can be produced which provide larger surface area and increase the efficiency of oxidation process.

As energy storage demands increase with the next generation of portable electronic devices, current lithium ion battery technology is considered unlikely to keep

pace. Miniature fuel cell devices have recently attracted a great deal of attention as an improved power supply for portable electronics [38].

1.5 Objectives of the present study

The present research provides an investigation of the velocity field within different geometric components. The main objective is to obtain an in-depth knowledge of the complicated interaction between the fluid and the chamber, by investigation the flow field, which is measured using a Micro Particle Image Velocimetry (μPIV) System. The flow velocity distribution is an important parameter, which provides a useful reference to evaluate and design fluidic elements in various applications. We have subdivided our discussions into three primary sections: design and fabrication of microfluidic chips (Chapter 2), μPIV system observed experimental results (Chapter 3, 4), and comparison of the simulated flow distribution using FEM software (Chapter 5).

Chapter 2

Design and fabrication of microfluidics chip

2.1 Introduction

The fabrication of micro fluidic apparatus includes: design, layout, microfabracation, bonding and assembling. The fabrication materials include singlecrystal silicon, polysilicon, silica, glass, epoxy, polyurea, polyamide, polystyrene, polymethylmethacrylate and PDMS (Polydimethylsiloxane) and they are separated into two categories namely, elastic and rigid. Depending on the material, different fabrication methods can be applied. They are mainly separated into two classes, which are direct micromachining and replication. The direct micromaching uses micro stereo lithography, plasma etching, laser ablation, deep reaction ion etching, surface micromachining, etc. The replication methods use a pre-developed mold to make chips. Generally, the replication methods require less cost. The fabrication of microfluidics is an important factor that determines the development of systems.

2.2 Micromachining technique for silicon-based chips

2.2.1 Singlecrystal silicon wafer

Since singlecrystal silicon wafer is a crystallized compound, this means the structure of the crystal is oriented to certain direction and it causes the etching rate to be different in different directions. This phenomenon has been used for bulk etching and known as anisotropic etching. For processing of singlecrystal silicon wafer, either wet etching or dry etching can be used.

Wet etching uses liquid chemical solutions on patterned wafer to achieve shaping of certain structure. Commonly used etchants include Alkali hydroxide etchants, ammonium hydroxide etchants, Ethylenediamine pyrochatechol (EDP), and Other etchants.

Dry etching uses gases to achieve shaping of certain structure. Compared to wet etching, dry etching requires short period of processing time, and can be used to obtain high-aspect-ratio structures. However, dry etching is more difficult to control due to the unevenly distributed etchant gas within the etching room. Plasma etching is a kind of dry etching, which also uses chemical reaction. Many materials can be treated with this method, including glass and silica to construct micro electrophoresis quartz glass or chromatography chips, as examples [39].

2.2.2 Polysilicon

Different from singlecrystal silicon, polysilicon is more suitable for surface micromachining. Polysilicon can be deposited on to a surface of different materials and etched out. Etching polysilicon is isotropic as it gives same etching rate at any direction. The etchants used for polysilicon machining is the same as that of singlecrystal silicon.

2.3 Polymer-based chips

Silicon was the first material used in the microfluidic system. However, since silicon is not biocompatible, polymers are used in the microfluidic chips for biological applications due to its high biocompatibility and elasticity. The micromachining method for polymers includes lithography, surface micromachining and micromolding.

2.3.1 Soft lithography

Whitesides from Harvard university is the pioneer in the field of soft lithography which is a micromachining technique used for elastic materials [40]. His research included the self-assembled monolayers (SAMs), elastomeric stamp and high polymer cast molding. The core technique in this method is the use of elastomeric stamp to imprint the scheme from the stamp to the target surface with a high polymer ink.

2.3.2 Micromolding

In this method, the key condition is the accuracy of the mould and the selection of the high polymer ink. The ideal ink should have a low adhesion force so that it can be easily removed from the mould. The mould can be made by silicon, glass, SU-8 or PDMS. Although the cast molding method is limited to certain easily solidified polymers, it is one of the most easily and rapidly performed method that can produce chips without expensive equipments. Other methods including imprinting, laser ablation and LIGA etc. could also be used on elastic materials.

PDMS is one of the most commonly used elastic materials in microfluidics chip production. The advantage of using this material is that it can be repeatedly deformed. It can also allow light with wavelengths over 300nm to pass though. Moreover, this material has a good biocompatibility, low toxicity and low cost. The disadvantage of

PDMS is that it cannot stand high temperature, and it has a low coefficient of heat conductivity. In 1998, Duffy, D.C. et al. [41] demonstrated the design and production of microfluidics chip with PDMS within 24hours.

2.4 Silica and glass

Although there are a lot of fabrication methodologies for silicon based microchips, the characteristics of silica and glass including optical transparency, low electrical conductance and biocompatibility, make it more suitable for certain applications. Compared to polymers, silica and glass have a higher surface smoothness, mechanical durability, reusability and lower auto-fluorescence. Furthermore, glass has better thermal stability, which is less likely been rusted by fluid compared to polymer made chips. Since fluorescence particle and external detection device have been used in this study, glass has been chosen as the best material for the fabrication of the microchips.

In general, the glass made chips provide better characteristics when used in microfluidic system compared to ordinary fluidic system. Compared to macro scale glass compartments, glass micro chips are better in terms of tensile strength and elastic deformation index. For glass based microchips, the fabrication method depends on the requirement of number, shape and function of the microcircuits.

2.4.1 Fabrication techniques for silica and glass

Chemical etching methods uses HF vapor, in the case of isotropic etching on silica. Chemical etching normally requires lithography for masking. The lithography has been broadly used in the micro chip production, which utilizes photoresist, mask and ultraviolet light to perform the patterning. During the past decade, more researches have presented wet etching techniques [42], as they are suitable for silica-based chip, glass-

based chip, and quartz glass-based chips. However, chemical etching has its limitation. Since isotropic etching gives same etching rate on every direction, high aspect structure is hardly produced by this method. Berthold et al. have devised a two step glass etching process using a double layer mask consisting of 400 nm thick amorphous silicon and 500 nm thick PECVD silicon carbide [43].

Powder blasting method uses particles with high hardness, such as silicon carbide or sapphire particles, to erode the wafer under high velocity. On this method structures with vertical walls can be produced. Furthermore, non-vertical surface can be formed by adjusting the angle of attack. This characteristic is widely used in fabrication of vertical connection holes or reservoirs. In this experiment, the reservoirs of microfluidic chip were made with powder blasting.

Other ongoing developing methods are used less often. For example, laser ablation was presented in 2004 by Niino H. et al. [44]. This method produces a non-satisfactory surface finishing, and therefore, powder blasting and laser ablation are often used for hole making in the chip.

The etch rate of all the methods, including chemical etching, physical ion etching and plasma etching, fall in the range of 0.5 to 5 μm/min. However, the surface smoothness is different for them. Chemical etching methods gives good surface finish compared to all other methods.

Other materials used in fabrication of microchips include plastics. Plastics are produced in precision finishing by casting machine and therefore are low in cost and rapid for production. However, due to the decrease in size of the microfluidic components, the plastic material is no longer fulfilling the requirement of the design proposal. Nowadays, plastics are only used for instruction and connector purposes.

2.5 Bonding

Bonding is the process of integrating a variety of apparatus together in order to construct the entire system depending on the applications. The bonding methods include fusion bonding, anodic bonding, adhering bonding, and low temperature bonding.

Fusion bonding is suitable for connection of micro structure made of glass or quartz. The critical point is the clearance and the flatness of the surface. To prevent the melting and deformation of the micro channel, other researchers used anodic bonding method for the glass-to-glass bonding. In anodic bonding, a thin layer of polysilicon or chlorinated silicon was used as the mid-layer.

2.6 Fabrication of the chip used in this experiment

The chip produced in this experiment is designed for examining the flow field distribution by using μPIV in order to improve the efficiency of chambers. Due to the high expense and technological limitation, the μPIV system used in this experiment contains external light source and external camera rather than integrated ones. Therefore, high transparency of the chip is required for the observation of the flow field and glass has been chosen as the material for the chip. The fluorescent particles used in this experiment have a diameter of 20μm, and therefore the diameter of the channel is 200μm and the etching depth is also 20μm.

2.6.1 Chip design

To achieve the objectives, chambers with different shape has been designed to understand the effect of shapes on chamber efficiency. Due to the cost issue of the experiment, the predesigned chambers are first simulated with COMSOL software to obtain the preliminary data on flow field distribution. Figure 2.1 shows the layout of the

designed chip. The major factor considered during the design of the chamber is the residence time which determines the period of time between entrance and exit of flow though the chamber. As the structure of the chamber varies, certain part of chamber may contain dead zone, which means no or very little replacement of the fluid within the zone. The dead zone will influence the reaction efficiency or cause precipitation to block the chamber, and therefore have negative effect on efficiency of the chamber. Furthermore, due to some other factors such as the characteristic of the material that makes the wall, and the near-wall effect, the flow distribution close to the wall of the chamber becomes rather complicated and therefore increases the uncertainty of the flow. In our experiment, the functional zone of the chamber was defined as central region which has certain distance from the wall. The distance varies depends on the initial flow velocity, material of the chamber, and shape of the chamber.

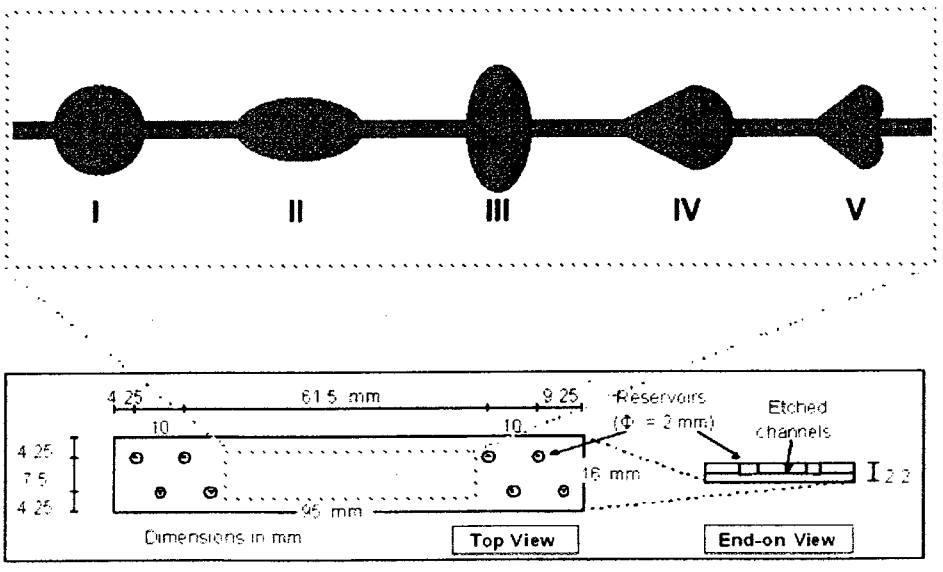

Figure 2. 1 Layout of the experimental chambers in Protolyne chip

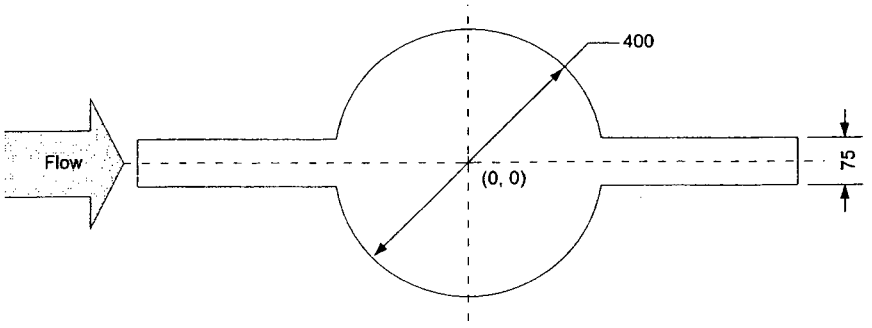

(I)

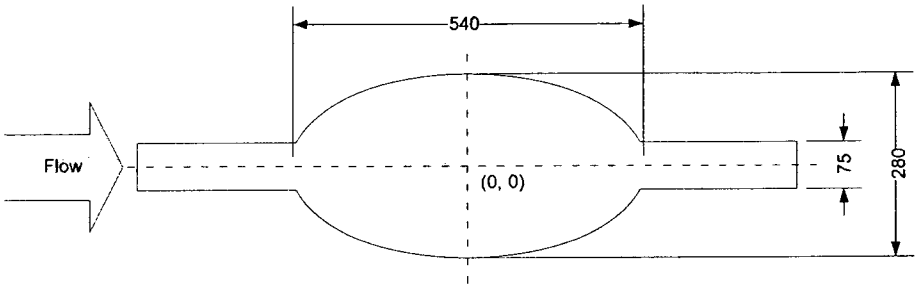

(II)

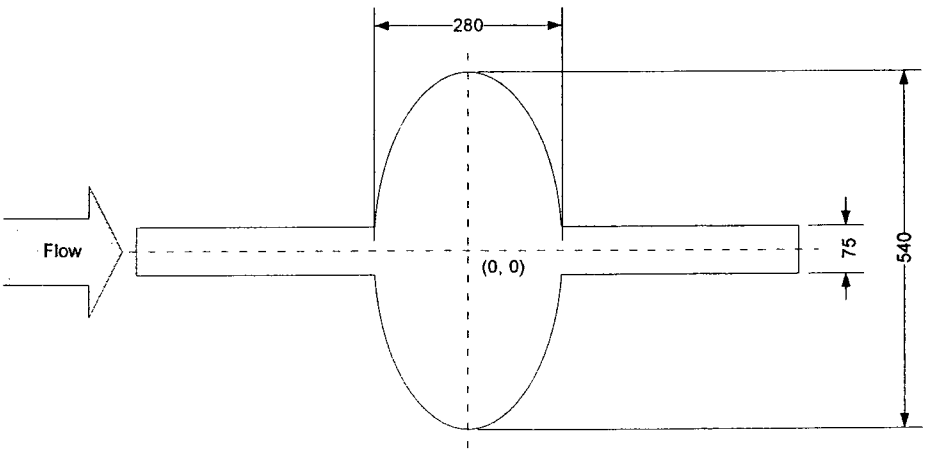

(III)

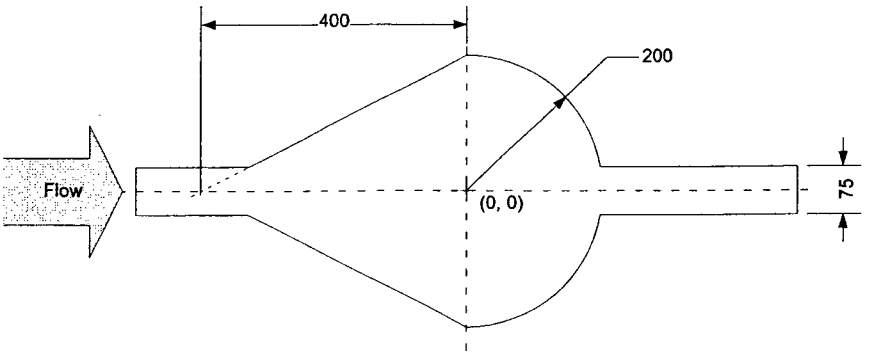

(IV)

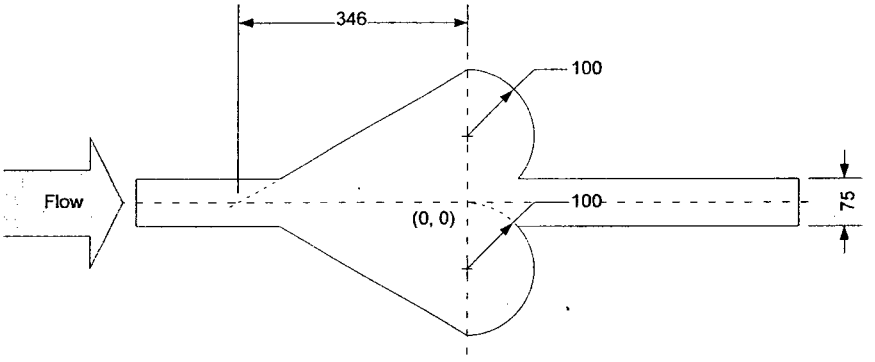

(V)

Figure 2. 2 Design of different microchambers showing geometrical dimensions (unit : micron)

The mask design requires the conjugation of fabrication technique and equipment capacity. For instance, the maximum resolution limited the precision of the acute angular structure within the micro fluidic channel, and different fabrication techniques also cause differences in the shape of the cross section.

In our experiment, mask design was conducted using L-edit program from Tanner Inc. This program was one of the programs recommended by CMC. The minimum width of the imprint line was first set at 0.1 micron; this was determined by the resolution of the fabrication. Then, the shape and location of the chambers are designed. Finally, these chambers are linked with channels. Depending on the fabrication method, the turning angle has to be considered. Since etching process can cause deformation of the structure, custom rules can be set in the software to examine the degree of angle between any crossing lines and minimum distance between two lines.

Other common designing software, such as AutoCAD, CATIA, ProE, etc. can also be used for making masking file. However, they are not specialized in designing for microsystems. L-edit v11.1 is focused on microsystem design. But the modern microsystem develops very fast and including more and more aspects in fields such as microfluidics, optics, micromechanism, and calorific, etc. These developments challenge the design softwares, even though they are updated frequently.

2.6.2 Chip manufacturing

In order to produce the designed chip, the layout has to be sent to Canadian Microsystems Corporation (CMC). CMC provides the tools, technologies and services for universities across Canada for research and development of microsystems. CMC provides services on design manufacture and testing of microsystems to faculty members and graduate students.

In industrialized chip production, the masking material includes chrome plated glass, or quartz glass. The CAD system is first used to generate the geometric drawing which is then transferred into data file. Using aligner, the drawing can be exposed onto the base plate which was coated with photoresistant material.

The manufacturing of glass based chip includes priming, coating of photoresist, soft bake, exposure, development, hard bake, etching, strip, positioning, and bonding. Since the adhesion force is low for the photoresistant material, it is easily peeled off during the development process. Therefore, a layer of photoresist material must be used to coat the surface of the substrate. After the layer is applied, the substrate will be put in the spin coater so that the photoresist material can be spread along the surface. Since this coating process was performed using the centrifugal force, the coating will be evenly distributed. During this process, the prevention of bubble formation is required. Soft bake uses application of heat to fix the photoresist material onto the substrate. After exposure, development and hard bake, the pattern of the mask will stay on the base plate where the rest of the part will be washed away. After etching and striping off from the wafer, the separate parts will be positioned and bonded together to form the entire chip.

In this experiment, Protolyne micromachining process technology [45] that comes from Micralyne Inc. was applied. The standard Protolyne chip is as shown in Figure 2.1. It was fusion bonded with two 16mm x 95mm x 1.1mm Schott Borofloat glasses. The channel pattern is etched on the bottom plate, and the top plate contains eight reservoirs at standardized location each having a diameter of 2mm. All the external flow circuits are connected to the chip though these eight reservoirs. The etching depth precision with protolyne technique provided is typically ±2μm and for open chambers it is typically ±5μm.

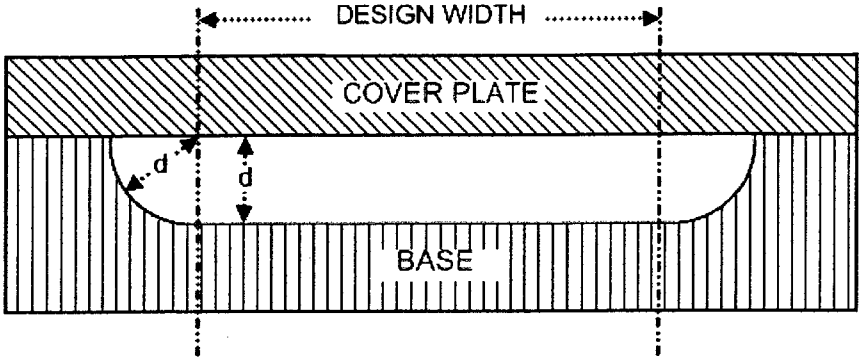

Figure 2. 3 Cross section of channel, d is etch depth

In this case, the etching depth (d) is 20 micron, and the actual diameter of the channel produced in this experiment is increased by about (Figure 2.3):

$$\frac{\pi d^2}{4} \times 2 = \frac{\pi \times 20^2}{4} \times 2 \approx 628 \mu m^2 \qquad (2.1)$$

This increased area due to fabrication tolerance had been taken into consideration in the calculation for both experimental setting and simulations, which is discussed in the following Chapters.

Since the cross section of the channel is not a rectangle, the velocity of the flow is not constant in the whole cross section of channel. Therefore the "velocity" discussed for particular section of the channel is the mean velocity for that section. The cross section is shown in Figure 2.3. In this study, the μPIV method, which is a two-dimensional measurement method, was used for experimental data analysis. Therefore,

the pressure-driven flow velocity profile across the section shows a parabolic distribution, compared to electroosmotic flow field which shows a pluglike flow distribution.

Due to the improvement of the fabrication of the microfluidic circuits, the precision of typical manufacturing method has improved to a degree that under our experimental scale, the dimensions of the microchamber will not be significantly different from the design. Since our experiment focus on the effect of chamber shape on flow velocity distribution, the precision of the chamber shape and dimension become extremely important in terms of significance of the experimental conclusion.

2.6.3 Summary

Nowadays, silicon, polymer and glass are three major materials used for the fabrication of the microfluidic chips. In this study, glass was chosen as the material for the production of the microfluidic chips due to its special optical transparent characteristics. A series of chambers with variety of shapes was designed in a sequential with 75 μm channel. The depth of the microfluidic circuits within the chip is 20μm. Among these chambers, 5 distinct chambers were selected as the representational ones for the study of the microfluidic flow distribution under certain conditions. The circular chamber with a radius of 200μm was chosen as the standard chamber. Two eclipse chambers with the focal points either along the channel axis or perpendicular to the channel axis were chosen for study of the effect of aspect ratio on flow distribution. Furthermore, more complicated chambers (shape IV and V in Figure 2.2) with different curvature and asymmetric inlet and outlet region were used to study the flow distribution and possible dead zones.

Chapter 3

Experimental setup

3.1 Introduction

Particle image velocimetry (PIV) is an optical technique to measure flow velocities in a plane. A typical PIV system consists of a laser as a light source, tiny neutrally buoyant particles that serve as the tracer, a camera to capture the images of the tracer particles, a computer equipped with an image acquisition system to capture and store images, and a pulse generator to control the timing of the laser pulses. In the PIV technique, the tracer particles are added to the flow. The laser pulse illuminates the tracer particles in the region of interest and the camera captures the positions of these particles at that instant of time. A short time (Δt) later, the second laser pulse illuminates the same plane again and the camera records the position of the particles that are shifted in the direction of the flow. This way a sequence of image pairs is obtained. Later, each of the image pair is processed to obtain the velocity field. In the processing step, the first image of the image pair is divided into small interrogation windows and the second image of the image pair is divided into search windows. The average particle shift in the interrogation window is estimated by cross-correlating the interrogation

window in the first image with the corresponding search window in the second image. The correlation peak provides the average particle displacement within the interrogation window. The average velocity in the interrogation region is obtained by dividing the particle displacement by the time delay between the two images (i.e. Δt). The same approach is applied to all the interrogation regions and hence a velocity field is obtained. A PIV image with the resolution of 1600 pixels x 1200 pixels is typically divided into about 7000 interrogation windows i.e. about 7000 velocity vectors are obtained simultaneously within the measurement plane. The μPIV system shares the same principle as the macroscopic PIV [46]. However, certain micro particle image velocimetry (μPIV) system configuration is unable to measure directly the flow distribution under certain threshold flow rate, mainly caused by the following reasons:

1) *The dimension of the trace particle*: Macro scale PIV uses particles with a dimension of tens to hundreds of microns, and they accurately represent the real flow velocities. Whereas, the particle diameter should not be more than a micron in the μPIV setup.

2)) *Optic resolution ratio*: Since the dimension of the particles used for studying micro-flow distribution is selected under the micrometer to submicron level, the magnification of the regular camera is too low to catch these small particles and therefore, could not be directly used for these studies. Hence, a microscope is used to enhance the magnification.

3) *Light source*: In conventional PIV systems the laser produces a light sheet. However, due to the smaller dimensions of the microfluidic chip, the measurement volume is illuminated by the light rather than illuminating the measurement plane. Thus, the light delivery optics in μPIV system are different from the standard PIV systems.

4) *Brownian motion*: In macroscopic PIV, these factors are so small so that they could be ignored. However, in μPIV, since the dimension is considerably small, the effect of Brownian motion is significant and may cause errors in the measurements.

In 1996, Brody [20] improved the μPIV method for tiny analytic pipeline in his study. He used an intensified CCD camera to image particle streaks in an 11x72 μm silicon channel. In 1998, Santiago et al. [46] from the Stanford University developed a method, which considered errors due to particle diffusion resulting from Brownian motion. A first order estimate of this error relative to the displacement in the x-direction is given. In 1999, Meinhart et al. [21] used impulse Nd: YAG laser at 200nm wavelength light to fluoresce polyphenyl alkene particles, the effective particle image size was low to 5.5 pixels. In 2003 Devasenathipathy et al. [22] studied flow field in cross-point of cross shaped channel with μPIV.

3.2 Composition of the system

3.2.1 Fundamental and basic components

A μPIV system is composed of a microscope, CCD camera, lighting source and a flow circulating system. The fluorescent particles which serve as the tracer particles, are mixed in the flow. Fig. 3.1 shows the main components of the μPIV system. The schematic of the μPIV setup is shown in Figure 3.2. The light delivery mechanism is also shown in the figure.

The light delivery and image acquisition schematic used in the classic micro PIV setups are shown in Figure 3.3. In these setups, the light is delivered vertically to the measurement volume through the microscope. Since the intensity of laser light is usually

high, this setup could damage the optical lenses and filters of the microscope. A novel approach is used in the present setup in which the laser light is delivered external to the microscope, directly to the chip at an angle of 45° (see Figure 3.4). Since the boric glass was used as the fabrication material here, the refractive index is 1.65. Therefore, the actual incident angles experienced by the particles are 27.3°. In this case, the advantage of changing the incident optical path is that, the incident light and the emission light do not have the same optical path, and therefore prevent the possibility of damaging the coating of the optical filter. Also, it can prevent the degradation of the intensity of the excitation light when it reaches the particles. More detailed discussion will be followed later in this chapter.

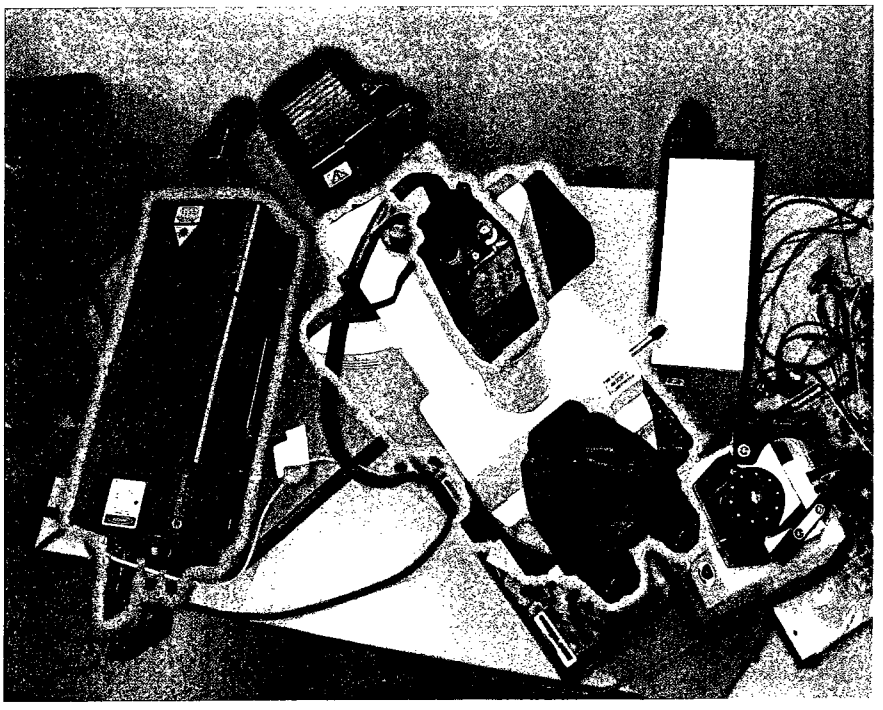

Red: Iris Diaphragm
Green: Laser
Yellow: High Speed Camera
Violet: UltraViolet Lightsource
Cyan: Epifluorescence Microscope
Blue: Peristaltic Pump

Figure 3. 1 Setup for μPIV experimentation

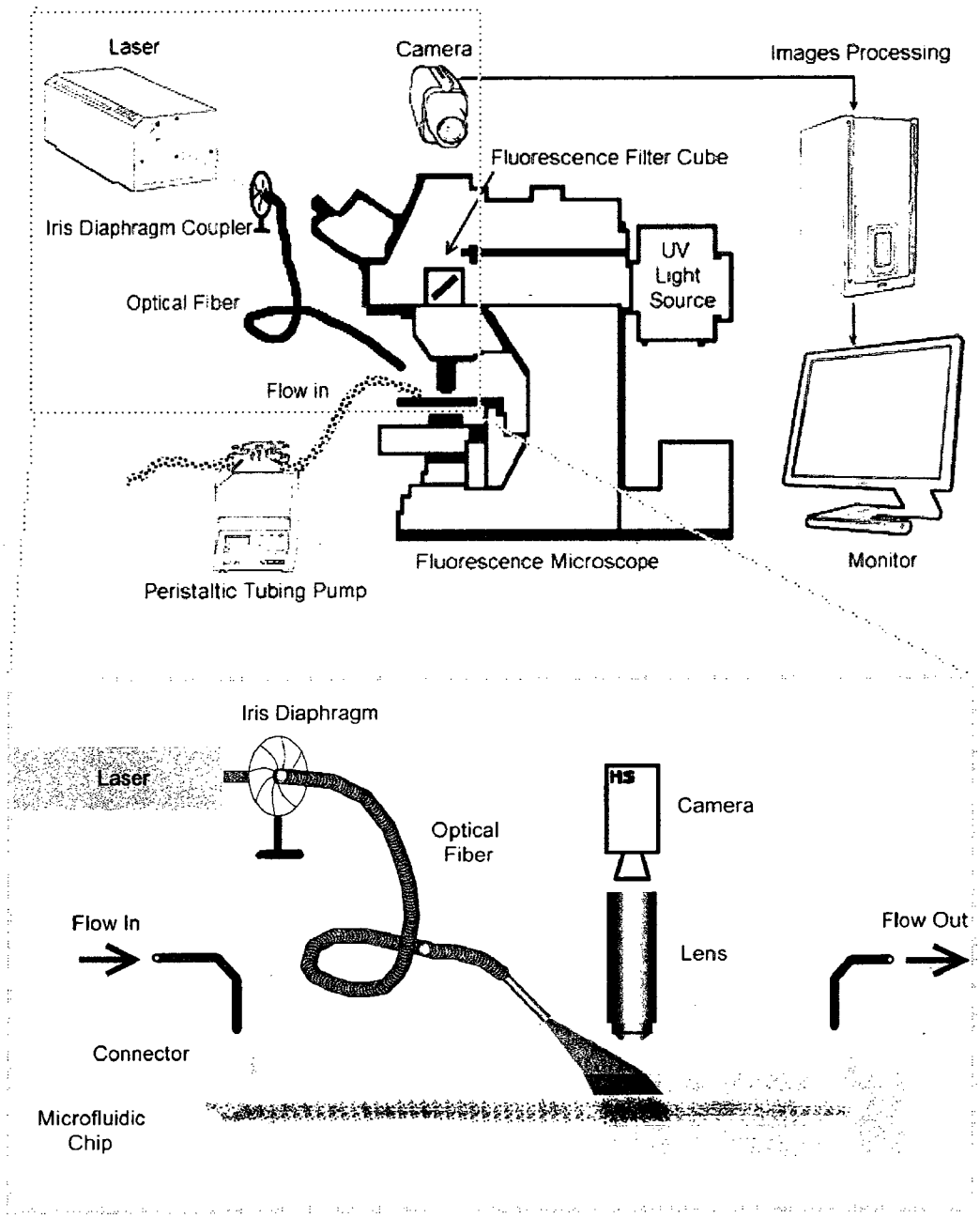

Figure 3. 2 Schematic of μPIV setup

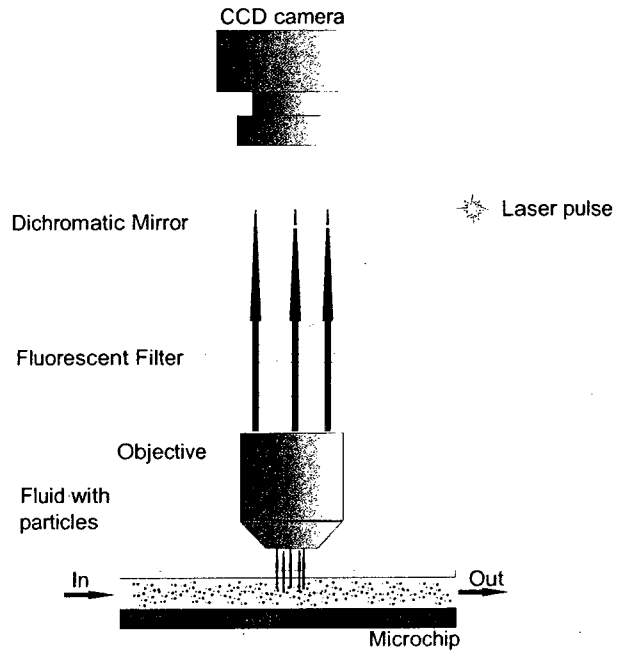

Figure 3. 3 Optical detection setup used in other studies by μPIV

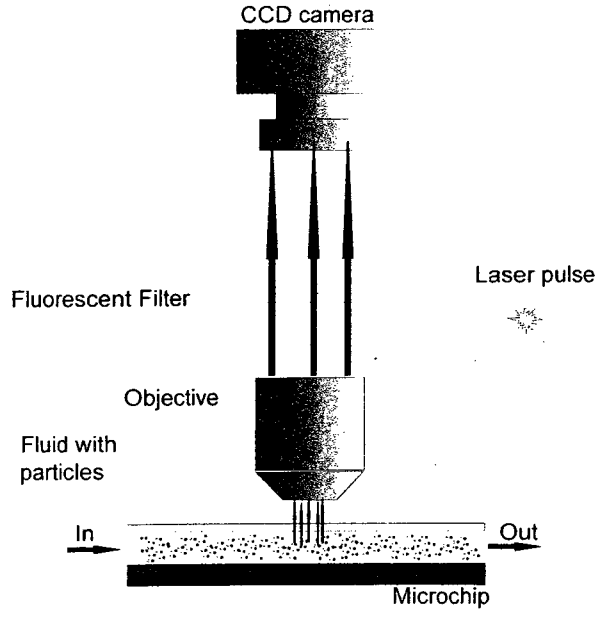

Figure 3. 4 Optical detection setup for μPIV used in this study

3.2.2 Particles

The particles used in this study are spherical with their surface coated with fluorescent material. The fluorescent material is excited by short wavelength light from the light source and it emits fluorescent light with longer wavelength. Since the high energy transition state after excitation is unstable, the excited electrons would return to the ground-state and release the energy during this process. These energies are released as the form of light with longer wavelength (smaller energy) comparing to excitation light from the light source.

The fluorescent light intensity emitted is normally very weak and is calculated by Beer–Lambert law [47]:

$$F = 2.3 Y_F I_o \varepsilon l c \tag{3.1}$$

Where Y_F is fluorescence quantum yield; I_o represents the light source optical power in the unit of Watts/ cm^2. ε is the molar absorption coefficient. l represents the thickness of the channel, c is the concentration of fluorescence matter in the solution.

Different kinds of fluorescence materials have a different excitation spectrum which means that the peaks of the excitation spectrum have different wavelengths. The peak of the excitation spectrum represents the maximum absorption coefficient for certain materials. For instance, the quinine sulfate has a maximum absorption at 350nm and the rhodamine 6G has a maximum absorption at 525nm. Similarly, every single fluorescence material also has different emission spectrum. At the peak of the emission spectrum, the corresponding fluorescence intensity is maximized. The quinine sulfate's fluorescence peak is at 470nm and the fluorescence peak of rhodamine 6G is at 555nm. However, compared to the excitation light, the emitted fluorescence is so weak, and in

order to get a fairly good observation result, the light source used for excitation should give a wavelength of light very close to the peak of the excitation spectrum and the photosensitive component should have the highest sensitivity around the emission peak of fluorescent material.

In order to have the best representation of the flow field, the size of the particle has to be small enough to avoid influences on the behavior of the flow. But smaller the particles, higher optical resolution is required to detect them. On the other hand, smaller particles diffuse faster than bigger particles and therefore affect the precision of the measurements since diffusion is independent from the flow behavior.

Moreover, particle is also under molecular thermal motion which is Brownian motion in the solution. Such a movement is a random diffusion and the distance of diffusion which is exponential to the diffusion time can be calculated by the following formula [48]:

$$S = \sqrt[2]{2Dt} \tag{3.2}$$

Here, S is the distance of diffusion, D is the diffusion Coefficient, which is inversely proportional to the size of the particle and fluid viscosity, and proportional to the temperature of solution, t is the diffusion time.

Since the error comes from the Brownian motion is random, it obeys the Gaussian distribution and the effect can be reduced by averaging the results from multiple images at the same location [46].

In the present experiment, we chose R0200 particle, procured from Duke Scientific Inc, with fluorescent excitation wavelength of 542nm, and emission wavelength of 612nm (see Figure 3.5). Duke Scientific Inc. provides polymer made particles with

three kinds of coating material that gives different excitation and emission spectra. The reason that such a particular particle has been selected is that the particle has a density of 1.06g/cm^3 which is very similar to the density of pure water, and therefore water was selected as the working fluid in this study. Moreover, the laser light source used in this experiment provides only two specific wavelengths at 266nm and 532nm. Since the laser light used for excitation is not exactly at the peak of the excitation spectrum of the particle, the particle is not emitting the maximum amount of emission light. However, since the excitation spectrum and emission spectrum is not overlapping at 532nm, the incident light was set by passing the excitation filter. The actual size of the particle used in this experiment was about 2 microns in diameter.

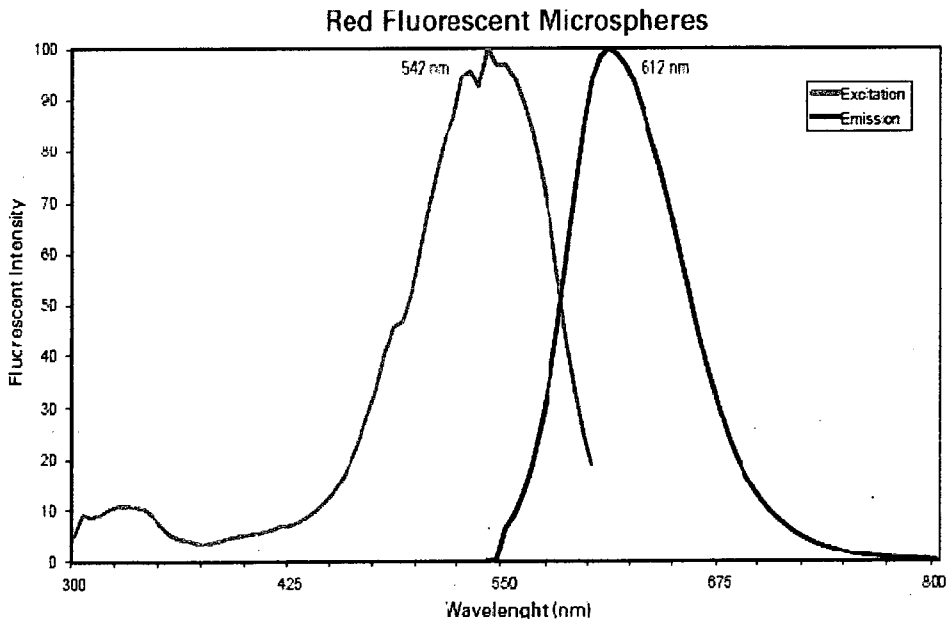

Figure 3. 5 Excitation and emission spectrum of the R0200 fluorescent particles used in this experiment [49]

3.2.3 Light source

Since the excitation spectrum is different for different materials, different excitation light sources are selected in different cases. The commonly used excitation light sources include: Mercury lamp, tritium light, Nd:YAG double pulsed laser.

Compared to other light sources, the mercury lamp gives a broader wavelength range of light. With the help of different light filters, ultraviolet light, blue light, and red light can be separated. The disadvantage of mercury lamp is that it produces lower intensity compared to other light source and therefore gives a weaker stimulation. In order to compensate, increasing exposure time have to be used, but under high flow rate, the long exposure time will cause the formation of a trail.

Nd: YAG double pulsed laser is the most commonly used light source in μPIV applications. After synchronization, the wavelength can be selected at 532 nm which lies on the peak of the excitation spectrum of some of the fluorescent materials. The pulse width is fixed in the range of 6-9 ns and the time delay between two pulses typically varies between 50μs to 30 ms. With the help of the pulse generator, the laser generator can be synchronized with the camera. Because the Nd:YAG laser intensity is very high, it can cause damage to equipments and the samples. To prevent this, the direct focus is prohibited or it is defocused before detection.

Since fluorescence intensity is proportional to the light intensity of the laser light source, both fluorescent signals and background noises are increased with the intensity of light. Besides, the laser light source has its own maximum power and intensity and the fluorescent materials also contain a maximum absorption limit where the emission intensity will not increase with the increasing of excitation intensity anymore. Normally,

the power required to excite the fluorescent light is under 1milli Watt. The formulas for calculating the energy of the laser are:

$$P_p = \frac{E}{t} \tag{3.3}$$

Here P_p is the peak power in watts, E is the energy per each pulse in Joule, t is the length of the pulse in seconds.

$$\bar{P} = E \times f \tag{3.4}$$

$\bar{P}$ is the average power, and f is the repetition rate in Hertz

$$D_P = \frac{P}{\pi r^2} \tag{3.5}$$

D_p is the density of the power, P is the power and r is the radius of the laser spot.

For the present experiments, SoloPIV 120XT Nd:YAG double pulsed laser generator from New wave Research Inc. was used. The main parameters of the laser are given in table 3.1. The frequency of the double pulsed laser is 30Hz and the interval between the two laser pulses adjacent to each other is synchronized with the camera.

Model		Solo 120XT
Repetition Rate(Hz)		15
Energy(mJ)	532nm	120
	266nm	20
Energy Stability Between Pulses(±%)	532nm	4
	266nm	9
Beam Diameter(mm)		5
Pulse Width(ns)		3 to 5
Divergence(mrad)		<3

Table 3.1 Parameters of the laser used in this study.

3.2.4 Microscopes

The fluorescence microscope used in μPIV is the micro imaging optics equipment with certain adaptation. The major parameters for the microscopes are magnification rate, numerical aperture, the work distance, focal depth, resolution, and field number etc. The relationship between these parameters is shown as below:

$$NA = n \sin\frac{\theta}{2} \tag{3.6}$$

NA is the numerical aperture, n is the index of refraction of media between objective lens and the object; θ is the angle of divergence. The bigger the angular aperture, the more of the light can enter the objective lens. This parameter is proportional to the diameter of the objective lens, but inversely proportional to the distance from focal point. In practice, increasing angular aperture is impossible. Therefore, in order to increase the aperture number, the index of refraction has to be increased. For example, oil is used in biological microscopic application to increase the refraction index in order to increase the numerical aperture to 1.4, which is 1 when air is used as the medium.

In addition,

$$R = \frac{\lambda}{NA} \tag{3.7}$$

R is the diameter of the light source. λ is the wavelength of the light entering the lens. Since the wavelength of light is defined, the smaller the R value, more details of the object can be obtained.

$$F = \frac{F_N}{M} \tag{3.8}$$

F is the size of field of view, F_N is the number of field of view, and M is the magnification. Therefore, the bigger the field of view, the larger actual area could be detected.

The focal depth is calculated as,

$$F_D = \frac{n\lambda}{NA^2} + \frac{nd_p}{M*NA} \tag{3.9}$$

n is refractive index, d_p is the size of the CCD pixel. Smaller the F_D (focal depth), fussier the out-of-focus level of image is.

The most important role of EPI microscope is the separation of excitation light and emission light. If the object cannot be distinguished from the background, it is impossible to detect these particles. The principle illustration diagram is show in Figure 3.6. The separation of excitation light and emission light is fulfilled by using a cube which includes excitation light filter, spectroscope, and emission light filter.

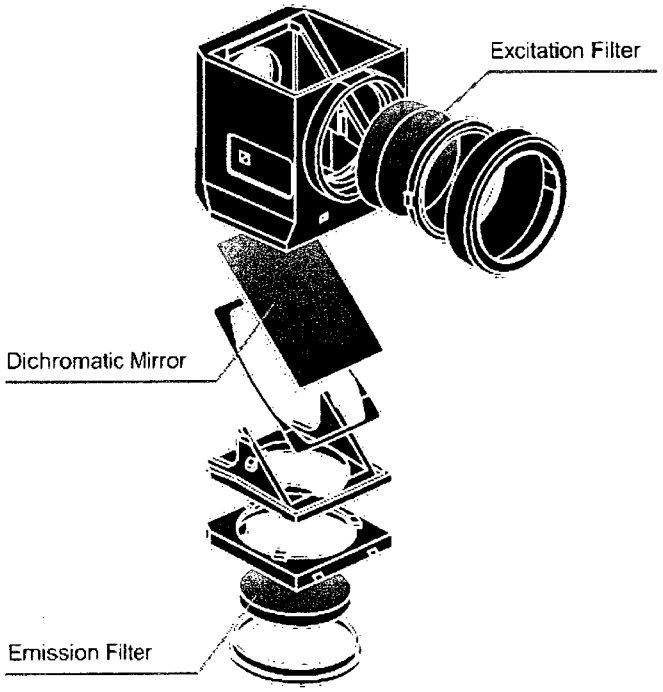

Figure 3. 6 Principle of fluorescence filter cube

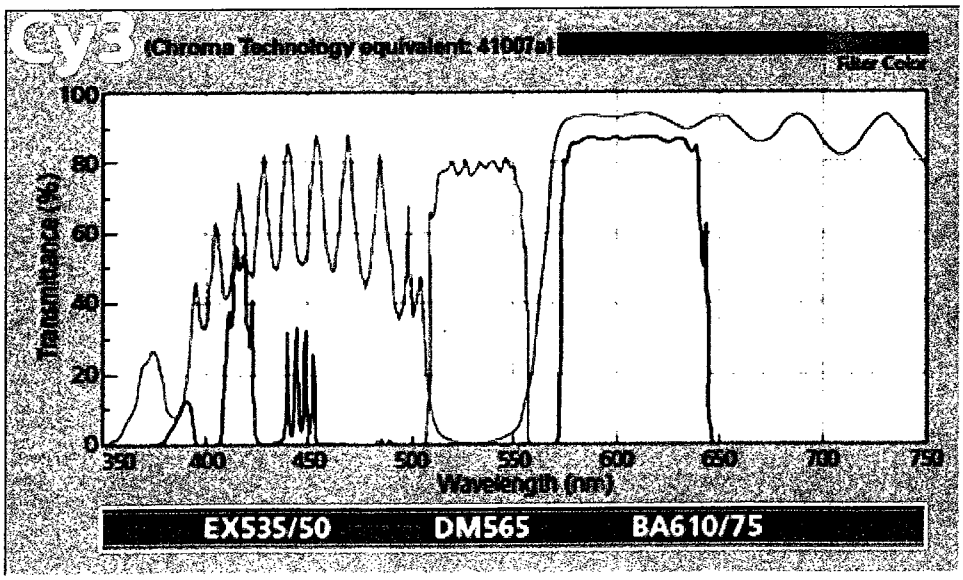

Figure 3. 7 Spectrum of excitation filter and emission filter Model Cy3 [50]

The role of excitation light filter is to band pass the light with the wavelength close to the peak of the excitation spectrum of the fluorescent materials used. The wavelength spectrum used in our experiment is as shown in Figure 3.7. The role of spectroscope is to selectively reflect the excitation light with the wavelength selected to the objective lens. The emission light filter is used to exclusively pass the fluorescent light and therefore further increase the definition of the fluorescent image.

In this experiment, Nikon EPI 55i fluorescent microscope was chosen with 10X objective lens. The special characteristic of this microscope is the fluorescent filter which makes it suitable for the observation of fluorescent signals from the biological samples. The filter is made of a thin glass layer which is coated with special optical materials. Depending of the materials, the filter is classified into band-pass and band-stop which allow special range of light wavelength to be either passed (band-pass) or blocked (band-stop). The coating materials themselves have specific characteristics which make it possible to transmit, reflect and absorb wavelengths of light with different proportions. Moreover, the material can also behave differently towards different wavelength of light. Even though the materials that were coated on the filter surface are very thin and the amount of light energy observed by this layer is low, the filter could still be damaged if the energy of light used for excitation goes beyond a threshold value depending on the configuration. In previous studies, directly changing of the microscopic light source to laser was used but in our case, since PIV require continuously exposure, the filter of the microscope may accumulate high thermal energy during the process and damage coating of the filter. In order to avoid this problem, the amount of energy produced by the laser was calculated according to the Equations 3.3 to 3.5. The threshold energy for destroying the filter is determined by the peak power of the laser. The adjustable parameters for the laser light source are the frequency of the laser pulse, the wavelength

and the length of each pulse. However, the laser light source used in this experiment is non-adjustable on wavelength. According to the formulas, changing frequency of the laser pulse and length of each pulse can only change the average power but not to reach the peak power. Therefore the optical fiber was used to change the illumination light path so that it goes directly onto the chamber without passing through the filter of the microscope.

3.2.5 The limitations of CCD

Charge Coupled Device (CCD) is a charge coupling device, which converts optical signal into electric signal. One of the most important parameter for CCD is its resolution. Resolution indicates the ability of the camera to differentiate in detail the contrast of image, which in the case of digitalized camera, is represented by the number of pixels in each dimension. The more pixels there are on the CCD chip, the better resolution will the camera have. The best CCD by far, has a pixel dimension of 4.65 μm. However, most of the high resolution CCD gives grayscales images. The ways of obtaining the RGB colorful picture is by first using certain light filter or prism to separate three-primary colors (red, blue and green) and then combine them into different optical channels which give the colorful images.

Another important parameter for CCD is the dynamic range. It is the recording range of hue by CCD. Regular CCD contains a dynamic range of 8 bits to 16 bits. For instance, a CCD with 8-bit dynamic range means that it can differentiate as many as 2^8 or 256 different gray scales from black to white. This parameter is especially important when the detected light is weak.

In the application of μPIV, the CCD apparatus, which is a Digital Monochrome 2 Megapixel Progressive Scan Camera (CV-M2) from JAI PULNiX Inc., must be synchronized with the laser light source in order to maximize the intensity of the fluorescence. The camera frame rate and the laser pulses are synchronized via a pulse generator. In PIV measurements, the camera shutter remains open all the time. As soon as the laser pulse illuminates the measurement plane, the image of the tracer particles is recorded by the camera sensor. The time delay between the two laser pulses is set in a way that the maximum particle shift from image 1 to image 2 of an image pair must be less than one-half of the dimension of the interrogation window. In the present study, the size of the interrogation window was set equal to 32 × 32 pixels. Thus, the time delays between two laser pulses for different cases were set in a way to keep the maximum particle shift less than 16 pixels.

3.2.6 Peristaltic tubing pump

This experiment uses pressure driven system which was performed by peristaltic pump from Gilson Inc. The model used in this experiment is Miniplus 3. It is a low pressure peristaltic pump which is designed for microfluidics to produce flow with negligible pulsation and consistent flow rate. The pump head spinning speed is controlled by a keypad. The output spinning speed is displayed on the LCD display beside the keypad. The flow is produced by a high-torque stepper motor which drives a series of rotatable rollers to press the tubing and therefore create the flow. The range of the spinning speed is controllable between 0.01RPM and 50RPM. The smallest adjustable scale is 0.01RPM. The user's guide indicates that the output flow rate ranges from 0.3μL/min to 30mL/min within PVC tubing [51].

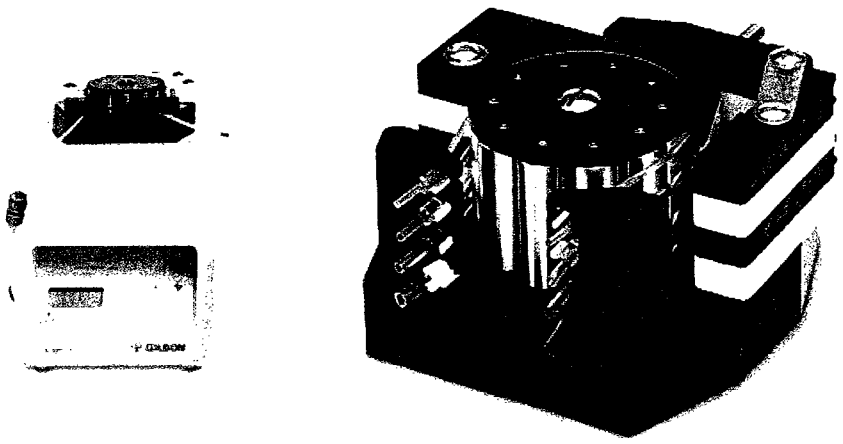

(a) (b)

Figure 3. 8 Photograph of peristaltic pump (a) external appearance and pump head (b)

In this experiment, the PVC tube used has an internal diameter of 0.5mm. The flow rate according to the user's guide is the reference rate in the PVC tube without any other apparatus connecting to it. However, after connecting to the experimental chip, the measured flow rate is different from the reference value from the user's guide. Figure 3.9 compared the experimentally measured velocities to the reference velocities from the user's guide. The difference between the experimental measured flow rate and the reference flow rate is about 6.3%. In order to produce an initial velocity right before entry into the chamber of 1.594mm /s, 4.781mm /s, and 7.969mm /s, the pump output spinning speed was set at 0.01RPM, 0.03RPM and 0.05RPM respectively.

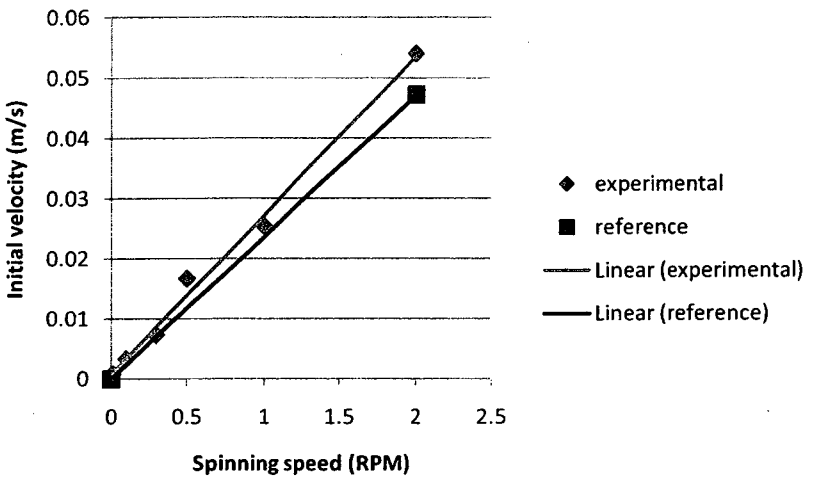

Figure 3. 9 Comparison between experimental velocities and reference velocities of the users' guide in PVC tube with 0.5mm internal diameter

Microfluidic connection is the tubing that connects the microfluidic circuits to the external devices. It is a problematic tubing system which is often the reason of experimental failure. So far, there is no common agreement on the standardized solution for certain situation.

For microfluidic chips based on polymers, holes can be made on the surface of the chip for the insertion of tubes with correct size. Adhesives can then be used to seal the connections. This way, garenteed water proofness can be achieved. However, the adhesives can get into the microchannels and change the shape of the channel or even block it. For glass or silica based chips, if epoxy resin is used as the adhesive to connect the slack tube on the extent surface of the chip (Figure 3.10), an inflexible structure has to be used to make sure the connection part can both resist to the internal pressures within the microchannel and evenly distribute the external drawing force on the tube. In

practice, the major reason for the failure of the adhesive connection is due to the external drawing force which pulls the tube and break the connection. Nowadays, new methods use certain device which applies high pressure on the connection region that seals (Figure 3.11). Up to 200 psi pressure drop can be operated in this way. However, this device occupies a big surface area on the chip, and is also very expensive in price. Generally speaking, connection with adhesives can provide good water proofness less expensive prices. Therefore, in this experiment, thin adhesive material layer was used. The connection area is about 0.34mm^2 and the working pressure drop can reach over 3.6 psi in experiment.

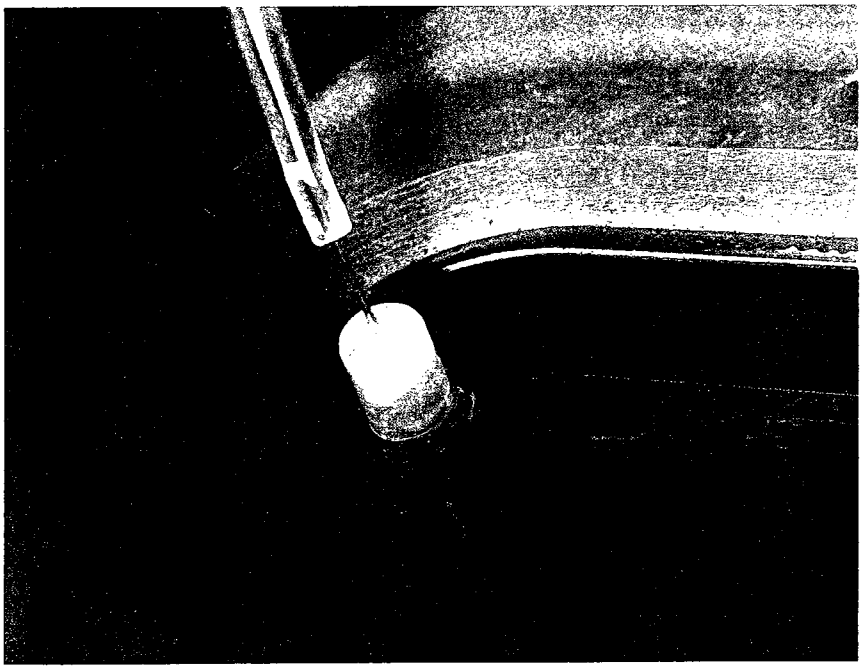

Figure 3. 10 Connector and glass chip joined with epoxy resin cement

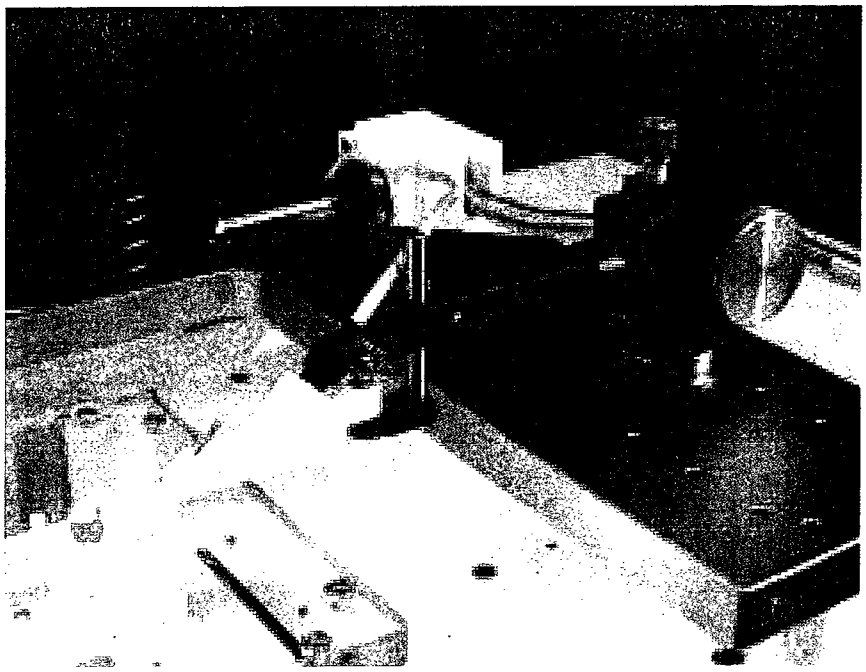

Figure 3. 11 L-serial connector from Cascade Microtech Inc.

3.3 μPIV parameter determination

3.3.1 Model of μPIV system

Assume that the size of field of view (FOV) is 'm' pixels times 'm' pixels, the entire system resolution is $C=m^2$, the microscope objective lens magnification power is K, the microscopic resolution is C_m, the CCD pixel dimension is d, the size of CCD die is L times H, C_p is image display resolution which represents the actual length on the measured objective shown between two adjacent pixels as in Figure 3.12.

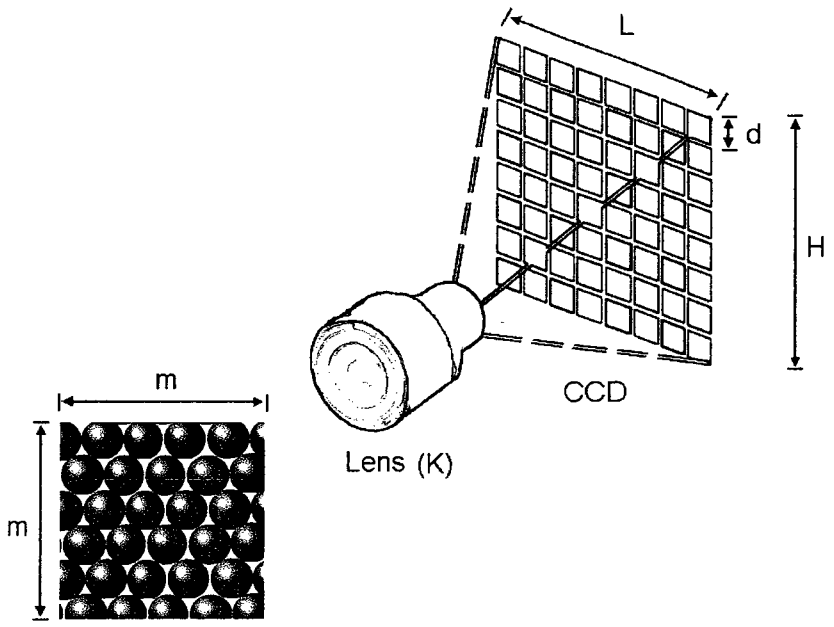

Figure 3. 12 Field of view and CCD dimensions

The size of the image under microscope is:

$$S_m = (mK)^2 \tag{3.10}$$

The size of image projected on CCD can be calculated under two different cases:

If mK * mK is greater than L * H,

then S_c= L * H, otherwise $S_c = (mK)^2$

The displaced objective size on the monitor (based on number of pixels) is:

$$S_p = \frac{S_c}{d*d} \tag{3.11}$$

Therefore, the screen resolution (based on microns) is:

$$C_p = (\frac{d}{K})C_m \tag{3.12}$$

The possible theoretical error within these calculations can be calculated as below:

$$\text{When } C_m K \geq d,\ \Delta = C_m - C_p * n_1 \tag{3.13}$$

$$\text{When } C_m K < d,\ \Delta = C_m * n_2 - C_p \tag{3.14}$$

Where n_1 is the maximal positive whole number that can make $\mathbf{C_p * n_1}$ less or equal to C_m , n_2 is the maximal positive whole number that makes $\mathbf{C_m * n_2}$ greater or equal to C_p .

After considering systematic error, the entire system resolution is:

$$C = C_P \pm \Delta \tag{3.15}$$

In this experiment, the actual resolution is 1608 (h) x 1208 (v) pixels. The 2 megapixels camera has an 11.8 (h) x 8.9 (v) mm CCD sensing area. The exposure timer for the camera is programmable, and the minimum exposure interval between two adjacent frames is within 0.002sec which means the dynamic range of the CCD used in this camera is very high. The exposure intervals respectively used in this experiment for initial velocities right before entry into the chamber are listed in Table 3.2.

Initial velocity	1.594mm /s	4.781mm /s	7.969mm /s
Exposure intervals	$6x10^{-3}$sec	$4x10^{-3}$sec	$2x10^{-3}$sec

Table 3. 2 Exposure intervals respectively used for initial velocities

3.3.2 Optical resolution

The objective lens resolution can be expressed as,

$$d_0 = \frac{\lambda}{NA} \tag{3.16}$$

Where d_0 represents the minimum distance between two separated light sources that can be distinguished by the objective lens. If the distance between two light sources is shorter than d_0, the two light sources will be treated as one. The minimal optic resolution is limited to 0.2um.

The particles image detected on focal plane contains the magnified actual particles' image and a diffraction ring. Therefore, the diameter of the particle image is slightly larger than the actual magnified particle dimension. And these two diameters can be estimated by the following approximate formula,

$$d_I = (M^2 {d_p}^2 + {d_s}^2)^{\frac{1}{2}} \tag{3.17}$$

$$d_S = 1.22(1 + M)\lambda/NA \tag{3.18}$$

Where d_I is the diameter of particles' image; d_p is the particles diameter; d_s is the diameter of the diffraction ring; M is the magnification power of objective lens; λ is the wavelength of the emission light; NA is the numerical aperture.

In this experiment, the diameter of the particles is 2 μm as well the dimension of a pixel in images is 4.65 μm. Under a 612nm wavelength, d_I was calculated by the above formula and shown in the following Table 3.3:

M	NA	d_I(micron)	d_I(pixel)
10x	0.3	31.086	6.685
20x	0.4	52.546	11.300
60x	0.6	136.946	29.451

Table 3. 3 particles' image diameter

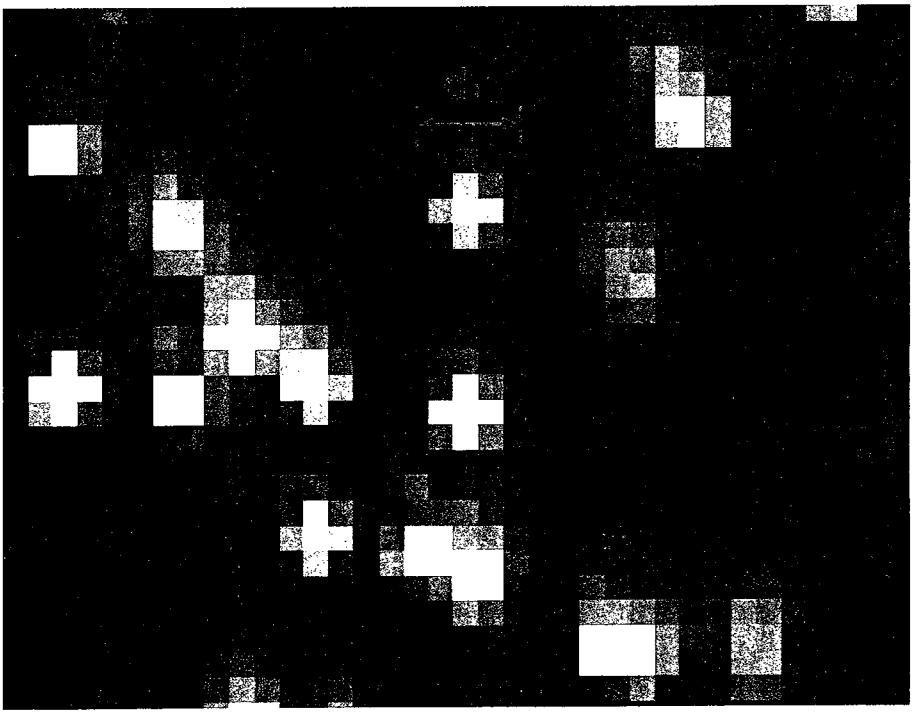

Figure 3.13 Particles image (10x objective lens)

Based on the above results, the diameter of diffraction ring d_s is greater than objective lens resolution (d_0), therefore, individual particles can be identified separately.

Moreover, according to Table 3.3, when 10 times magnification objective lens has been used, every particle would have a size about 6 pixels (Figure 3.13). Such a size is big enough to be identified from the background, and therefore it fulfills the requirement of the experimental setup.

As shown in Figure 3.14, the high speed camera, which works at 30Hz ($1/t_3$), takes a pair of photo of the illuminated particles at two determined times precisely, separated by Δt (t_1). The time separation Δt is the most important adjustable variable in a μPIV system, as it determines the maximum and minimum velocities that can be measured. The laser pulses (t_2) have to be synchronized with it. The duration of the laser pulses, determines the brightness of particles during the pulse exposure. The displacements of the particles during Δt can be measured if the images corresponding to the same particles can be recognized in the two pictures. These displacements are thereafter used to calculate the average velocities of the particles according to the formula $D/\Delta t$ where D is the displacement of the particle.

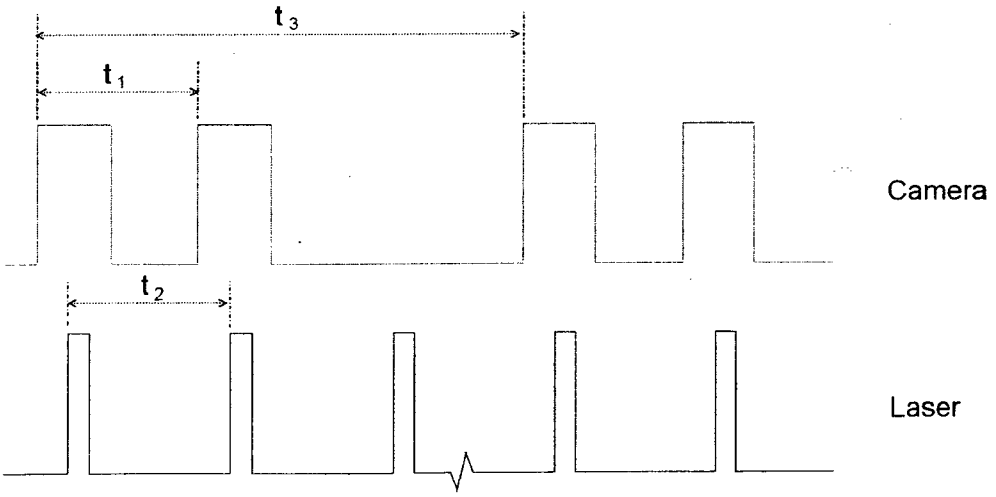

Figure 3. 14 sequential chart of μPIV

3.4 Application of cross correlation algorithm in velocity measurement using particle imaging

There are many different algorithms used in the analysis of two dimensional velocity field based on continuous image capture. This experiment uses Heurisko software [52] from AEON Verlag & Studio to compute the velocity field from the μPIV images.

Block-matching method is the least complicated and most commonly used algorithm. It separates the first image into several different blocks, and then uses the matching rule to search the most similar block in the second image comparing to the template block selected from the first image. Once the matching block has been found, the displacement between the two blocks can be used to calculate the vector of velocity. The most commonly used matching rule includes mean square function (MSE), minimal D-value function (MAD) and maximal cross-correlation function (CORR) etc.

The MSE function's evaluation criterion is

$$\mathrm{MSE}(d_1, d_2) = \frac{1}{N_1 N_2} \sum_{(n_1,n_2)\in B} [S(n_1, n_2, k) - S(n_1 + d_1, n_2 + d_2, k+1)]^2 \qquad (3.19)$$

Here, B represents the N1 * N2 block, which could be chosen as the set of vector (d1, d2). The Estimation of the minimum value of (d1, d2) is:

$$[d_1, d_2]^T = \arg\min_{d_1,d_2} \mathrm{MSE}(d_1, d_2) \qquad (3.20)$$

The mean absolute deviation(MAD) function evaluation criterion is :

$$\mathrm{MAD}(d_1, d_2) = \frac{1}{N_1 N_2} \sum_{(n_1,n_2)\in B} |S(n_1, n_2, k) - S(n_1 + d_1, n_2 + d_2, k+1)| \qquad (3.21)$$

$$[d_1, d_2]^T = \arg\min_{d_1,d_2} \mathrm{MAD}(d_1, d_2) \tag{3.22}$$

Maximal cross correlation function evaluation criterion is:

$$\mathrm{CORR}(d_1, d_2) = \sum_{n_1,n_2 \in B} S(n_1, n_2, k) * S(n_1 + d_1, n_2 + d_2, k + 1) \tag{3.23}$$

In order to get the maximal value of the CORR(d1, d2):

$$[d_1, d_2]^T = \arg\max_{d_1,d_2} \mathrm{CORR}(d_1, d_2) \tag{3.24}$$

According to all three functions, the velocity vector of the whole captured region can be calculated as:

$$\vec{V}_{(n1,n2)} = \begin{bmatrix} d_1/\Delta t \\ d_2/\Delta t \end{bmatrix} \tag{3.25}$$

The cross correlation algorithm is most commonly used processing method in μPIV applications. This method uses similar fundamental principles as block matching. In order to calculate the average velocity of the entire flow field, the different averaging mathematical methods can be used.

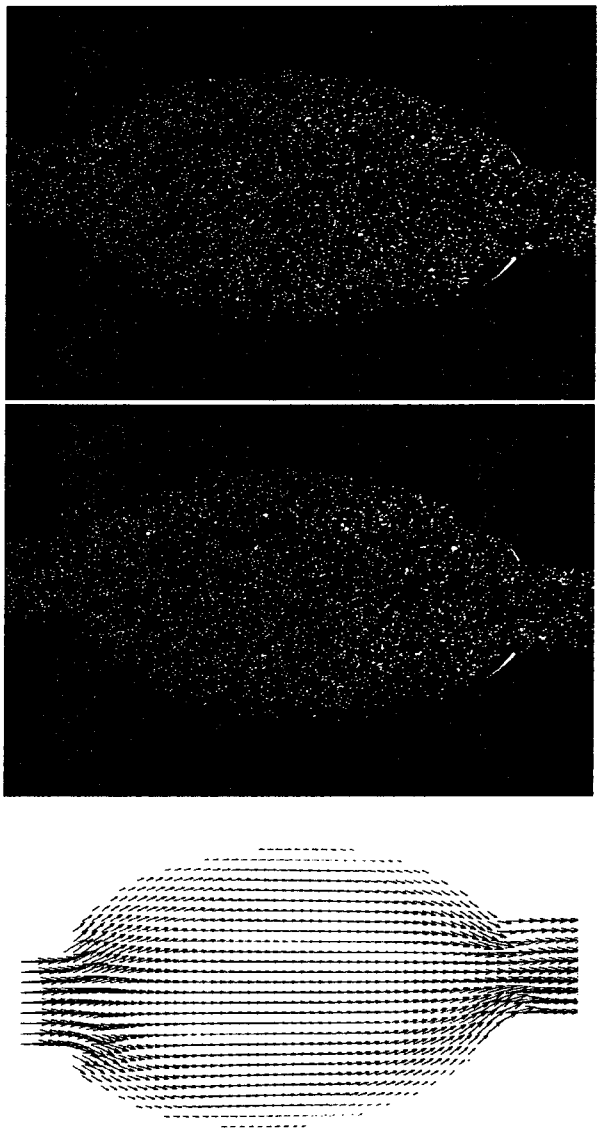

Figure 3.15 Estimated velocity field of Shape II at flow rate of 23.9e-3 mm3/s (Re = 3.44e-1) using image pairs A and B separated by t_1 = 0.002 sec

Figure 3.15 shows an image-pair and its μPIV result. Analysis software calculates the particle displacement between the two images by partitioning the image into smaller windows, which named interrogation window. Based on this displacement, the velocity field is calculated.

The μPIV velocity is essentially a measure based on statistics. There is an inherent statistical error between real flow field and its result. To consider the type of error expected in PIV measurements, the total error is the sum of all errors that include velocities gradient biasing, tracking biase rely on sub-pixel fit estimators and random noise from various sources (e.g. light quantization, CCD dark current, particle blocking, etc).

The PIV Challenge used following three parameters to evaluate PIV results [53]:

The first is signal noise ratio (SNR), the best result was 33%. The average result between various research institutions was 20%. Another parameter is the Root Mean Squared error (RMS error), and the best value is 0.04. The average result between various research institutions was 0.08. The third parameter is Convergence towards high confidence level. The best result of research institutions close to 90%. The average result was 70%.

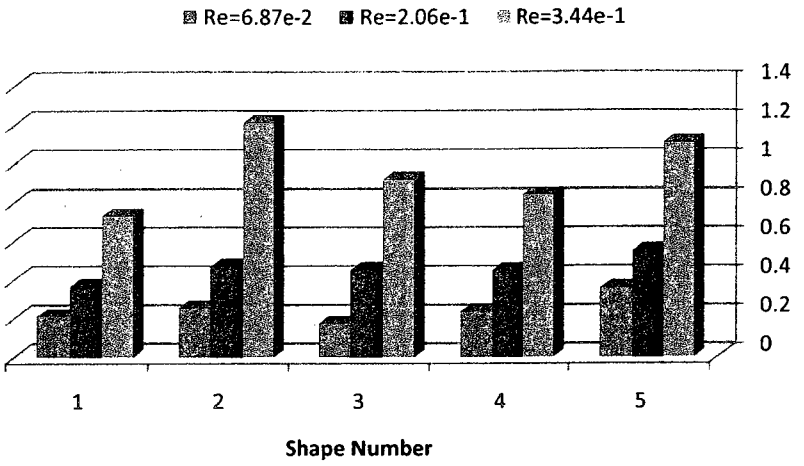

Figure 3. 16 RMS error along y=0μm section under different flow rates for shapes I, II, III, IV and V

To quantitatively compare oblique illumination method against simulation, Figure 3.16 shows the RMS (Root Mean Squared) error in velocity measurement along the x axis for the 5 shapes at 3 different flow rates. The error increases with the flow rate. At this cross-section, the errors are the least for circular chamber.

3.5 Summary

In this Chapter, the oblique illumination experimental setup for μPIV system was discussed. Compared with classic perpendicular method, oblique illumination method reduces the luminance loss to about 30% by reducing the optical path. It is also less costly than the classical perpendicular illumination method. The major parameters for the experimental setup have been calculated and analyzed. These calculations examined the possibility and feasibility of the platform setting and discussed further the mathematical algorithm for μPIV. In this study, 532nm laser light was used as the

excitation light source under 10X objective lens, with an overlap setting as 50%. Therefore the testing flow velocity can reach 2.97×10^{-1}mm/s, and results are highly accurate compared to the simulation. In practice, by using peristaltic tubing pump, the flow velocity reaches 1.594×10^{-1}mm/s within the detection region, and therefore the experimental platform setting fulfilled the requirement of study. For connection was employed, the method using adhesives that have lower maximum resistant pressure drops. However, by using direct adhesion on plastic level with larger connection area, the maximum pressure drop can reach over 3.6 psi.

Chapter 4

μPIV Experimentation

4.1 Introduction

The PIV technique and the components of the μPIV system used in the present study are described in Chapter 3 along with the other components of the experimental setup. This chapter is focused on the experiments and the experimental results.

4.1.1 Experimental Conditions

Experiments are conducted for five different micro-chamber shapes, such as: shapes I, II, III, IV and V. For each shape, the velocity measurements are made at three flow rates which are $4.782 \times 10^{-3} mm^3/s$, $14.34 \times 10^{-3} mm^3/s$, $23.91 \times 10^{-3} mm^3/s$. The working fluid is distilled water. The corresponding Reynolds numbers can be calculated as follows,

$$R_e = \frac{Q}{w\nu} \tag{4.1}$$

Where Re is Reynolds number, Q is the flow rate, w is the channel width and v is the kinematic viscosity of water. Ambient temperature detected in laboratory is 26°C; the corresponding kinematic viscosity of water is $0.928 \times 10^{-6} m^2/s$. These parameters are shown in Table 4.1.

Flow Rate (mm^3/s)	Channel Width (μm)	Reynolds Number	Chambers				
			I	II	III	IV	V
0.00478	75	0.069	√	√	√	√	√
0.01433	75	0.206	√	√	√	√	√
0.02391	75	0.344	√	√	√	√	√

Table 4.1 Test flow rate and Reynolds number

4.2 Experimental Analysis

Over the past decade, the two algorithms mentioned earlier were broadly used in the research of μPIV. In this experiment, Heurisko software platform was used pre-processing the images. The post processing and resulted output were based on the codes developed in the MATLAB environment.

4.2.1 MATLAB platform

MATLAB is a programming language specialized in mathematical calculation and modeling. It is widely used in mechanical analysis, fluidics research, simulation of electrical device, and automation and control in industrial setup. Normally, MATLAB allows easy matrix manipulation, plotting of functions and data, implementation of algorithms, and interfacing with programs in other languages.

In this study, the MATLAB code was compared on two platforms, one is a dual-core notebook running Windows Vista 64-bit (2 GB RAM) which enabled multiple

threading in Matlab and the other one is a Windows XP 32-bit on a one core regular desktop with 2 GB RAM. Running MATLAB analysis is very memory intensive. The exact same code has being used on both platforms. As a result, 64-bit system does not get much better performance as compared to the above 32-bits system. The time for running a μPIV post process on microfluidic chamber I with inlet velocity is 802sec on Windows Vista 64-bit system versus 827 sec on Windows XP 32-bit system for calculations. As we can see, under current conditions, the upgrading of 32bits system to 64bits system does not accelerate the calculation process dramatically.

4.2.2 Data Analysis

In this chapter, the experimental result of flow velocity distribution in microchambers will be discussed. Two kinds of plots have been used to visualize the distribution of velocity. One is the planer which displays the entire velocity field distribution within certain chamber. This plot represents the flow velocity and direction at every single location within the chamber. The displacement of the location is standardized with respect to the origin located at the geometric center of the microchamber. The other types of plots are graphical curves that represent the velocity distribution along certain cross sections of the chamber. These plots are used to analyze and quantify the flow behavior at different flow rates at specific locations of the chambers. The velocity profiles along the x axis of shape I at different flow rate are shown in Figure 4.5.

4.3 Velocity distribution

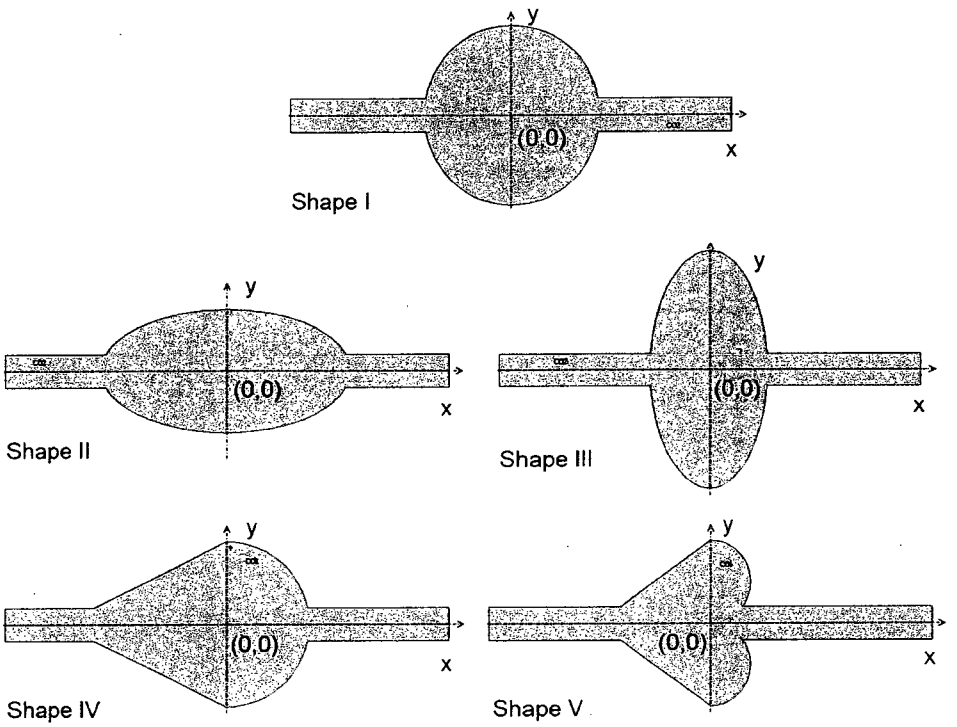

Figure 4. 1 Coordinates of shapes I, II, III, IV and V

4.3.1 Mean velocity

The entire velocity fields for shapes I to III at flow rate of 23.9e-3mm^3/s are shown in Figures 4.2 to 4.4.

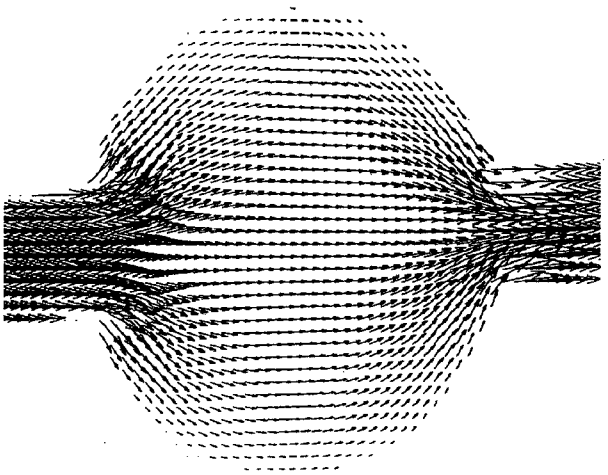

Figure 4. 2 Entire velocity distribution field of shape I at flow rate of 23.9e-3 mm^3/s (Re = 3.44e-1)

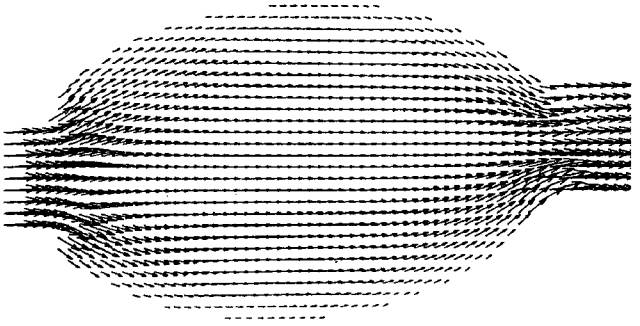

Figure 4. 3 Entire velocity distribution field of shape II at flow rate of 23.9e-3 mm^3/s (Re = 3.44e-1)

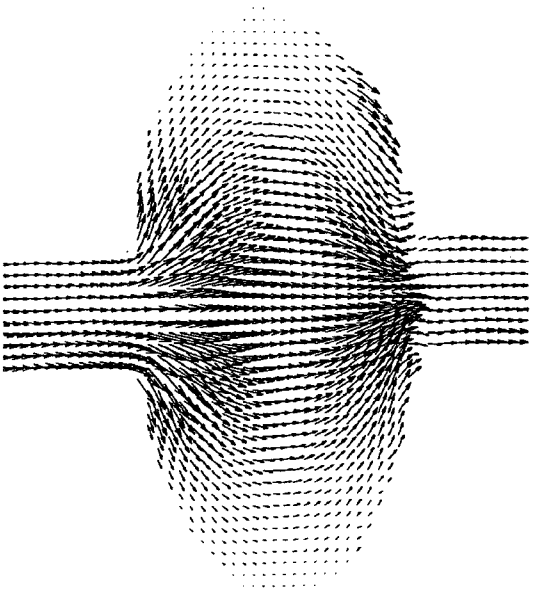

Figure 4. 4 Entire velocity distribution field of shape III at flow rate of 23.9e-3 mm^3/s (Re = 3.44e-1)

Due to the fundamental principle of the μPIV, the velocity at certain location is the mean velocity of an interrogation window. From the entire velocity distribution field of chamber I, it can be see that, except the inlet and outlet region, the rest of the chamber contains a homogeneous flow distribution along the axis of the chamber. As it is not possible to ensure the particle flow along the mid streamline, the mid streamline velocity is estimated with particles that are closer to the mid streamline. As these particles diverge or converge rapidly at the entry and exit, it increases the uncertainty in estimating centerline velocity. In the more stabilized region, which is close to the geometric centre of the chamber, the particles do not undergo large diversion and they represent the mid streamline being close to it. From Figure 4.5, it can be seen in Shape I that the maximum value of the inlet region is 8.66 mm/s, the outlet region is 8.80 mm/s

and the mid section is 2.65mm/s with the channel flow rate of $23.9\times10^{-3}mm^3/s$. The maximum value of the inlet region is 5.88mm/s, the outlet region is 5.60mm/s and the mid section is 1.70mm/s with the channel flow rate of $14.3\times10^{-3}mm^3/s$. The maximum value of the inlet region is 1.71 mm/s, the outlet region is 1.93mm/s and the mid section is 0.46mm/s with the channel flow rate of $4.78\times10^{-3}mm^3/s$. Unexpectedly, under high flow velocity, there was sudden increase in velocity nearby the inlet and outlet region of the chamber. These velocity peaks can be explained by the fundamental Laminar flow theory. Since micro-particles had been introduced into the testing fluid for tracking the flow, the characteristics of the fluid might be different from homogenous fluid of deionized water. Normally, this disadvantage of introducing particles can be corrected by reducing the size of the particle as introduced in Chapter 2. However, the smaller the size of the particle is used of higher magnification lens for μPIV system. Since μPIV is a detection of whole field flow distribution, the whole geometric structure of chamber should be within one single image taken by CCD. Therefore, the magnification of the lens is restricted by the size of the chamber which is 600μm in length. In this case, the size of the particles cannot be reduced accordingly.

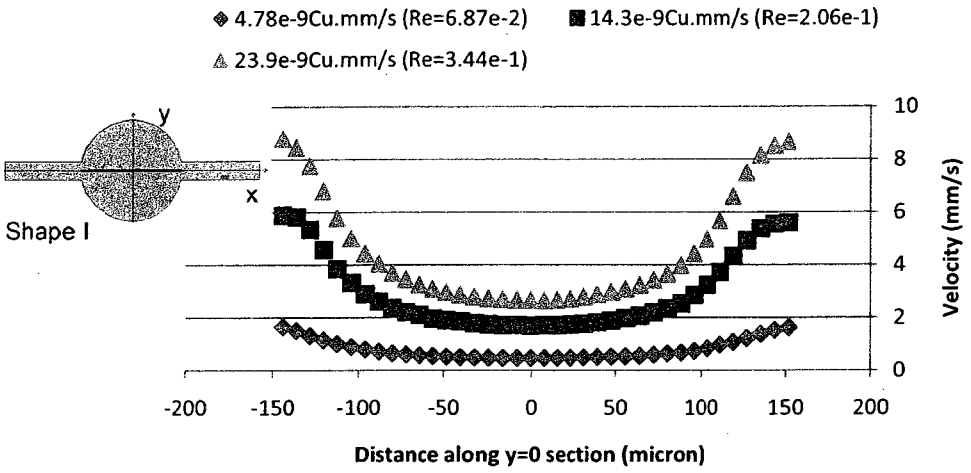

Figure 4. 1 Shape I Velocity variation along y=0μm section for flow rates of 4.78e-3mm^3/s (Re=6.87e-2), 14.3e-3mm^3/s (Re=2.06e-1) and 23.9e-3mm^3/s (Re=3.44e-1)

4.3.2 Comparison of velocity distribution in shape I, II and III

Comparing the entire velocity distribution field for shape I, shape II and shape III, the flow distribution in shape II is more homogeneous than flow distribution in shape I and shape III. Shape III with a much higher width to length ratio showed a peripheral region flow velocity close to zero, which means that these regions can be considered as dead zone. Figure 4.6 represents the comparison of flow distribution along the axis of the channel for the three shapes with the same flow rate of 23.9e-3mm^3/s. Under ordinary conditions, the peak velocity at the centre of the horizontal cross sections should be inversely proportional to the width of the chamber, where in this case it should be in the ascending order of III to I to II.

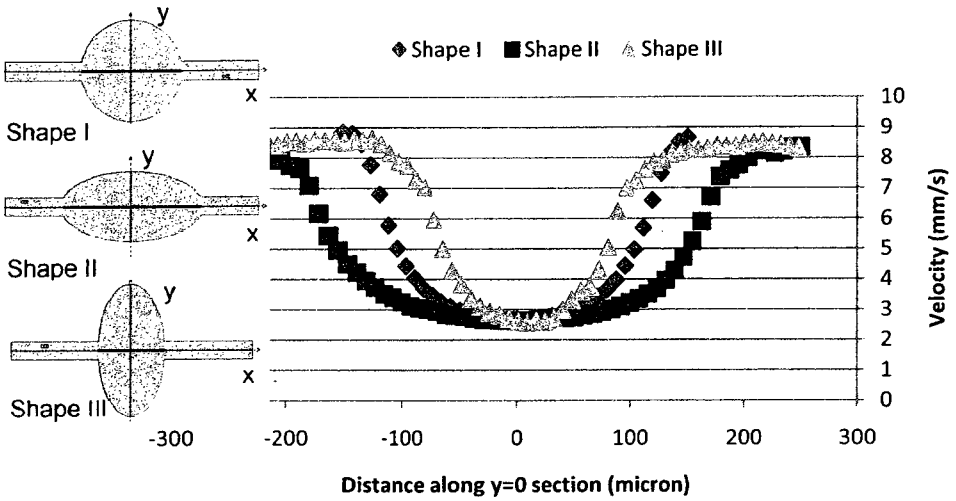

Figure 4. 2 Comparison of flow distribution along y=0μm section at flow rate of 23.9e-3mm^3/s (Re = 3.44e-1) for shapes I, II and III

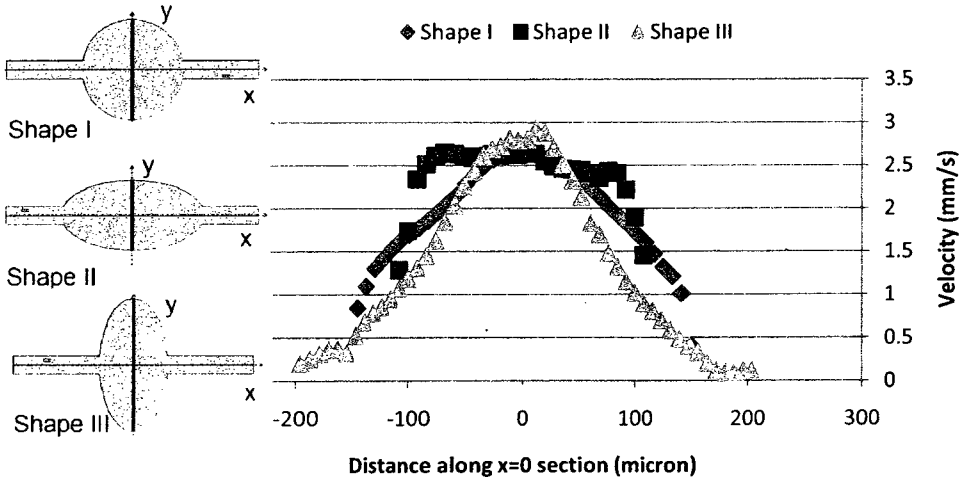

Figure 4. 3 Comparison of flow distribution along x=0μm section at flow rate of 23.9e-3mm^3/s (Re = 3.44e-1) for shapes I, II and III

Figure 4.7 shows the comparison between flow velocity distribution within shape I, II, and III along the mid cross section. The general pattern of the flow velocity distribution among three graphs are similar, given that the descending and ascending curve having a similar slope. Since shape II has a longer length with a smaller curvature along the chamber wall, therefore the velocity decreases more abruptly than the shape III which has a more gradual decrease in the velocity towards the wall.

4.3.3 Comparison of flow distribution in shape IV and shape V

The entire velocity fields for shape IV and shape V at flow rate of 23.9e-3 mm3/s are shown in Figures 4.8 and 4.9, respectively. As the figures show, shape V is more susceptible of forming a dead zone within the curved outlet region compared to shape IV, which does not contain such a low velocity part which may form a dead zone in the chamber.

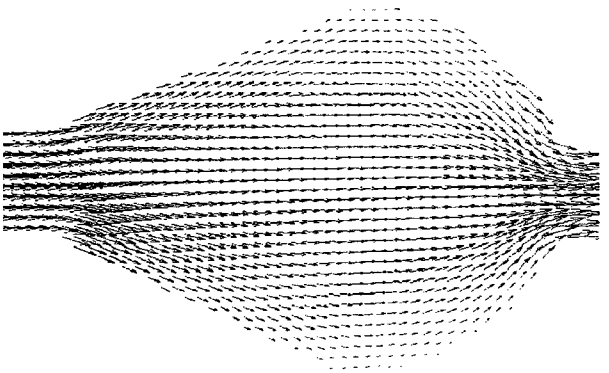

Figure 4. 4 Entire velocity distribution field of shape IV at flow rate of 23.9e-3 mm^3/s (Re = 3.44e-1).

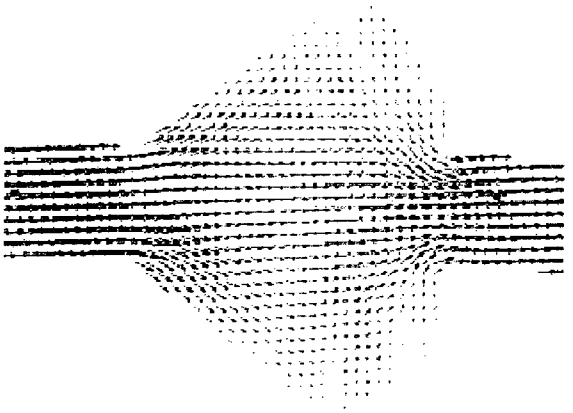

Figure 4. 5 Entire velocity distribution field of shape V at flow rate of 23.9e-3 mm^3/s (Re = 3.44e-1)

Figure 4.10 shows the comparison of the mid section, which locate half length of chamber size along x axis, flow velocity distribution for shape I, IV and shape V for the same channel flow rate of 23.9e-9mm^3/s. The velocity profile for shape I is also plotted as a reference. As shown in the plot, shape V has a much shaper peak which means that the velocity around the peripheral region decrease much faster comparing to shape IV which shows a very broad peak. This dramatic decrease is due to the recirculation formed within the peripheral region of shape V which establishes dead flow zones. Furthermore, the maximum peak velocity in shape V is higher than the maximum peak velocity in shape IV, because the low velocity recirculation zones narrow down the high velocity zone of the chamber causing the flow to accelerate in the central region of the chamber. The area under each graph, which represents the total flow rate, is the same within different section of variety of chambers, since the flow rate is the same.

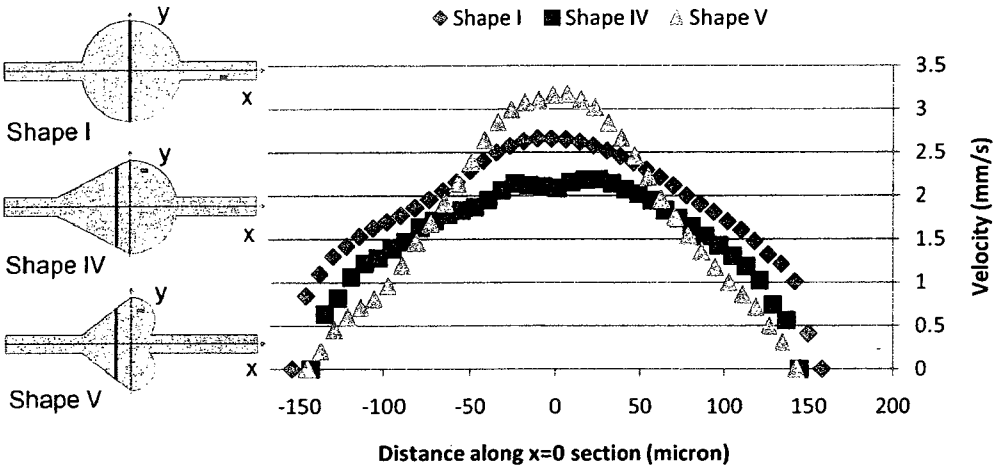

Figure 4. 6 Comparison of flow distribution at flow rate of 23.9e-3 mm^3/s (Re = 3.44e-1) for shapes I along x=0, shape IV along x= -60μm and shape V along x=-90μm

Figure 4.11 shows the comparison of flow velocity distribution along the x axis for shapes I, IV and V for the same channel flow rate of 23.9e-9 mm^3/s. The descending region and ascending region of the curve is not symmetric in both shape IV and V due to the asymmetric shape of the inlet and outlet region of the chambers. Compared to shape I which is the circular shaped chamber, shape IV which contains a semicircular shaped outlet region gives almost exactly the same flow velocity distribution in the downstream region. Shape V, which has a straight inlet opening with an angle of 60° gives similar velocity distribution to shape IV rather than shape I, which have an inlet opening angle of 53.13°. The descending region of shape V is more gradual which leads to the conclusion that smaller the inlet opening angle, slower the fluid velocity. Since the outlet region of shape V is not at the top of the geometric shape of the chamber, recirculation that formed adjacent to outlet region influence the flow around mid streamline leading to the maximum peak velocity at the midpoint actual is higher than the expected. As shown in

the figure, the lowest velocity is not at the geometric centre of shape V where the width of the chamber reaches maximum, but rather more upstream of the chamber.

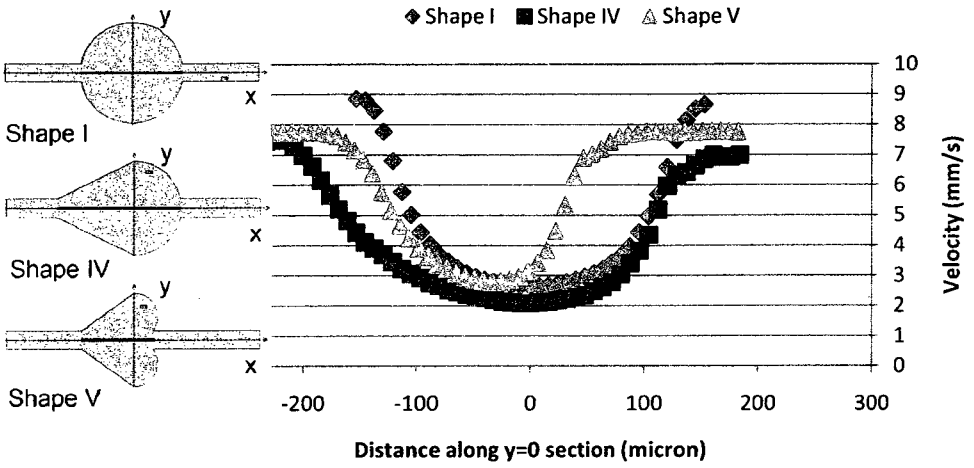

Figure 4. 7 Comparison of flow distribution at flow rate of 23.9e-3 mm^3/s (Re = 3.44e-1) for shapes I, IV and V along y=0μm section

4.4 Summary

In conclusion, μPIV method is able to visualize and measure the entire flow velocity field simultaneously. As shown with three different initial velocities, μPIV can be used to detect flow velocity within a very broad range with an acceptable detection limits. The flow velocity profile observed within certain cross section shows a more or less smooth curve which means that the flow became steady during the measurement. Furthermore, all of the distribution curves observed by μPIV displayed general trend as expected which should be a parabolic profile for pressure driven flow. The width to

length ratio of the chamber influences the mixing effect of the fluid within the chamber. If the ratio is high, dead zone might be formed in the region far away from the axis of the channel. If the ratio is low, such as in the case of the channel, the difference between adjacent streamline is small. It is possible to obtain recirculating flow at higher flow rate. Overall, the localized μPIV method was successful in estimating flow velocities.

Chapter 5

Modeling and verification of flows in microchambers

5.1 introduction

This chapter focuses on modeling microchambers and the comparison of the simulation result with the experimental results. Physical experimental results' feedback on whether these microfluidic chip designs work is a time-consuming process of prototype fabrication and testing. If the design does not work, the reason is difficult to be determined. The size of the devices, which is within microns scale, makes it nearly impossible to analyze them, and without quantitative information engineers must rely on instincts and multiple trials to optimize the design. For this reason, simulation software can be used to inspect and amend the designs. Simulation is an important tool for the analysis of microfluidic chip, which is critical not only for the manufacturing, but also in the operations. Under micron scale, the typical flows are characterized by low Reynolds numbers. Turbulence is hardly observed. Diffusion is more critical in the mixing phenomena [54]. Microfluidic system typically involves multiple physical processes that

are associated with each other. As of microfluidic system, it includes actuation, pumping, fluid and mobile parts.

In the last decade, the computational fluid dynamic (CFD) methods are well described in many papers and applied routinely in scientific applications. The CFD can offer multi-physics simulation, including coupled solutions of fluid flow, structures, electrostatics, AC / DC conduction, electro-magnetic, free surface flows with surface tension, and magneto-hydrodynamics, etc.

5.2 Popular commercial CFD software

There are various commercially available CFD software which could be used in microfluidic studies. These software include COMSOL [55], Fluent [56], CFX [57], Flow-3D, Phoenics [58], and Star-CD [59].

FLUENT is a commercially available popular CFD tools, which has been used in multiple industrial circles including flow, dynamics, heat transfer and chemical reaction. It contains a large number of physical models, advanced numerical techniques, preprocessing and post processing technologies, which are applicable to the automobile designs, petroleum and natural gas, machine turbo design, aviation and aerospace [56]. The Fluent software is part of CFD group software of ANSYS. It has high quality in terms of computational speed, stability and precision which gives the best combination for FLUENT software to adopt in different discrete forms and numerical techniques. Especially for various complicated physical phenomenon in a variety of flow field. The Gambit, which allows the user to control the mesh through the use of sizing functions

and boundary layer meshing, builds the geometric form and generates grid which is then solved in FLUENT [56].

CFX was initially developed by AEA Company in the United Kingdom. It is used to simulate fluid, conduction of heat, multiphase flow, chemical reaction, and combustion-gas stream. The advantage of CFX is its better ability to solve cases with complicated geometry but simple physical phenomenon [57]. CFX which solves solution through Finite Element Method (FEM) and Structured Grid Method specifically contains automation time step and simple algorithmic algebra grid. It can effectively and accurately express the complicated geometric form. Each grid allows shifting and deformation. The dynamic grid function further allows every grid to be able to slide or rotate compared to other part of the mesh [57]. CFX includes various turbulent models [57], which are K-Epsilon model, low Reynolds number K-Epsilon model, RNG K-Epsilon model, algebra Reynolds strain model, and differential Reynolds strain model etc. The CFX-TASC can process incompressible fluid, sub-stream. Turbulent models such as K-Epsilon model, double layers of model, conduction of heat to surface radiation, the Gibb's radiation model including convection of heat transfer, solid heat transfer, surface and porous medium heat transfer [57].

Compared to FLUENT, CFX which is a structured grid method has a higher convergence rate. But FLUENT is based on unstructured solving method, and therefore can improve calculation speed by distributed computing. FLUENT supports all Finite Volume Method, Finite Difference Method, as well as FEM for problem solving where as CFX only supports FEM [56; 57].

In 2003, ANSYS acquired AEA Company and CFX's trademark. Soon after, ANSYS also acquired FLUENT Company. Today FLUENT and CFX are both components of ANSYS.

PHOENICS is developed by CHAM Ltd. from United Kingdom. CFD simulation software solves heat, flow, reaction and combustion-gas streams. Phoenics have 21 built-in turbulent model, 8 multiphase flow models and over 10 different schemes that can be suitable for flows with various Reynolds numbers. The PHOENICS provides the function and interface to modify or add new models by clients [58].

STAR-CD is software for simulation of flow in Arbitrary Region. STAR-CD is originated from CD-adapco Ltd. It based on FVM. Its grid generation uses unstructurized grid cell, which can be a hexahedron, a tetrahedron, pyramidal cone or six kinds of forms of polyhedral. STAR-CD has interfaces convenient with CAD, CAE software, such as ANSYS, IDEAS, NASTRAN, PATRAN, ICEMCFD and GRIDGEN etc [59].

5.3 COMSOL

COMSOL based on FEM was developed from MATLAB toolbox. It includes several modules which include AC/DC Module, Acoustics Module, Chemical Engineering Module, Earth Science Module, Heat Transfer Module, MEMS Module, RF Module, and Structural Mechanics Module. For most of the other multi-physical modeling, COMSOL uses direct-coupling instead of indirect-coupling [55]. Moreover, user-defined expression is easily controlled than other CFD software where the expression is not modifiable or addible by the users under different situations. Since COMSOL was

developed by MATLAB toolbox, it is able to output series of MATLAB commands, which can be performed as a file with extension 'm' and script by MATLAB. Each action performed in COMSOL can also be programmed in MATLAB as a file with extension 'm'. By using script of COMSOL, it is very easy to develop modules specialized for certain mathematical model [55].

However, COMSOL has a poor function creation for geometric modeling, especially for mending geometric model imported from other CAD software. It causes COMSOL to occupy more memory than using direct approach to solve the special model, since it pushes data into memory directly. Furthermore, after various physical fields have been occupied, the required data bandwidth increases dramatically [55].

FEM is the most commonly used calculation method in both academia and industry. It was first used for solving the problem in structural mechanics. Nowadays, it has been broadly used in the field of structural mechanics, fluidics, and heat conduction etc for analysis and simulation. FEM first separate the region under calculation into many non-overlapping blocks which called elements. These elements are connected with each other by nodes. The size of the elements will influence the difference between simulation results and real situations. The smaller the elements, the high precision will be achieved. In an element, the differential equation or algebraic equations can be used to calculate the physical variables. Finally, a combined equation considering all the individual elemental equations along with appropriate boundary conditions can be solved.

5.3.1 Optimal mathematical model in COMSOL.

The memory of computer required for simulations is different. These differences depend on the number of nodes of geometric grid, the classes of form function, for

example, second order Lagrange function. The size of the computing grid is depended on the classes of form function and numbers of geometric grid. Furthermore, it also depends on the numbers of independent variables and implicit variables. The looseness of sparse matrix of the model also influences the amount of the calculations. The looseness of sparse matrix of the models depends primarily on the degree of freedom on coupling between different equations [60]. Also, the geometric dimensions of the object and the shape of the grid can influence the looseness of the model. For instance, an objective with a high degree of freedom and thin or flat surface, like microchambers used in microfluidics, will have a looser matrix of the whole model than a solid big object.

5.3.2 Calculation methods involved in simulation

5.3.2.1 Basic assumption

All the calculations are based on the following assumptions:

1) The viscosity coefficient, diffusion coefficient, and density for fluid are all constant.

2) The fluid is incompressible.

3) The effects of gravity, magnetic force, and temperature are ignored.

5.3.2.2 Simultaneous system of equations for physical model

Equation of continuity

$$\frac{\partial u}{\partial x} + \frac{\partial v}{\partial y} + \frac{\partial w}{\partial z} = 0 \tag{5.1}$$

Equation of momentum along X-axis

$$\rho\left(\frac{\partial u}{\partial t}+u\frac{\partial u}{\partial x}+v\frac{\partial u}{\partial y}+w\frac{\partial u}{\partial z}\right)=-\frac{\partial p}{\partial x}+\mu\left(\frac{\partial^2 u}{\partial x^2}+\frac{\partial^2 u}{\partial y^2}+\frac{\partial^2 u}{\partial z^2}\right) \quad (5.2)$$

Equation of momentum along Y-axis

$$\rho\left(\frac{\partial v}{\partial t}+u\frac{\partial v}{\partial x}+v\frac{\partial v}{\partial y}+w\frac{\partial v}{\partial z}\right)=-\frac{\partial p}{\partial y}+\mu\left(\frac{\partial^2 v}{\partial x^2}+\frac{\partial^2 v}{\partial y^2}+\frac{\partial^2 v}{\partial z^2}\right) \quad (5.3)$$

Equation of momentum along Z-axis

$$\rho\left(\frac{\partial w}{\partial t}+u\frac{\partial w}{\partial x}+v\frac{\partial w}{\partial y}+w\frac{\partial w}{\partial z}\right)=-\frac{\partial p}{\partial z}+\mu\left(\frac{\partial^2 w}{\partial x^2}+\frac{\partial^2 w}{\partial y^2}+\frac{\partial^2 w}{\partial z^2}\right) \quad (5.4)$$

Here, ρ represents the density, t is time, u, v, and w are the velocity components in x-, y- and z-directions, respectively. P represents the pressure, and μ is the dynamic viscosity.

5.3.2.3 Definition for general expression

When using COMSOL to solve the partial differential equations, the mathematical equations must be transformed into standard general expressions defined in COMSOL as nonlinear equations,

$$d_a\frac{\partial u}{\partial t}+\nabla\cdot\Gamma=F \quad (5.5)$$

Here, $d_a\frac{\partial u}{\partial t}$ represents the time term, d_a is the coefficient for time term; ∇ is the gradient operator; Γ is the flux term; and F is the source term [55].

Using equation 5.1 to 5.4, the following general expression can be generated:

Equation of continuity

$$\Gamma = -\begin{bmatrix}0\\0\\0\end{bmatrix}, \qquad F = -\left[\frac{\partial u}{\partial x} + \frac{\partial v}{\partial y} + \frac{\partial w}{\partial z}\right] \tag{5.6}$$

Equation of momentum on X-axis

$$\Gamma = -\begin{bmatrix} 2\mu\frac{\partial u}{\partial x} \\ \mu\left(\frac{\partial u}{\partial y} + \frac{\partial v}{\partial x}\right) \\ \mu\left(\frac{\partial u}{\partial z} + \frac{\partial w}{\partial x}\right) \end{bmatrix},$$

$$F = -\left[\frac{\partial p}{\partial x} + \rho\left(u\frac{\partial u}{\partial x} + v\frac{\partial u}{\partial y} + w\frac{\partial u}{\partial z}\right)\right],$$

$$d_a = [\rho] \tag{5.7}$$

Equation of momentum on Y-axis

$$\Gamma = -\begin{bmatrix} \mu\left(\frac{\partial v}{\partial x} + \frac{\partial u}{\partial y}\right) \\ 2\mu\frac{\partial v}{\partial y} \\ \mu\left(\frac{\partial v}{\partial z} + \frac{\partial w}{\partial y}\right) \end{bmatrix},$$

$$F = -\left[\frac{\partial p}{\partial y} + \rho\left(u\frac{\partial v}{\partial x} + v\frac{\partial v}{\partial y} + w\frac{\partial v}{\partial z}\right)\right],$$

$$d_a = [\rho] \tag{5.8}$$

Equation of momentum on Z-axis

$$\Gamma = -\begin{bmatrix} \mu\left(\frac{\partial w}{\partial x} + \frac{\partial u}{\partial z}\right) \\ \mu\left(\frac{\partial w}{\partial y} + \frac{\partial v}{\partial z}\right) \\ 2\mu\frac{\partial w}{\partial z} \end{bmatrix},$$

$$F = -\left[\frac{\partial p}{\partial z} + \rho\left(u\frac{\partial w}{\partial x} + v\frac{\partial w}{\partial y} + w\frac{\partial w}{\partial z}\right)\right],$$

$$d_a = [\rho] \tag{5.9}$$

5.3.2.4 Boundary conditions

The inlet velocities (i.e. the velocities at inlet of the microchamber) same as that of the experiments are considered for the simulations. That is:

$$u = u_{in},\ v = v_{in},\ w = w_{in} \tag{5.10}$$

Here, the subscript 'in' represents the inlet condition. The velocity at the exit was selected as a fully developed flow.

$$\frac{\partial u}{\partial s} = \frac{\partial v}{\partial s} = \frac{\partial w}{\partial s} = 0 \tag{5.11}$$

No-slip condition was selected for wall. At wall,

$$u = v = w = 0 \tag{5.12}$$

The gauge pressure at outlet was set to zero. The outlet is exposed to atmosphere.

The initial condition of the velocity is as following:

$$u = V_{init} \quad \text{and} \quad P_{out} = 0 \tag{5.13}$$

5.3.2.5 Calculations of parameters

Many of the parameters necessary to simulate these microchambers have been acquired through design values or measurement, including the size, inlet velocity and outlet press, diffusion coefficients, and viscosities. These parameters are presented in Table 5.1.

Name	Value	Unit
Liquid density	1.00E+03	kg/m3
Dynamic viscosity	1.00E-03	N s/m2
Volume force X-dir	0	N
Volume force Y-dir	0	N
Outlet pressure	0	Pa
Channel depth	2.00E-05	m
Mean free path	3.10E-09	m

Table 5. 1 Structural parameters of simulation

The viscosity is set to the viscosity of water at the room temperature. Since the majority of the fluid is water, the diffusion coefficient is within the scale of $10^{-9}m^2/s$, the Reynolds number is less than 1. The flow rates of the fluid as mentioned before were $4.78\times10^{-3}mm^3/s$, $14.3\times10^{-3}mm^3/s$ and $23.9\times10^{-3}mm^3/s$.

5.4 Comparison between simulation results and experimental results

5.4.1 Comparison for Shape I at the flow rate of 14.3e-3mm^3/s (Re=2.06e-1)

The comparison between the experimental and simulation results for shape I at different cross-sections is shown in Figure 5.1 to 5.4. The location of the section corresponds to shows on top left corner of these figures. The Figure 5.1 shows the comparison of simulation and experiments along inlet cross section at x=-150μm. The Figure 5.2 shows the comparison of simulation and experiments along the middle cross section at x=0. The Figure 5.3 shows the comparison of simulation and experiments along outlet cross section at x=150μm. The Figure 5.4 shows the comparison of simulation and experimental result along channel axis cross section at y=o. These experimental results based on 'detect windows', which means that there are fewer data points obtained in the experimental analysis than simulation results. Except for the entrance region, the simulation results agreed well with the experimental results. At the inlet section, the magnitude of the experimental velocity is lower than the simulated values which are likely due to the reason that in the experimental study, there were some bad data points in the inlet section that were eliminated from the experiments and hence the averaged values are slightly underestimated.

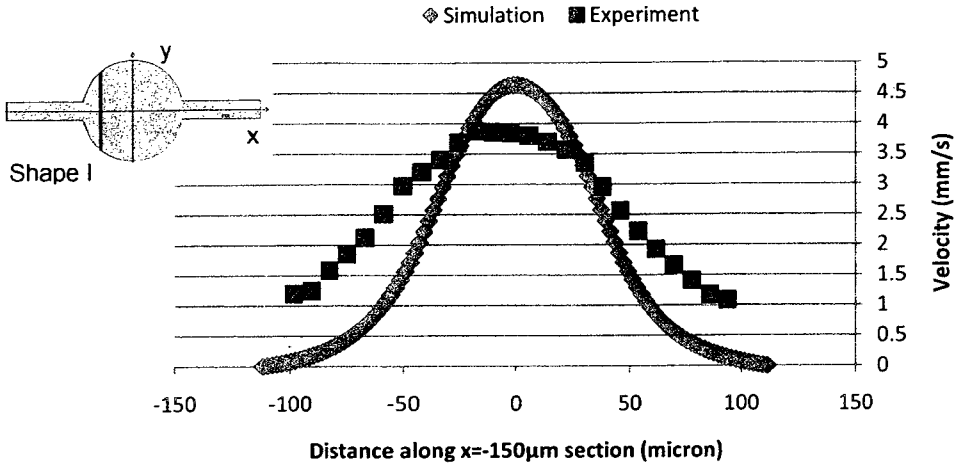

Figure 5. 1 Comparison of prediction and experimental velocity distribution along x= -150μm section at flow rate of 14.3e-3mm^3/s (Re=2.06e-1) for shape I

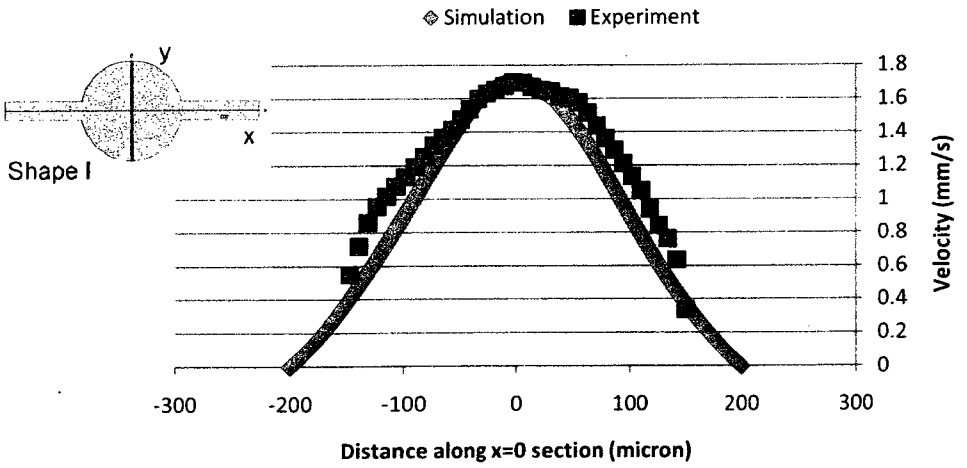

Figure 5. 2 Comparison of prediction and experimental velocity distribution along x=0μm section at flow rate of 14.3e-3mm^3/s (Re = 2.06e-1) for shape I

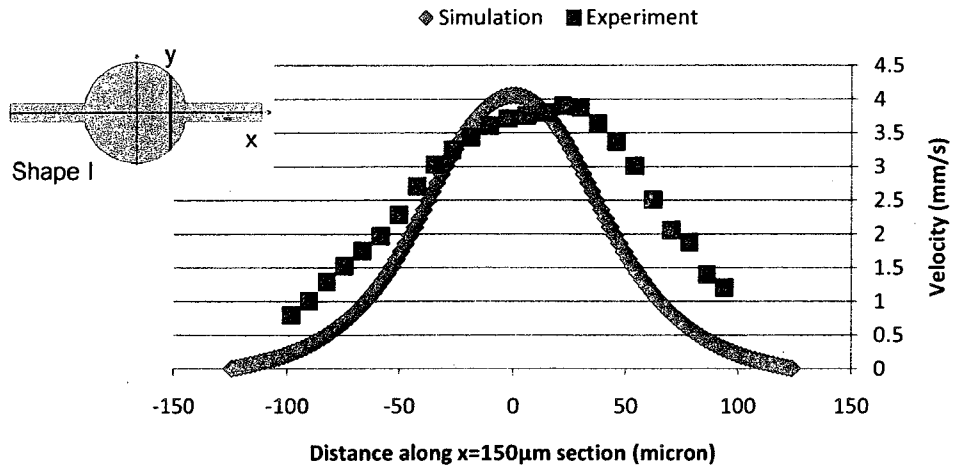

Figure 5. 3 Comparison of prediction and experimental velocity distribution along x=150µm section at flow rate of 14.3e-3mm^3/s (Re = 2.06e-1) for shape I

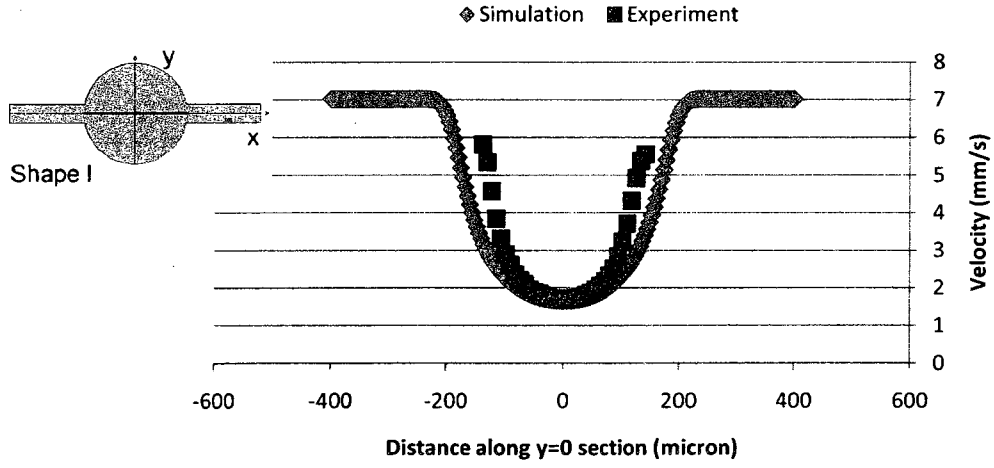

Figure 5. 4 Comparison of prediction and experimental velocity distribution along y=0µm section at flow rate of 14.3e-3mm^3/s (Re = 2.06e-1) for shape I

Within the chamber, the cross section perpendicular to the axis gives a parabolic shape. In general, the width of the chamber should be inversely proportional to the maximum low-peak velocity of the cross section. And, the average velocities along the cross section should be inversely proportional to size of chamber despite the flow rate of the inlet flow.

Where Figure 5.1 to 5.3 show the comparison of predicted velocities and experimental velocities along difference distance of x of shape I, and at flow rate of $14.3\times10^{-3}mm^3/s$. Figure 5.4 to Figure 5.6 show the same comparisons along x axis at three different flow rates. In Figure 5.7 to Figure 5.8, predicted velocities and experimental velocities along y axis are compared at different flow rates. The simulation results agreed well with the experimental results at the two lower flow rates. At the lowest flow rate, the experimental results are lower in magnitude than the simulation results. These differences might caused by the induction of particles into the fluid, which may not follow the same characteristics as the pure deionized water that was used for the calculation of the simulation results.

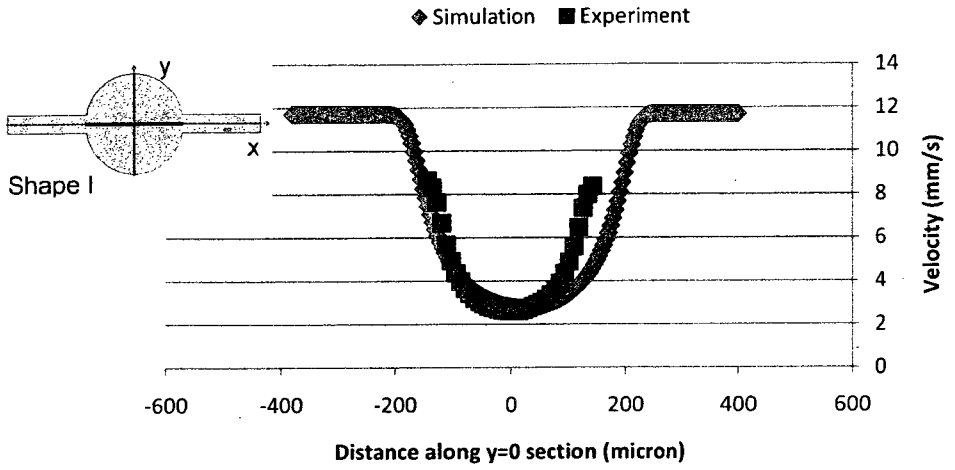

Figure 5. 5 Comparison of prediction and experimental velocity distribution along y=0μm section at flow rate of 23.9e-3mm^3/s (Re=3.44e-1) for shape I

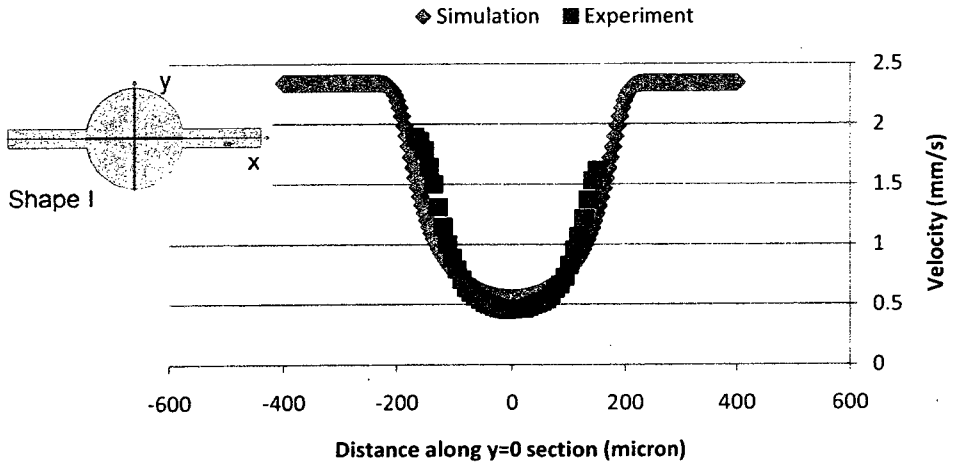

Figure 5. 6 Comparison of prediction and experimental velocity distribution along y=0μm section at flow rate of 4.78e-3mm^3/s (Re=6.87e-2) for shape I

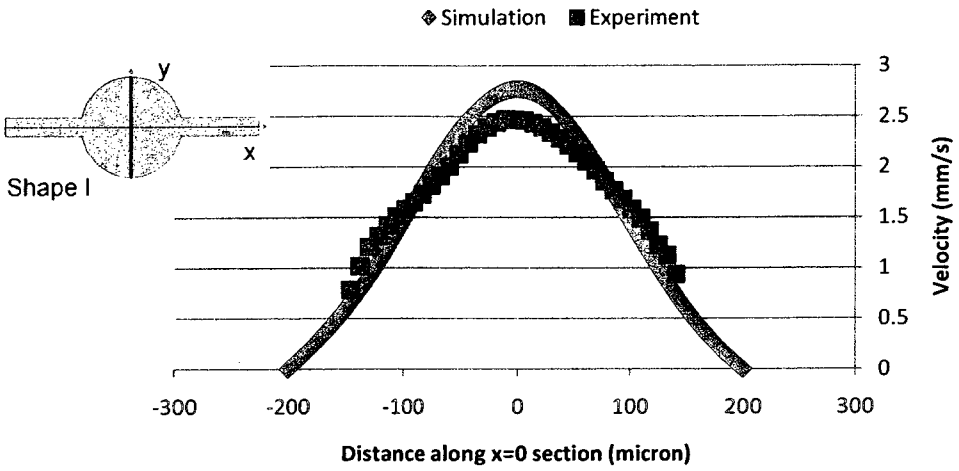

Figure 5. 7 Comparison of prediction and experimental velocity distribution along x=0μm section at flow rate of 23.9e-3mm^3/s (Re=3.44e-1) for shape I

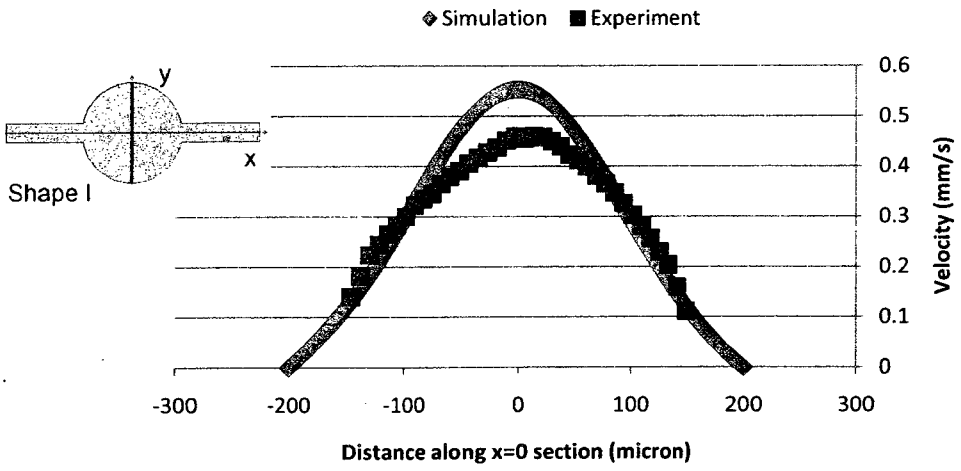

Figure 5. 8 Comparison of prediction and experimental velocity distribution along x=0μm section at flow rate of 4.78e-3mm^3/s (Re=6.87e-2) for shape I

5.4.2 The experimental uncertainty induced by apparatus and calculation algorithm

Figures 5.9 and 5.10 which shows the velocity distribution along the middle sections at x=0 for the Shape I and Figures 5.11 and 5.12 shows the velocity distribution along the axis section (y=0) of the Shape I under different flow rate. Higher the entrance flow rate, the lower the consistency of the measured velocity especially near the inlet and the outlet regions of the chamber. Because the PIV measurement relies on a interrogation window, within the outlet region, the changes in flow velocity increase dramatically, and therefore the variability of velocity within this interrogation window increases and hence the stability of the measurement decreases. Another possible reason is that around the outlet region, the particle contains velocity towards different directions with an uneven distribution. Furthermore, the detectable particles within the interrogation window, which appears twice in two adjacently pictures taken, decrease due to the high velocity. Therefore the weighing of each measured particle in PIV calculation results in a increase and the unevenly distributed particle movement will distort the velocity towards certain direction significantly. This effect decreases the detection range of experimental analysis under the region with high acceleration, and therefore increases the systemic error of the measurement and the precision of the measurement decrease as well. In Figure 5.10 the experimental results drop faster than simulated results due to experimental limitation on capturing high velocity gradient flows. This could be due to the less number of particles in the interrogation window adjacent to the wall. In general, each window should contain at least 3 particles in order to have a correct calculation. However, the bigger the size of the window, the larger the minimal detection area it is for the calculation. In this case, the velocity gradients increase dramatically. This effect is especially important when calculating the velocity along the

wall of the chamber since the closer it is to the wall, the steeper the gradients are. Furthermore, along the wall, particles "slide" over the wall because friction force and oriented Brownian movements which do not fulfill the assumption for the calculations used in the experimental setup. This region is very small but may influence the simulated velocity curve and may cause difference between experimental and simulation results in these regions. On the other hand, the tangent lines of the flow velocity and the tangent lines of the wall change along the outer most streamline, which makes the condition much more complicated in these regions. Since our experimental objective is mainly focused on the functional region, i.e. the central region, of the chamber, the complication associated with the peripheral region is not considered in the simulation model.

Another parameter that causes the mis-match between experimental and simulation results is the precision of the calculated magnification scale. Since the microfluidic system is very small, it requires a high optic magnification for the detection. Therefore, any small difference between the magnification marked on the lens and the actual magnification of the lens is amplified. Furthermore, under such a high magnification, the variance within the wavelength of the illumination light can also influence the actual magnification of the lens. On the other hand, the incident angle of the light is not exactly perpendicular to the entire FOV and therefore causing elongation of the optical path and lead to miscalculation of the magnification. Therefore, alternatively, the magnification scale of the experimental setup can be calculated by another method rather than using the marked magnification of the lens. It can be calculated from the number of pixels between two points and the actual distance between these two points. Unfortunately, this method is also not perfectly precise, as the wall of the chambers is not exactly perpendicular to the plane of the microfluidic chip, making it difficult to find the exact defined point in the image of μPIV.

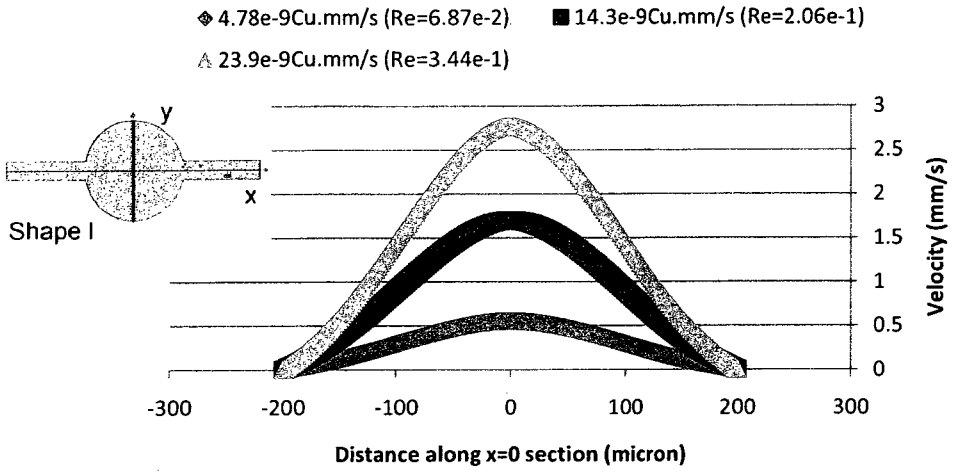

Figure 5. 9 Comparison of predicted velocity distribution along x=0μm section under different flow rates for shape I

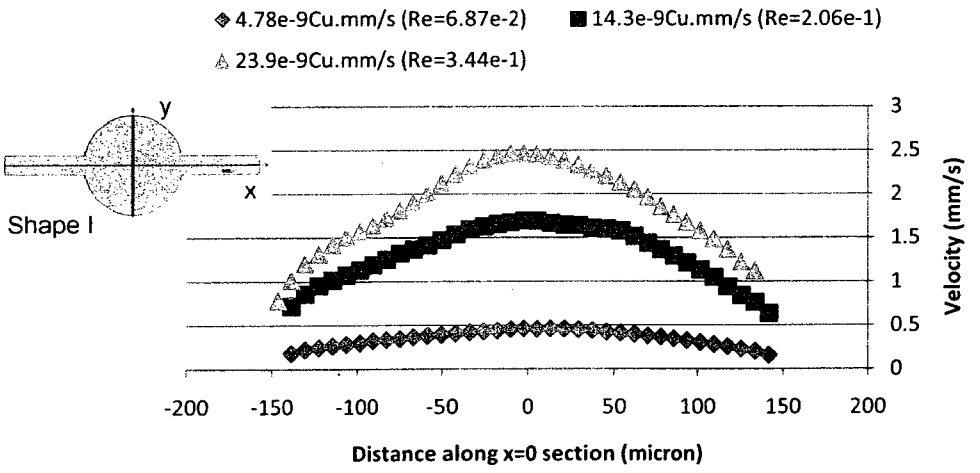

Figure 5. 10 Comparison of experimental velocity distribution along x=0μm section under different flow rates for shape I

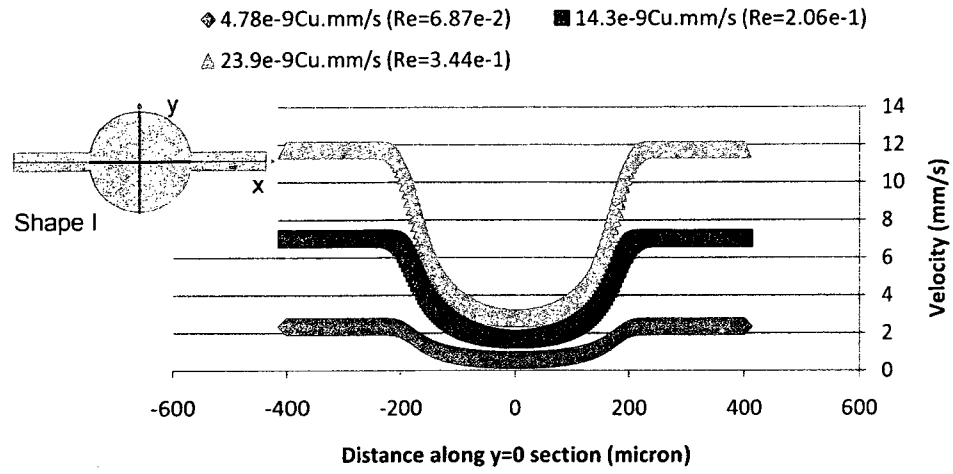

Figure 5. 11 Comparison of predicted velocity distribution along y=0μm section under different flow rates for shape I

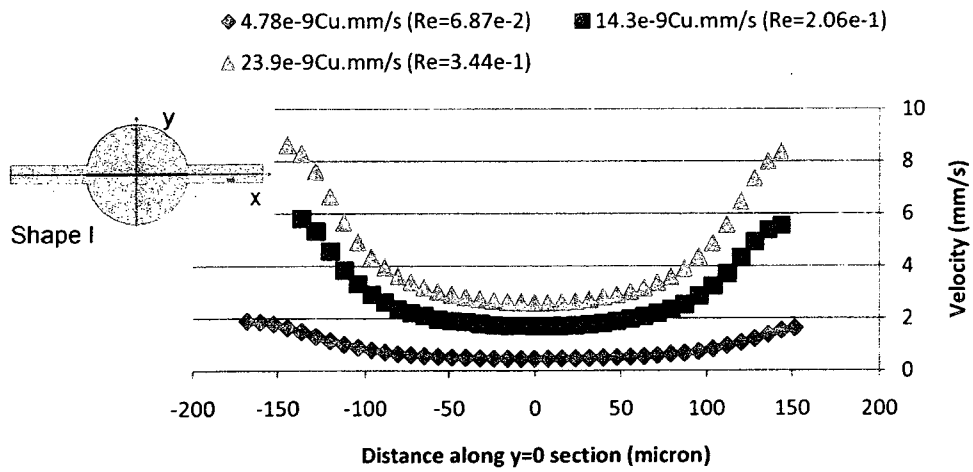

Figure 5. 12 Comparison of experimental velocity distribution along y=0μm section under different flow rates for shape I

As shown in Figures 5.9 to Figure 5.12, the shape of the velocity distribution curve is similar for different entrance flow rate. The differences between the velocities are proportional to the differences between the entrance flow rates. This phenomenon is well presented in Figure 5.12 which shows the velocity distribution along the axis. In the case of circular chamber, the distribution is symmetrical along the mid cross section and therefore the chamber has been chosen as the reference to demonstrate this verification study.

5.4.3 Effect of aspect ratio on flow velocity distribution

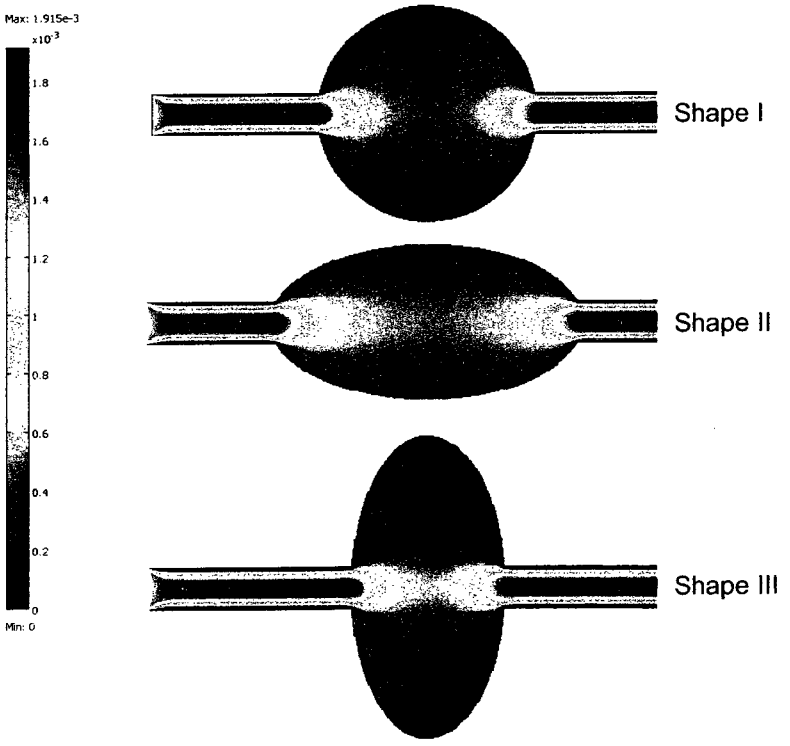

Figure 5. 13 Comparison of flow velocities surface plot at flow rate of 4.78e-3mm^3/s (Re=6.87e-2) for shapes I, II, III

Figure 5.13 shows the comparison of simulated velocity distribution for elliptical chamber with two foci along the channel axis (shape II) and elliptical chamber with two foci perpendicular to the channel axis (shape III) along with circular chamber (shape I). Red color represents region with high flow velocity and blue color represents region with low flow velocity. As indicated, the flow distribution at the inlet and outlet region is similar among all three shapes, but the distribution along the mid cross section and axis are different. Because in microfluidic system the flow is mainly laminar, two fluid layers are hardly mixed within a narrow straight channel and hence these chambers are required for mixing and reaction of two fluids. Since the longitudinal diameters of the chambers is different among these three shapes, the reaction efficiency depends on the ratio of the streamline length and the distance between inlet and outlet regions. Larger the length to width ratio of chamber, slower is the flow and longer is the residence time of the flow within the chamber.

Since the flow velocity is linearly related to the pressure of the flow, according to the Hagen–Poiseuille equation [61]:

$$\Delta P = \frac{8\mu LQ}{\pi r^4} = KLQ \tag{5.14}$$

Here L is the distance along the streamline, r is the radius of the chamber, Q is the volumetric flow rate, μ is the dynamic viscosity which is constant in this study, and K is the pressure descending index. K is related to the flare angle of the chamber. In this case, velocity and flow rate are constant within the channel. Therefore, as the flare angle increase, pressure decreases exponentially. Therefore the pressure drop between a certain point and inlet (or outlet) region is determined by only two parameters which is

the width of the chamber and the distance along the streamline from the inlet (or outlet) region of the chamber. Therefore, for all three shapes, the midpoint velocity which is directly related to the pressure at this point can be qualitatively determined by these parameters. Shape I has a total length of 400μm; shape II has a total length of 540μm; and shape III has a total length of 280μ m which gives 200μm, 270μm, and 140μm from the midpoint to the inlet opening of the chamber. The width of shape I, II, and III are 400μm, 280μm, and 540μm respectively. By using these geometrical factors, the aspect ratio of each chamber can be calculated. However, the flow distribution is not only associated with the aspect ratio, but also related to the characteristics of the flow. Therefore only estimated velocity at certain location can be obtained. As shown in Figure 5.15, shape III contains the highest midpoint flow velocity which is followed by shape II which is higher than shape I.

Figures 5.15 to 5.20 which give the velocity distribution of the flow along the mid cross sections (x=0) of all three chambers, the comparison between the experimental and simulation results for shape II and shape III is similar to what seen for shape I. Shape II has more deviation indicating that the velocity differences between particles and de-ionized water are the largest near the central part. Velocity distribution can be observed as non-parabolic. Shape II has the highest average velocity and shape III has the lowest average velocity. The characteristic homogenous velocity across the mid section (x=0) of shape II chamber detected in the experimental results is not a smooth curve (Figure 5.14). However, around the region very close to the chamber boundary, the flow behavior matches the simulation curve. The average velocity at certain cross section is dependent on the size of the sectional area. Here shape III has the largest cross section area which gives the lowest average velocity. Although the shape III has the highest slope of curve around the central region of the chamber, the peripheral

region of the chamber has virtually no flow velocity. Such a zone within a chamber is called dead zone which means the fluid within this zone have a longer residence time. This effect may cause retention or even precipitation of the reagent that could further block the flow circuits.

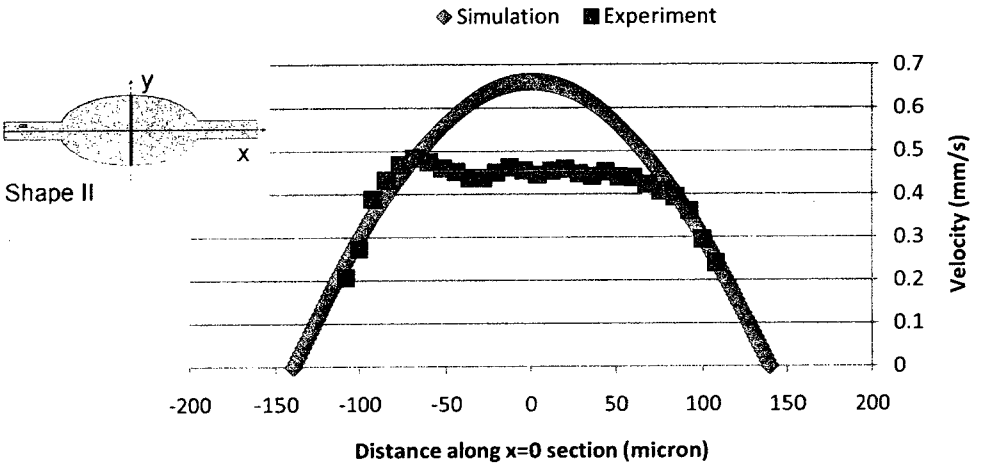

Figure 5. 14 Comparison of prediction and experimental velocity distribution along x=0μm section at flow rate of 4.78e-3mm^3/s (Re=6.87e-2) for shape II

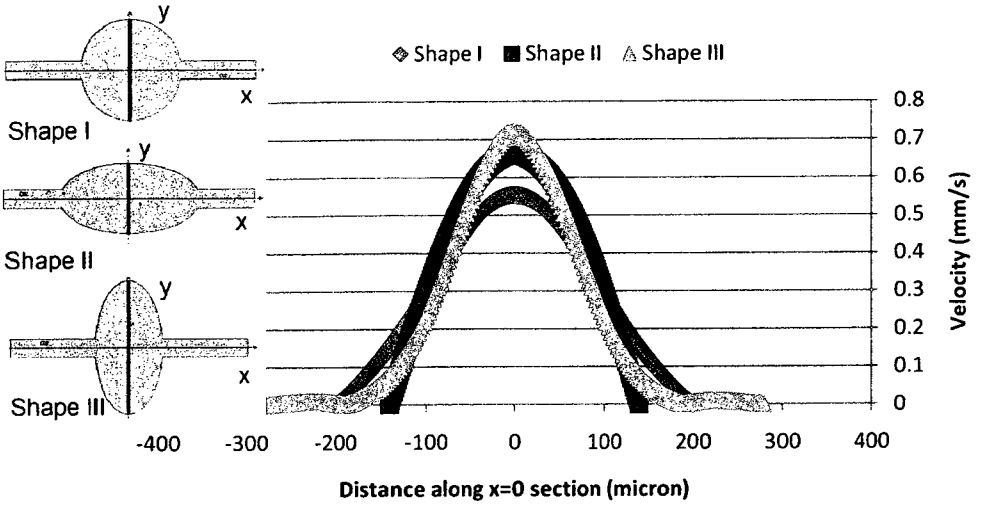

Figure 5. 15 Predicted velocity distributions along x=0μm section at flow rate of 4.78e-3mm^3/s (Re=6.87e-2) for shapes I, II and III

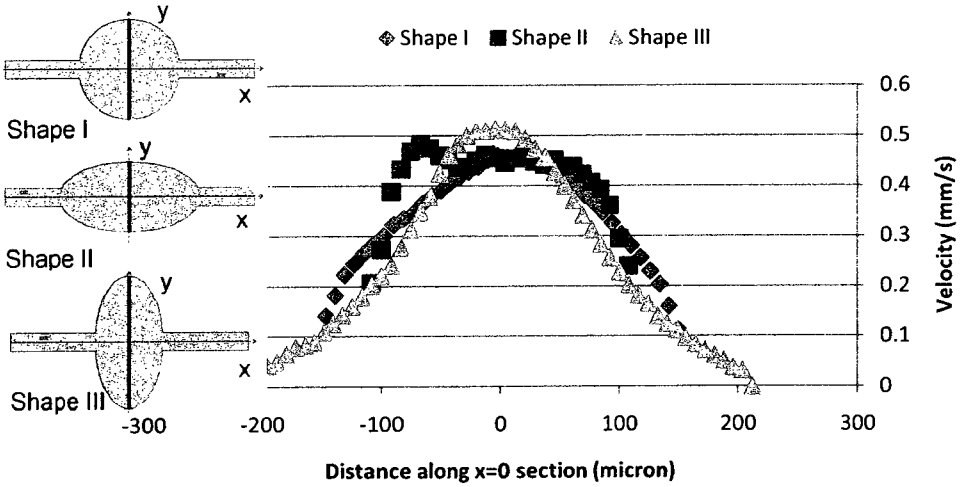

Figure 5. 16 Experimental velocity distributions along x=0μm section at flow rate of 4.78e-3mm^3/s (Re=6.87e-2) for shapes I, II and III

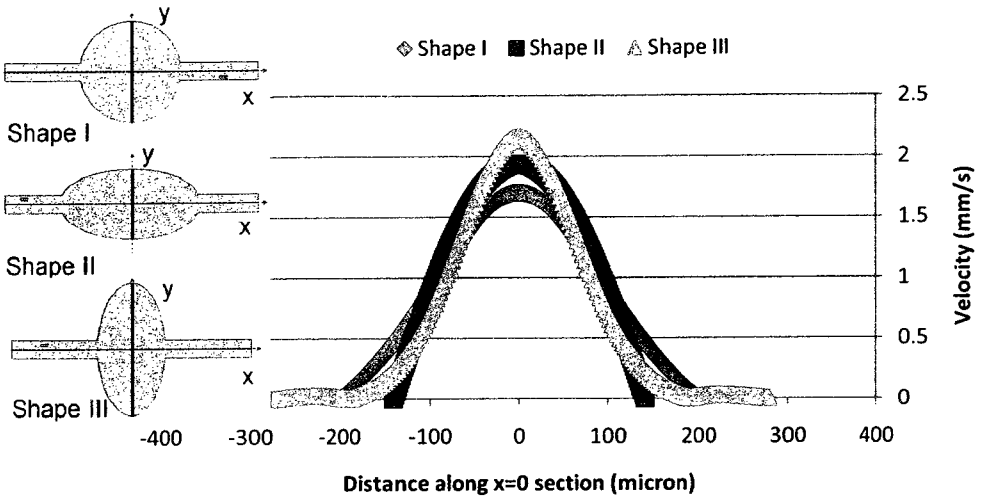

Figure 5. 17 Predicted velocity distributions along x=0μm section at flow rate of 14.3e-3mm^3/s (Re=2.06e-1) for shapes I, II and III

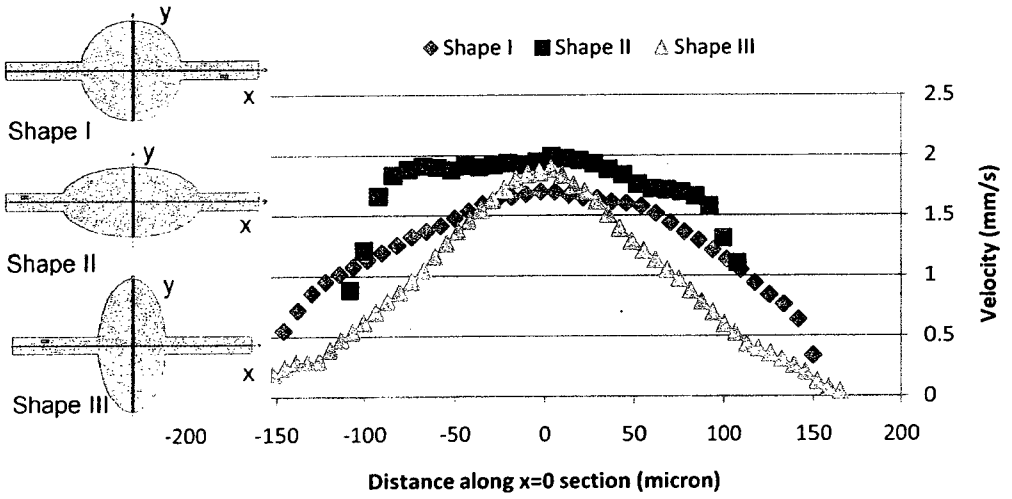

Figure 5. 18 Experimental velocity distributions along x=0μm section at flow rate of 14.3e-3mm^3/s (Re=2.06e-1) for shapes I, II and III

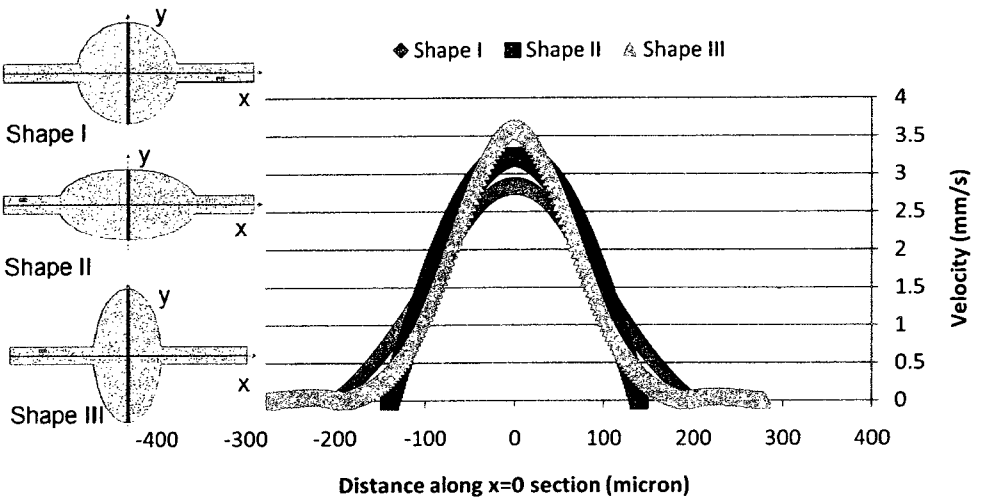

Figure 5. 19 Predicted velocity distributions along x=0μm section at flow rate of 23.9e-3mm^3/s (Re=3.44e-1) for shapes I, II and III

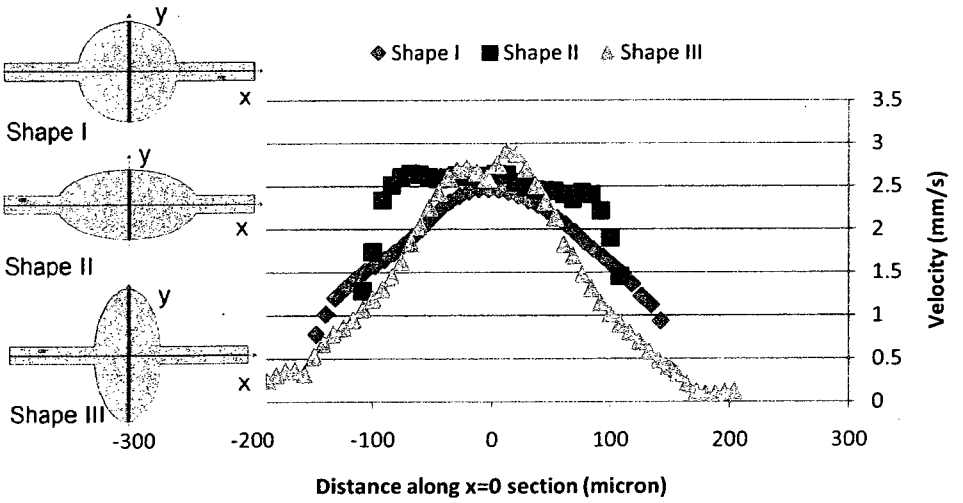

Figure 5. 20 Experimental velocity distributions along x=0μm section at flow rate of 23.9e-3mm^3/s (Re=3.44e-1) for shapes I, II and III

5.5 Asymmetric inlet and outlet chambers with corners.

Previous studies had shown that chambers with sharp angles, such as squares or triangles or diamond which gives larger corner angle, will give dead zones around the corner of the chambers [62]. In order to discover the more complicated flow behavior within chambers with corners and asymmetric inlet and outlet region, shape IV and shape V have been designed. As shown in Figure 5.21 Both of them contain straight walls along the inlet region and curved walls along the outlet region. The curved side of shape IV is a semicircle where the curved side of shape V is made of two smaller semicircles.

The zoomed outlet region of the shape V in simulation vector plot is shown in Figure 5.22. Within the curved region, the flow velocity is very low and the flow direction is reversed than the main stream flow which forms recirculation zone. In the experimental data, the flow velocity detected within this region is zero. Even in the simulation results, the recirculation is detected only with 50X magnification of velocity. Therefore we can conclude that, this region of the chamber increases the residence time dramatically and forms a dead zone. This zone has very little or no contribution to the reaction or mixing role of the chamber. Flow distribution as shown in Figure 5.23 for shape IV with the curved outlet region. No recirculation zone is formed in this case and the velocity near the wall is higher than the one in shape V. This velocity is even detected in the experimental μPIV measurements even with a lower detection power.

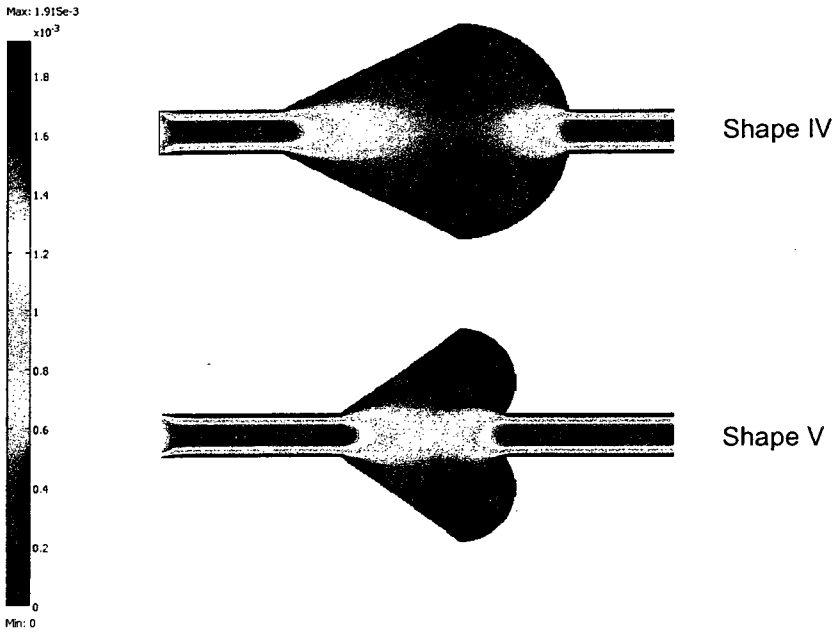

Figure 5. 21 Comparison of flow velocities surface plot at flow rate of 4.78e-3mm3/s (Re=6.87e-2) for shapes IV and V

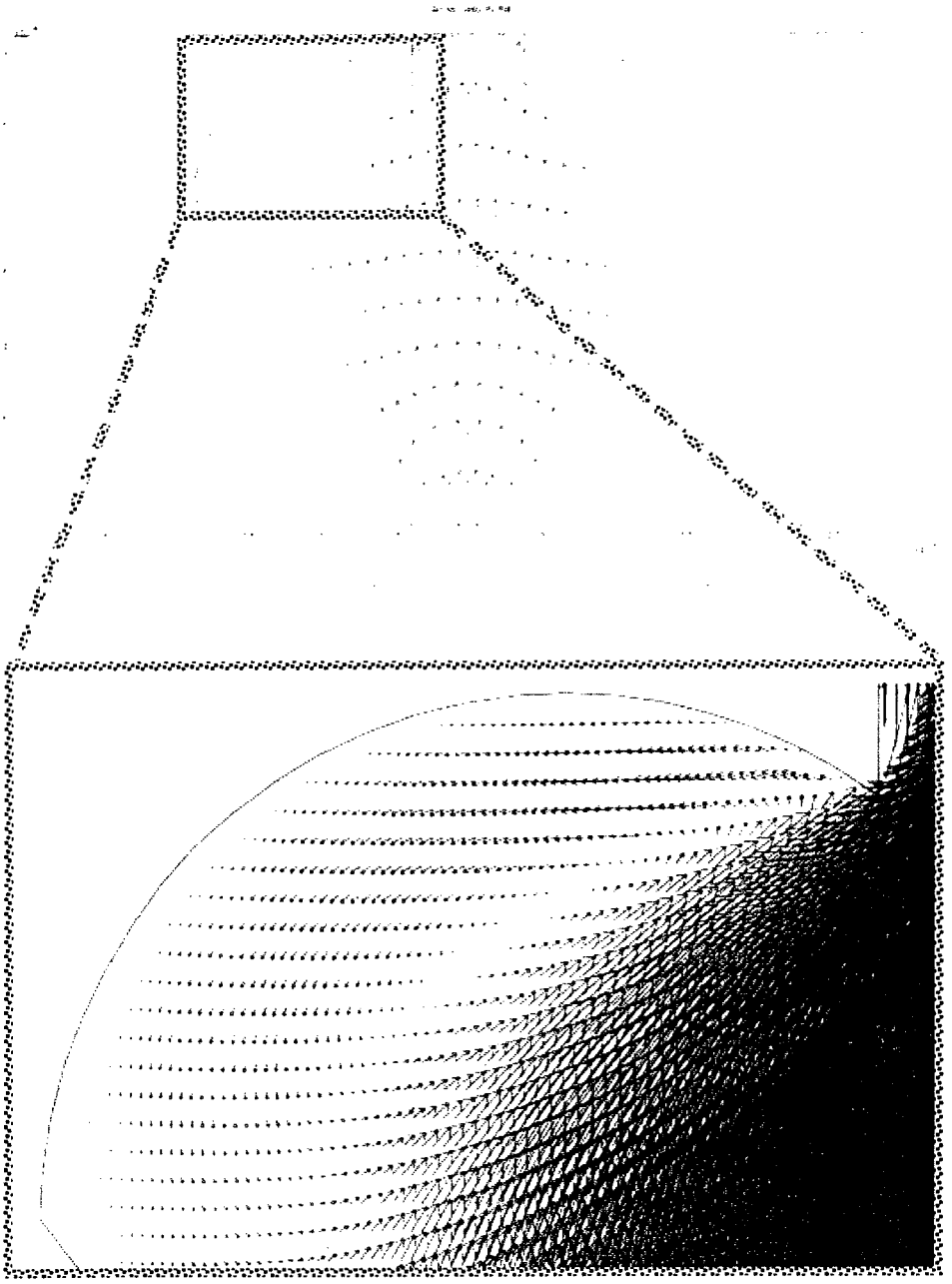

Figure 5. 22 Predicted velocity distributions indicated by arrow plot at flow rate of 4.78e-3mm^3/s (Re=6.87e-2) for shape V

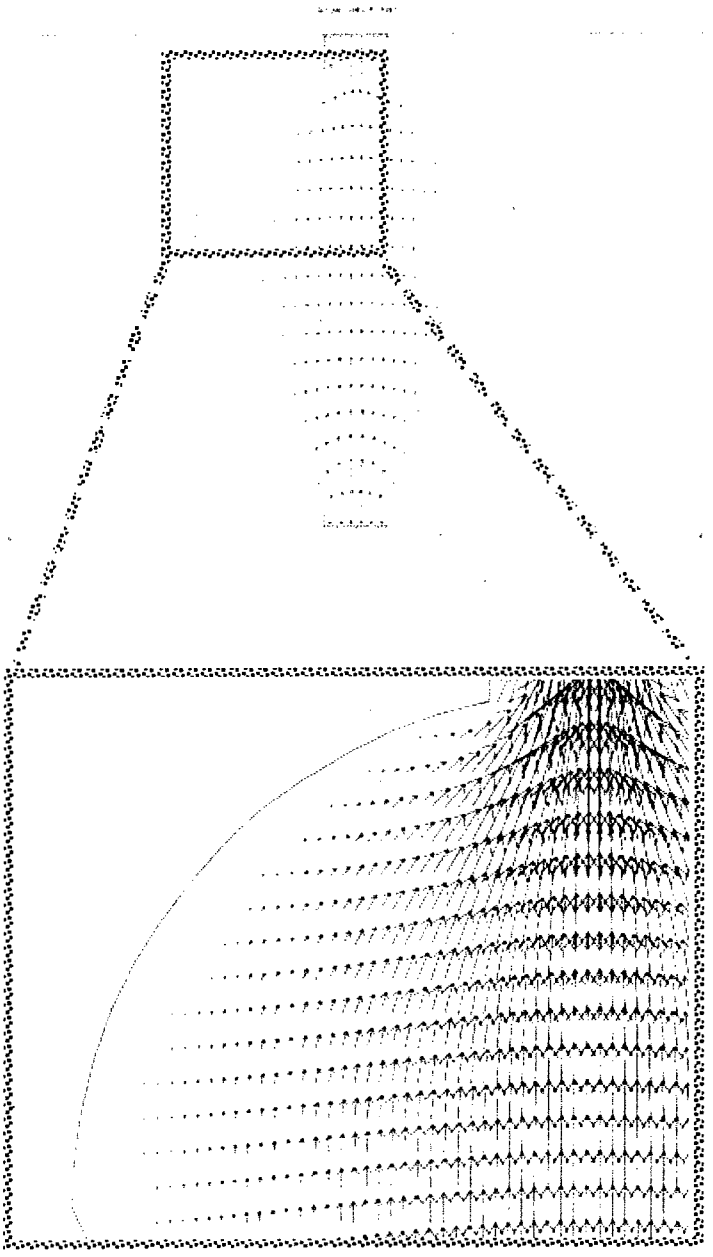

Figure 5. 23 Predicted velocity distributions indicated by arrow plot at flow rate of 4.78e-3mm^3/s (Re=6.87e-2) for shape IV

The comparison of prediction and experimented results are shown in Figures 5.24 to 5.29 for shape IV along x and y axis and also at different entrance flow rates. Except for the highest flow rate, the simulation results agreed well with the experimental results. Along mid-point section (x=-60μm) at the highest flow rate, the experimental results of peak part are lower in magnitude than the simulation results. Similarly, the comparison of prediction and experimented results are shown in Figures 5.30 to 5.35 for shape V along x and y axis and also at different entrance flow rates. Compared with the convex sides of shape IV, the shape V has a straighter tendency along mid-point sections.

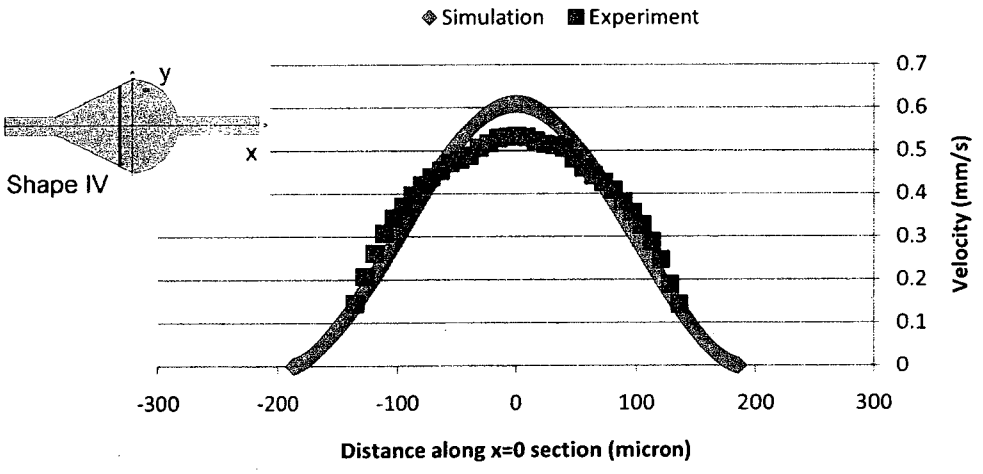

Figure 5. 24 Comparison of prediction and experimental velocity distribution along x= -60μm section at flow rate of 4.78e-3mm^3/s (Re=6.87e-2) for shape IV

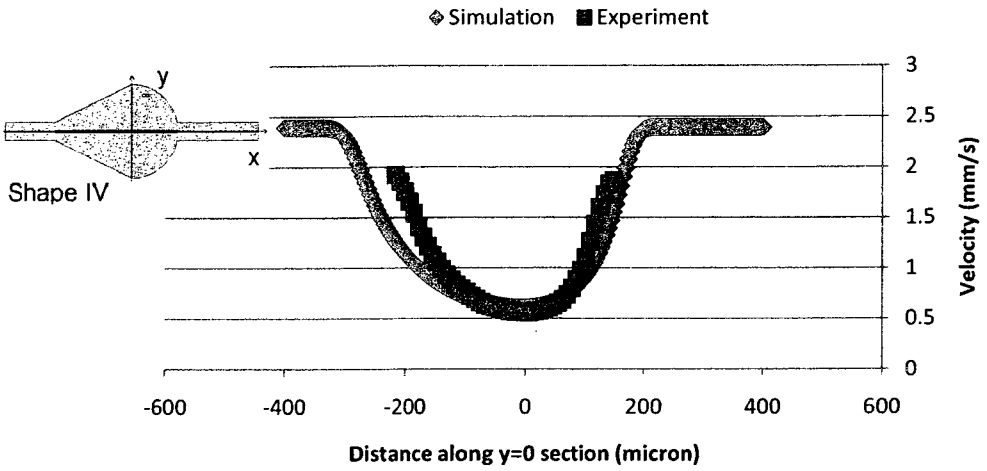

Figure 5. 25 Comparison of prediction and experimental velocity distribution along y=0μm section at flow rate of 4.78e-3mm^3/s (Re=6.87e-2) for shape IV

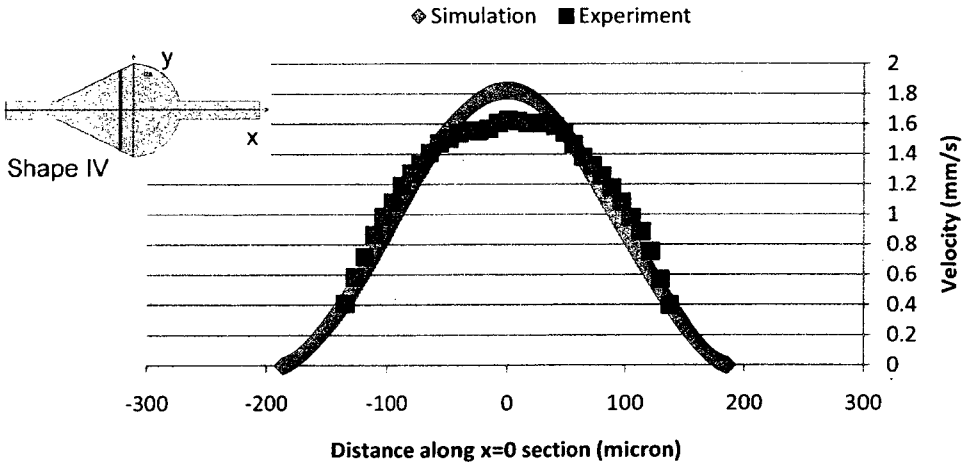

Figure 5. 26 Comparison of prediction and experimental velocity distribution along x= -60μm section at flow rate of 14.3e-3mm^3/s (Re=2.06e-1) for shape IV

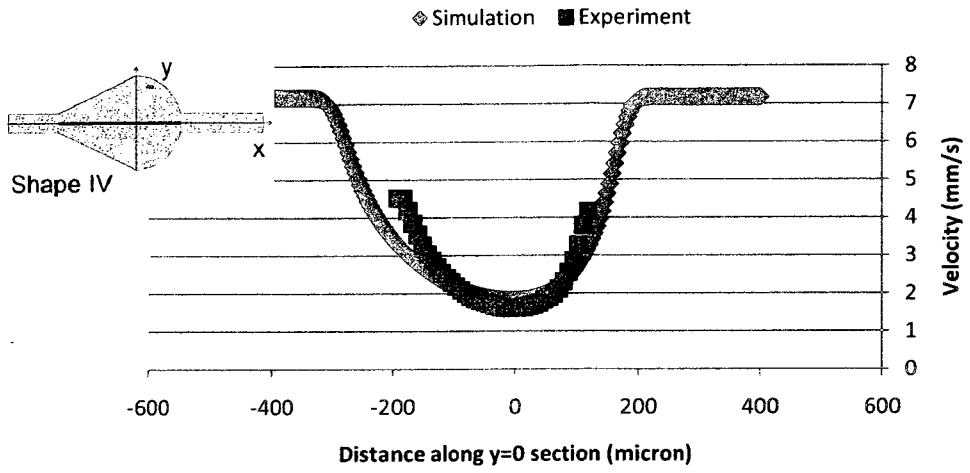

Figure 5. 27 Comparison of prediction and experimental velocity distribution along y=0μm section at flow rate of 14.3e-3mm^3/s (Re=2.06e-1) for shape IV

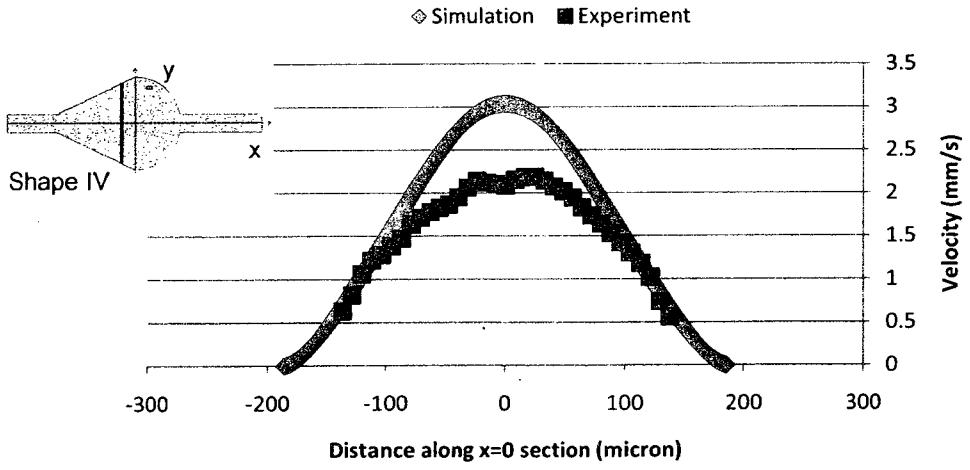

Figure 5. 28 Comparison of prediction and experimental velocity distribution along x= -60μm section at flow rate of 23.9e-3mm^3/s (Re=3.44e-1) for shape IV

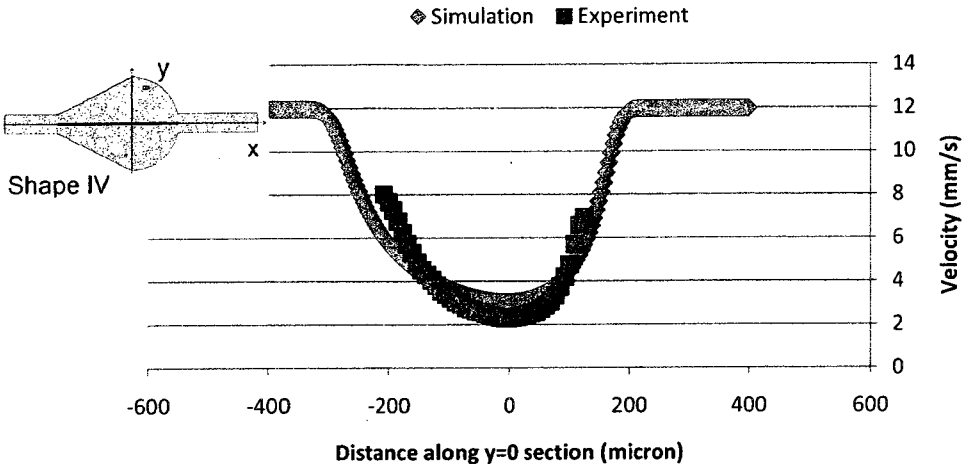

Figure 5. 29 Comparison of prediction and experimental velocity distribution along y=0μm section at flow rate of 23.9e-3mm^3/s (Re=3.44e-1) for shape IV

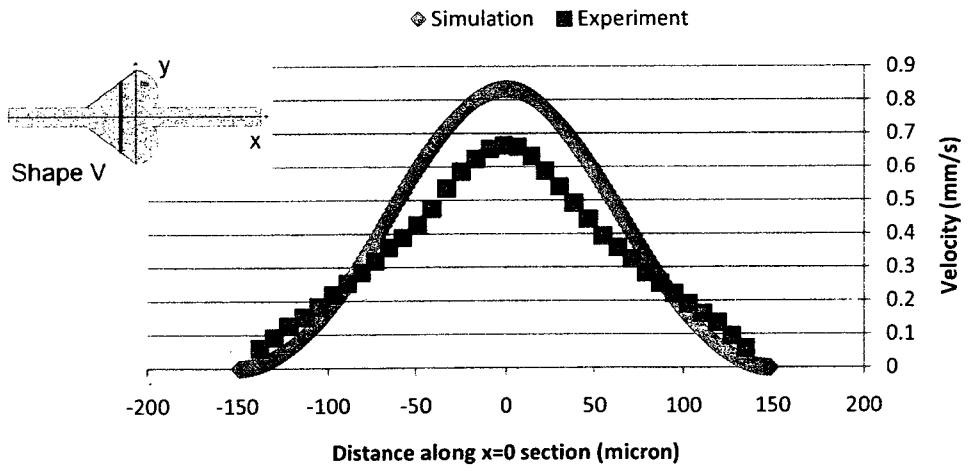

Figure 5. 30 Comparison of prediction and experimental velocity distribution along x= -90μm section at flow rate of 4.78e-3mm^3/s (Re=6.87e-2) for shape V

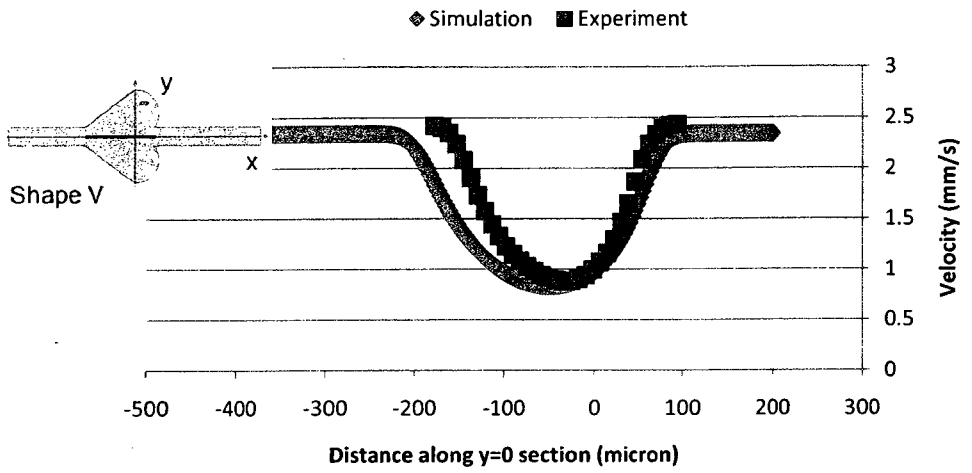

Figure 5. 31 Comparison of prediction and experimental velocity distribution along y=0μm section at flow rate of 4.78e-3mm^3/s (Re=6.87e-2) for shape V

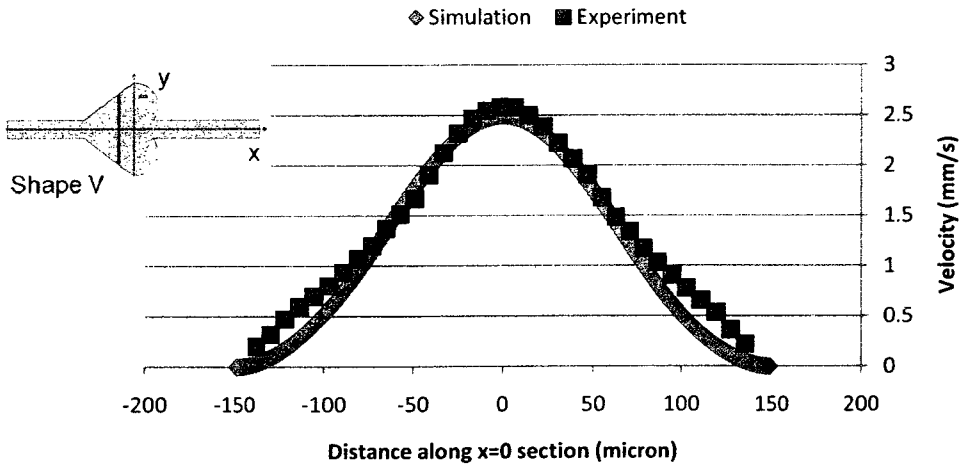

Figure 5. 32 Comparison of prediction and experimental velocity distribution along x= -90μm section at flow rate of 14.3e-3mm^3/s (Re=2.06e-1) for shape V section

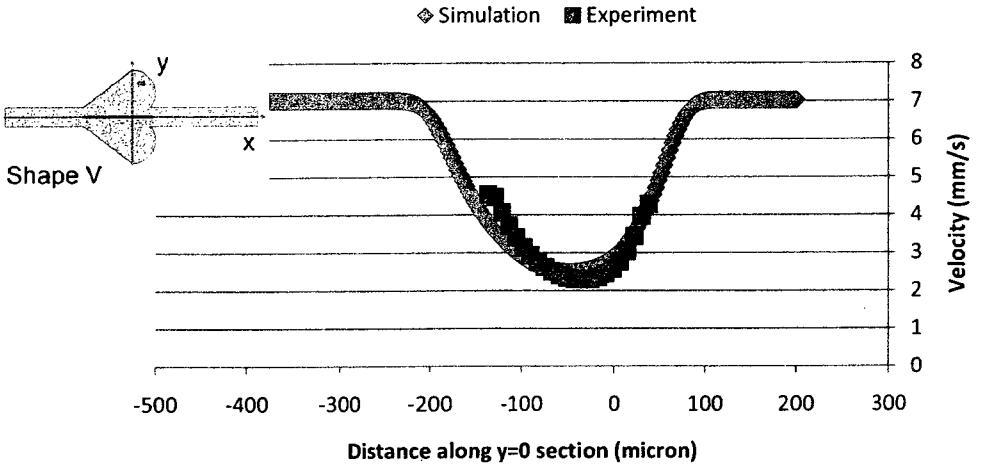

Figure 5. 33 Comparison of prediction and experimental velocity distribution along y=0μm section at flow rate of 14.3e-3mm^3/s (Re=2.06e-1) for shape V

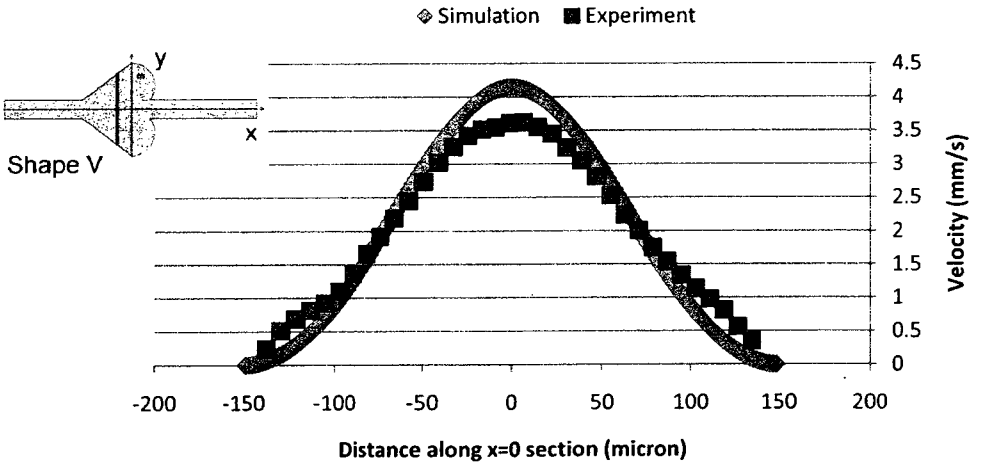

Figure 5. 34 Comparison of prediction and experimental velocity distribution along x= -90μm section at flow rate of 23.9e-3mm^3/s (Re=3.44e-1) for shape V

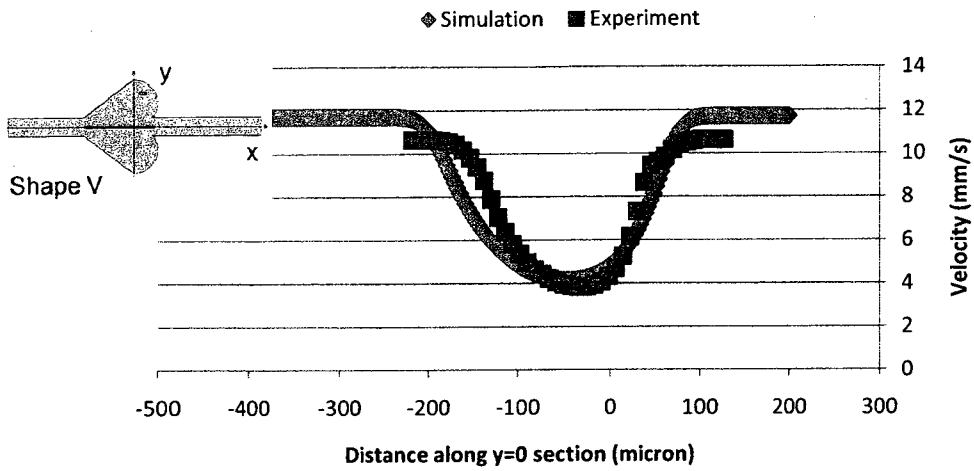

Figure 5. 35 Comparison of prediction and experimental velocity distribution along y=0μm section at flow rate of 23.9e-3mm^3/s (Re=3.44e-1) for shape V

5.6 Summary

Compared to experimental results, the predicted results show much more detailed information on flow velocity distribution along the entire chamber. In order to obtain better experimental results, certain adjustments on experimental settings are required. However, as confirmed by the simulation results, the experimental results obtained in this study gives a satisfactory agreement. The experimentation provided confirmation of the actual behavior of the flow.

Overall, compared the results obtained at the same cross section within the same microchamber at different velocity, despite the effect of detection limits, the experimental and simulation results have a fairly good agreement. The discrepancies between the experimental and simulation results could be due to the introduction of particles into the fluid which may change the characteristics of the flow to certain extend.

Theoretically, introduction of particles should not change the character of the flow; no slip effect of the particles could be detected under the experimental setups. With same measurement location, the much better matches could be achieved by using smaller particles, which has better following flow features, within the range of the detection limit.

Chapter 6

Conclusion and outlook

6.1 Conclusions

Since Manz and Eidmer introduced μTAS concept in 1990s [63], microfluidics' applications became one of the most popular research areas. Commercialized products from this field have also been continuously developed. These products also accelerated the development of MEMS, biochemistry and micro optics, etc.

The present study has described the design and fabrication process of glass based microfluidic chip. This study has also presented the model of microflow in a microfluidic chip, μPIV measurement methods, and simulation of microfluidic system. The results obtained from each method have also been compared.

However, the development of the microfluidics is still in its primary phase and a lot of research areas are still under investigation. As a flow visualization and characterization method, μPIV has become the most important study and verification tool in microfluidics. This study had discussed the major problems for μPIV platform

construction and the setup. By using the constructed μPIV platform, microfluidic glass-based chip produced by CMC, and fluorescent particles, the influence of geometry of microchambers on flow behavior has been detected and compared. The study has suggested that the shape of the microchambers is highly influential in flow field distribution. The simulation results are compared with the experimental results obtained from the μPIV measurements, at different cross sections of the microchambers.

Conclusions based on the results from present works are outlined as below:

- The pressure driven flow profile, which should be parabolic under classical condition, is exceptionally influenced around the inlet and outlet region of the microchambers.
- In terms of light source, optical fiber has been used to introduce the incident light which is not perpendicular to the surface of the chip. The oblique illumination method is different from previously published studies and may protect the optical instruments from damage by high energy laser light. Since the experimental results obtained under such a setup is similar to the simulation results, one can conclude that such a setup do not interfere with the experimental results.
- Shape IV is preferable what with less recirculating areas than shape V. The horizontal ellipse causes less dead zone than the vertical ellipse. But the vertical ellipse is better for mixing liquids in respect that the velocity difference is higher between the adjacent streamlines. The circular shape is currently used for both mixing and observation purposes. However, for only one of the purposes, either of the elliptical shapes which are specialized can be chosen.
- Reducing of length to width ratio of the microchambers can increase the velocity difference between adjacent stream lines, but may cause formation of the dead zone in peripheral region away from the center.

- If the outlet region of the microchamber is not at the top of its geometric shape, the formation of recirculation zone can be detected. However, in μPIV detected results, the velocity distribution within this region is different from the simulated results. Therefore, in terms of mixer design as one of the applications of microfluidics, the efficiency of mixing within this region is under study.

6.2 Future work

Recently, the microfluidics has been applied in a wide range of applications and researches involved in this area have also been derived into variety of branches. Based on the observations obtained from this study, further investigation is required in the following areas:

6.2.1 Optimization of the complicated geometric shapes of the microchamber.

As shown in this study, the shapes of the microchamber highly influence the flow distribution which directly leads to the change in efficiency of the mixing effect. Therefore, in applications such as devices involving chemical reactions, the shapes of the microchambers have to be optimized in the way that it maximizes the mixing effect but do not form dead zones within the chamber. In practice more complicated shapes of microchambers might be required which require more complicated mathematical model for the simulation of its flow distribution, which may not even be possible. Therefore, combination of actual experimentation and simulation is the best way for design and optimization of complicated microchambers.

6.2.2 Three dimensional flow distribution measurement in microfluidics

Since the microflow is three dimensional in nature, measurement of flow distribution at different horizontal planes should be detected. Currently, the three-dimensional measurement by PIV has been done in ordinary fluidic system, but

due to the size limitation, it is still hardly transferred into the field of microfluidics. By introducing certain improvements on the devices, the three-dimensional measurement of the microfluidic system can be achieved to some extent.

6.2.3 Extended application of μPIV including conditions involve high flow velocity and low particle concentration.

In practice, certain applications of microfluidics require high flow velocity and low particle concentrations. For instance, when testing blood flow in blood vessels, especially arterial blood flow, the flow velocity is very high and application of high concentration of florescent particles may influence the health condition of the organism. Therefore, improvements on mathematical model as well as certain hardware devices are required to achieve these requirements. In order to extend the velocity detect ability of the flow, more precise timer and laser generator giving precisely generated laser must be used. These devices reduce detection error associated with timing and therefore allow more accurate measurement under high flow velocity. In the case of reduced particle concentration, improved mathematical model is required for the calculation of the flow distribution.

6.2.4 The influence of flow distribution by surface characteristics of the wall for new materials

With the development of micro-fluid systems, new materials and manufacturing processes have been developed. That is, flow channel joined electronic circuits. New materials and new technology introduce new surface

properties. Study of these characteristics will be helpful for design and manufacturing.

6.2.5 Real time displacement of μPIV results.

Since μPIV calculation requires a long term post processing period, the flow distribution cannot be obtained instantly. Improvement on mathematical algorithm with parallel arithmetic and implement the calculations in the hardware will be useful to reduce the analysis time. This way, the real time displacement of the flow distribution might be achieved for on-site applications.

REFERENCES

1. Lee, F. C., and W. Crooks. A Review of Ink-Jet Printing. International Business Machines Corporation, 1988.

2. Manz, A. , N. Graber, and H. M. Widmer. "Sens. Actuators." B1 (1990): 244-248.

3. Flockhart, S. M. , and S. J. Yang. "Numerical Analysis of Fluid Flow in Channels of Micron Dimensions." Microengineered Components for Fluids 176 (1996).

4. Rice, L. , and R. Whitehead. "Electrokinetic Flow in a Narrow Cylindrical Capillary." The Journal of Physical Chemistry 69 11 (1965): 4017-4024.

5. Bien, D C S , et al. "Characterization of Masking Materials for Deep Glass Micromachining." Journal of Micromechanics and Microengineering 4 (2003): S34.

6. Jang, W. I., et al. "Fabrication of Mems Devices by Using Anhydrous Hf Gas-Phase Etching with Alcoholic Vapor." Journal of Micromechanics and Microengineering 3 (2002): 297.

7. Arana, Leonel R., et al. "Isotropic Etching of Silicon in Fluorine Gas for Mems Micromachining." Journal of Micromechanics and Microengineering 17 (2007): 384-392.

8. Revell, P.J., and G.F. Goldspink. Review of Reactive Ion Beam Etching for Production.

9. Ichiki, T., et al. "Plasma Applications for Biochip Technology." Thin Solid Films 435 1-2 (2003).

10. Belloy, E., A. Sayah, and M. A. M. Gijs. "Oblique Powder Blasting for Three-Dimensional Micromachining of Brittle Materials." Proceed. Eurosensors XIV, the 14th European Conference on Solid-State Transducers. Ed.

11. Jang, Ho-Su, Myeong-Woo Cho, and Dong-Sam Park. "Micro Fluidic Channel Machining on Fused Silica Glass Using Powder Blasting." Sensors 8 2 (2008): 700-710.

12. An, R., et al. "Water-Assisted Drilling of Microfluidic Chambers inside Silica Glass with Femtosecond Laser Pulses." Applied Physics A: Materials Science & Processing 83 1 (2006): 27-29.

13. Bart, S. F., et al. "Microfabricated Electrohydrodynamic Pumps." Sensors and Actuators 21-23 A (1990): 193-198.

14. Wu, S., et al. "Mems Flow Sensors for Nano-Fluidic Applications." International Conference on Micro Electro Mechanical Systems 13th, MEMS. Ed.: ISBN 0-7803-5273-4.

15. Herwaarden, Van A. W. , and P. M. Sarro. "Thermal Sensor Based on the Seebeck Effect." Sensors and Actuators 10 A (1986): 321-346.

16. An Integrated Sensor for Invasive Blood Velocity Measurement. 1993.

17. Lindken, R., J. Westerweel, and B. Wieneke. "Stereoscopic Micro Particle Image Velocimetry." Experiments in Fluids 41 2 (2006): 161-171.

18. Nguyen, Chuong V. , Andreas Fouras, and Josie Carberry. "Improved Accuracy of Micro Piv Measurement Using Image Overlapping Technique." 14th Int Symp on Applications of Laser Techniques to Fluid Mechanics. Ed.

19. Lima, Rui, et al. "In Vitro Blood Flow in a Rectangular Pdms Microchannel: Experimental Observations Using a Confocal Micro-Piv System." Biomedical Microdevices 10 2 (2008): 153-167.

20. Brody, J. P. , et al. "Biotechnology at Low Reynolds Numbers." Biophys J. 71 6 (1996): 3430–3441.

21. Meinhart, C. D. , S. T. Wereley, and J. G. Santiago. "Piv Measurements of a Microchannel Flow." Experiments in Fluids 27 (1999): 414-419.

22. Devasenathipathy, S., et al. "Particle Imaging Techniques for Microfabricated Fluidic Systems." Experiments in Fluids 34 4 (2003): 504-514.

23. Kim, Hyun-Seok, et al. "Separation of Apoptotic Cells Using a Microfluidic Device." Biotechnology Letters 29 11 (2007): 1659-1663.

24. Khandurina, J., et al. "Integrated System for Rapid Pcr-Based DNA Analysis in Microfluidic Devices." Anal Chem 72 13 (2000): 2995-3000.

25. Wolfe, K. A., et al. "Toward a Microchip-Based Solid-Phase Extraction Method for Isolation of Nucleic Acids." Electrophoresis 23 5 (2002): 727-33.

26. Yeung, S. H., et al. "Rapid and High-Throughput Forensic Short Tandem Repeat Typing Using a 96-Lane Microfabricated Capillary Array Electrophoresis Microdevice." J Forensic Sci 51 4 (2006): 740-7.

27. Seong, Gi Hun , Jinseok Heo, and Richard M Crooks. "Measurement of Enzyme Kinetics Using a Continuous-Flow Microfluidic System." Anal Chem 75 13 (2003): 3161-3167.

28. Figeys, Daniel, et al. "An Integrated Microfluidics-Tandem Mass Spectrometry System for Automated Protein Analysis." Analytical Chemistry 70 18 (1998): 3728-3734.

29. Grayson, A. C., et al. "Differential Degradation Rates in Vivo and in Vitro of Biocompatible Poly(Lactic Acid) and Poly(Glycolic Acid) Homo- and Co-Polymers for a Polymeric Drug-Delivery Microchip." J Biomater Sci Polym Ed 15 10 (2004): 1281-304.

30. Herr, A. E., et al. "Integrated Microfluidic Platform for Oral Diagnostics." Ann N Y Acad Sci (2007): 362-74.

31. Srinivasan, V., V. K. Pamula, and R. B. Fair. "An Integrated Digital Microfluidic Lab-on-a-Chip for Clinical Diagnostics on Human Physiological Fluids." Lab Chip 4 4 (2004): 310-5.

32. Xuan, Wenga, et al. "Rapid Detection of Formaldehyde Concentration in Food on a Polydimethylsiloxane (Pdms) Microfluidic Chip." Food Chemistry 114 3 (2009): 1079-1082.

33. Sakamoto, C., et al. "Rapid Quantification of Bacterial Cells in Potable Water Using a Simplified Microfluidic Device." J Microbiol Methods 68 3 (2007): 643-7.

34. Vaillanta, F. , et al. "Turbidity of Pulpy Fruit Juice: A Key Factor for Predicting Cross-Flow Microfiltration Performance." Journal of Membrane Science 325 1 (2008): 404-412.

35. Wu, M. L., R. R. Zall, and W. C. Tzeng. "Microfiltration and Ultrafiltration Comparison for Apple Juice Clarification." Journal of Food Science 55 4 (1990): 1162-1163.

36. Marle, L. , and G.M. Greenway. "Microfluidic Devices for Environmental Monitoring." TrAC - Trends in Analytical Chemistry 24 9 (2005): 795-802.

37. McGraw, C. M., et al. "Autonomous Microfluidic System for Phosphate Detection." Talanta 71 3 (2007): 1180-5.

38. Bazylak, A., D. Sinton, and N. Djilali. "Improved Fuel Utilization in Microfluidic Fuel Cells: A Computational Study." Journal of Power Sources 143 1-2 (2005): 57-66.

39. Ahn, Chong H. and A. Bruno Frazier eds. Characterizing the Process of Cast Molding Microfluidic Systems. 1999. SPIE.

40. Xia, Younan, and George M. Whitesides. "Soft Lithography." Annual Review of Materials Science 28 1 (2003): 153-184.

41. Duffy, D. C., et al. "Rapid Prototyping of Microfluidic Systems in Poly(Dimethylsiloxane)." Analytical Chemistry 70 23 (1998): 4974-4984.

42. Corman, T., P. Enoksson, and G. Stemme. "Deep Wet Etching of Borosilicate Glass Using an Anodically Bonded Silicon Substrate as Mask." Journal of Micromechanics and Microengineering 8 2 (1998): 84-87.

43. Berthold, A., P. M. Sarro, and M. J. Vellekoop. "Two-Step Glass Wet-Etching for Microfluidic Devices." Proceedings of SeSens 2002. Ed.

44. Niino, H., et al. "Laser Ablation of Toluene Liquid for Surface Micro-Structuring of Silica Glass." Applied Surface Science 252 13 SPEC (2006): 4387-4391.

45. Protolyne: A Micromachining Process for Microfluidic Applications. Micralyne Inc., 2004.

46. Santiago, J. G., et al. "A Particle Image Velocimetry System for Microfluidics." Experiments in Fluids 25 4 (1998): 316-319.

47. Ingle, J. D. J. , and S. R. Crouch. Spectrochemical Analysis. New Jersey: Prentice Hall, 1988.

48. Konrad, Michael. "Diffusion". <http://www.scienceisart.com/A_Diffus/Xeq2Dt_2.html>.

49. Product Catalog and Technical Reference Guide. Thermo Scientifi Inc., 2007.

50. Fluorescence Filter Sets Guide. Nikon Instruments Inc., 2005.

51. Miniplus 3 Peristaltic Pump User's Guide. Gilson Inc., 2003.

52. Digital Image Processing in Industry and Science. Hanau: AEON Verlag & Studio, 2002.

53. Stanislas, M., et al. "Main Results of the Third International Piv Challenge." Experiments in Fluids 45 1 (2008): 27-71.

54. Hirt, C.W., and B.D. Nichols. "Volume of Fluid/Vof/ Method for the Dynamics of Free Boundaries." Journal of computational physics (1981).

55. Comsol User's Guide. COMSOL Inc, 2008.

56. Fluent User's Guide. Fluent Inc, 2007.

57. Fluid Analysis Solutions Brochure. ANSYS Inc., 2007.

58. The Phoenics-Vr Udf Manual. CHAM Ltd, 2006.

59. Star-Cd Manual. CD-adapco Inc, 2006.

60. Olesen, L. H., F. Okkels, and H. Bruus. "A High-Level Programming-Language Implementation of Topology Optimization Applied to Steady-State Navier-Stokes Flow." International Journal for Numerical Methods in Engineering 65 7 (2006): 975-1001.

61. Pfitzner, J. "Poiseuille and His Law." Anaesthesia 31 2 (1976): 273-5.

62. Bayraktar, T. , and S.B. Pidugu. "Characterization of Liquid Flows in Microfluidic System." International Journal of Heat and Mass Transfer 49 (2006): 815-824.

63. Reyes, D. R., et al. "Micro Total Analysis Systems. 1. Introduction, Theory, and Technology." Analytical Chemistry 74 12 (2002): 2623-2636.